January 2013

Myoglobin Detection on SiC: Immunosensor Development for Myocardial Infarction

Alexandra Oliveros Villalba
University of South Florida, amolive4@mail.usf.edu

Scholar Commons Citation

Oliveros Villalba, Alexandra, "Myoglobin Detection on SiC: Immunosensor Development for Myocardial Infarction" (2013). *Graduate Theses and Dissertations.*
http://scholarcommons.usf.edu/etd/4740

Myoglobin Detection on SiC: Immunosensor Development for Myocardial Infarction

by

Alexandra Oliveros Villalba

A dissertation submitted in partial fulfillment
of the requirements for the degree of
Doctor of Philosophy
Department of Electrical Engineering
College of Engineering
University of South Florida

Co-Major Professor: Stephen E. Saddow, Ph.D.
Co-Major Professor: Mark J. Jaroszeski, Ph.D.
Andrew Hoff, Ph.D.
Sylvia Thomas, Ph.D.
Nathan Gallant, Ph.D.
Anthony Guiseppi-Eli, Ph.D.

Date of Approval:
May 21, 2013

Keywords: Biosensor, impedance spectroscopy, silicon carbide, biocompatibility, self-assembled monolayers

DEDICATION

"To my family,

your encouragement in the hardest times made me the person I am today. Thank you for being the light that brightened my path in the darkest times"

ACKNOWLEDGMENTS

I would like to thank my major professor, Dr. S.E. Saddow and co-major professor, Dr. M.J. Jaroszeski for believing in me and for nominating me for the Presidential Doctoral Fellowship. For always providing the financial support and resources, including their expertise to succeed in the completion of my work. To Dr. A. Guiseppi-Eli for all the discussions and guidance that contributed to chapter 2 and chapter 3, and for encouraging me to explore the field of potentiostatic and impedance based sensors. I want to also thank Dr. A. Sagüés for sharing his knowledge and expertise and for teaching me the basics in electrochemistry, the time spent in your lab made possible chapter 4.

I want to express my gratitude to Dr. A. Hoff for his advice in the area of device processing and characterization. To Dr. S. Thomas for helping me understand what the PhD is about, and helping me to be practical and prioritize effectively. I wish to thank Dr. N. Gallant for providing his expertise in the area of biomaterials and cell mechanics when I was working with graphene.

To my colleagues from the Walter Schottky Institute, Dr. I.D. Sharp, Dr S. Schoell and M. Sachsenhauser, thank you for teaching me about organic functionalization of SiC and providing XPS analysis. I want to express my gratitude to C. Kotanen, J. Byrd and N. Wilson from the Center for bioelectronics, biosensors and biochips for their help when I started learning about impedance spectroscopy. Also, to E. Paz and A. Sanchez for their assistance using the potentiostat and setting up my workspace in the USF corrosion lab.

Thank you to T. Chapman for assisting me in ordering the chemicals and providing advice for my cell culture technique.

For providing expertise and advice when I developed my protocols and cell culture assays, protein conjugation and antibody immobilization I want to thank L. West. To the NREC staff, R. Tufts, R. Everly, J. Bieber and Dr Y. Emirov for providing their expert advice and training in some of the tools I needed to build my devices.

I also want to thank B. Batson for providing resources outside of the lab to network with students and professionals and plan my career path. Last, but not least, I want to express my gratitude to Dr. C. Locke and Dr. C. Frewin who taught me all the techniques and were there with me from the start of this journey. To my colleagues that were in the SiC group: Dr. C. Coletti for starting the bio-SiC research, Dr. N. Schettini for performing the hema-compatibility SiC experiments. And to those who are in the group: Dr S. Afroz and Dr M. Reyes for growing the SiC films, M. Nezafati for helping me with the characterization of the SiC, J. Register for working on the *a*-SiC and J. King for building the glove box used for the SAM preparation.

TABLE OF CONTENTS

LIST OF TABLES

LIST OF FIGURES

ABSTRACT

Silicon carbide (SiC) has been around for more than 100 years as an industrial material and has found wide and varied applications because of its unique electrical and thermal properties. In recent years there has been increased attention on SiC as a viable material for biomedical applications. Among these applications are those where SiC is used as a substrate material for biosensors and biotransducers, taking advantage of its surface chemical, tribological and electrical properties.

In this work we have used the proven bio- and hema-compatibility of SiC to develop a viable biorecognition interface using SiC as the substrate material for myocardial infarction detection. The approach followed included the development of an electrochemical-based sensor in which 3C-SiC is used as the active electrode and where flat band potential energy changes are monitored after successive modification of the SiC with aminopropyltriethoxysilane, anti-myoglobin and myoglobin incubation.

We have studied the quality of self assembled monolayers obtained by surface modification of SiC using organosilanes such as aminopropyltriethoxysilane and octadecene, which is the starting point for the immobilization of cells or proteins on a substrate. We employed this technique on 6H-SiC where we were able to control the proliferation of H4 human neuroglioma and PC12 rat pheochromocytoma cells *in vitro*. Finally, aminopropyltriethoxysilane (APTES) was successfully used to immobilize anti-myoglobin on the 3C-SiC electrodes as demonstrated by fluorescence microscopy results. The electrical characterization of the surfaces was performed via impedance spectroscopy and by measuring changes in flat band potential using the Mott-Schottky plot technique.

Changes in flat band and impedance of the SiC/antibody/protein interface would allow us to detect changes in the space charge region of the semiconductor. However, we believe that because of the presence of surface states and different crystal defects on the 3C-SiC we did not observed repeatable results that allowed us to identify the presence of myoglobin in solution. In addition, certain modifications need to be performed to the electrochemical cell in order to confirm the presence of the myoglobin immobilized on the functionalized SiC surfaces.

CHAPTER 1: INTRODUCTION TO A MYOCARDIAL INFARCTION SILICON CARBIDE IMMUNOSENSOR

1.1 Research Objective and Motivation

Enabling the continuous monitoring of physiological parameters that provide a physician with the knowledge to determine a proper therapy for their patient is becoming a major area of interest in the biomedical research [1]. The use of biomarkers, in addition to other techniques, can produce more effective and targeted diagnoses provided that they can be implemented in real-time [2].

Individuals with silent cardiac syndrome develop myocardial infarctions (MI) that go unnoticed and require periodic examinations [3]. The continual monitoring of Troponin I, Creatine kinase (CK1) and Myoglobin can provide highly specific diagnostic data even before the clinical manifestations of a MI becomes apparent. Myoglobin concentrations rise quickly after a MI event and it is thus considered a biomarker for the early detection of MI [4].

Silicon Carbide (SiC), and more specifically 3C-SiC, has been shown to be a bio- and hema-compatible semiconductor material [5]. Various forms of SiC have been extensively used and studied, such as amorphous SiC, as a heart stent coating [6, 7], and it has been shown to be a promising material for long-term biological applications [8]. The fact that 3C-SiC can be grown by chemical vapor deposition (CVD) on Si substrates has made it an attractive material for BioMEMs applications and field effect devices such as the field effect transistor or FET [9, 10]. The principle of operation of a FET biosensor is based on the assumption that charged molecules in close proximity to the semiconductor induce an electric field that penetrates the near-surface region of the semiconductor and alters the conductivity of the semiconductor, a change which can be sensed electronically.

Proteins such as antibodies and myoglobin have many charges and the use of alternating current (AC) and electrochemical impedance spectroscopy (EIS) allow the measurement of changes produced by the mentioned molecules once immobilized on a semiconductor or a metal surface. The use of EIS allows one to identify physical processes related to biological process on the SiC surface that dominate different parts of the impedance spectrum [11].

1.2 Acute and Silent Myocardial Infarction

Heart attack is the usual name given to acute myocardial infarction (AMI), even though it is also used to refer to other diseases. This condition can be the first manifestation of a coronary disorder or it can become a major concern for patients with established coronary disease. AMI is probably one of the main diseases to cause death, mostly in developed countries. Statistics suggest that around 1.5 million heart attacks occur each year, one occurs every twenty seconds and a possible death every minute [12]. The intensive care unit (ICU) usually contains a significant number of patients having underlying cardiac disease. This includes patients with acute myocardial infarction, acute heart failure, among other symptoms [13].

The two words, myocardial and infarction, imply that cardiac myocytes in the heart tissue die, mainly because of a lack of oxygen [14]. Myocardial infarction consists of irreversible necrosis in heart muscle after a prolonged ischemia. Oxygen is supplied to the heart through the arteries in order to complete metabolic processes.

Plaque rupture or thrombus formation in a coronary vessel may cause a reduction of blood supply to an area of the myocardium along with an imbalance in the oxygen supply [15], see Figure 1. If blood flow to the heart is interrupted, the tissue that has suffered necrosis will not recover and is usually covered by a collagen scar. The consequence is that the heart action potential will occur at a slower rate, resulting in a low heartbeat rate that will be prolonged so that the healthy tissue can contract. Healthy heart muscle does not relax because the electrical impulse can reenter and trigger healthy heart muscle to beat again. If the beat rate reaches 200 beats per minute, heart output and blood flow are reduced to zero and eventually the heart stops beating.

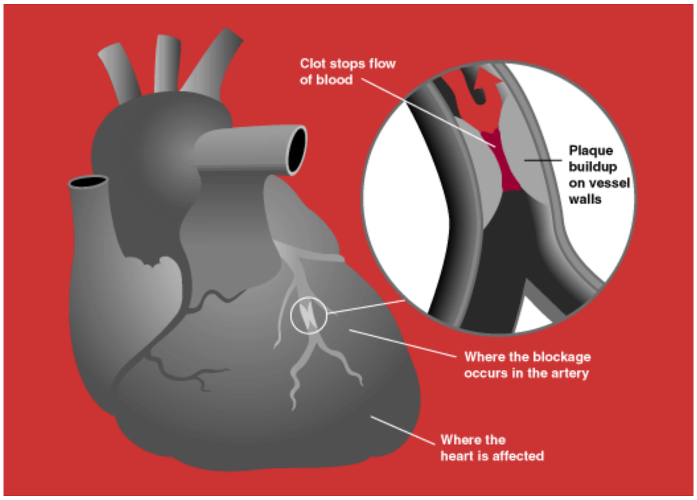

Figure 1 Possible causes of myocardial infarction illustrated in the heart.

In an event where there is of lack of oxygen in the heart, a reduction in the metabolism in the organ occurs, which reduces the force of muscular contraction and a decrease of the systolic wall motion in the affected region. In addition to the mentioned changes, there is diastolic relaxation with abnormal systolic contractile function and a thickening of the heart walls which leads to the formation of ischemic tissue.

1.2.1 Silent Myocardial Infarction

A silent myocardial infarction is defined as heart ischemia with no symptoms related to the same, i.e., an absence of chest discomfort [3, 16]. It has been estimated that silent ischemia occurs in 2-4% of the adult population [17]. Typically in 20 - 60% of patients that present acute myocardial infarction the classic symptoms are not displayed and are classified as silent myocardial infarction [18]. Since no symptoms are noticed at the time of the occurrence of the infarction, it is typically detected by a surveillance of ECG, during which some of the patients show atypical symptoms [19]. Patients that are predisposed to this condition include individuals with renal failure [20], patients with sudden death [21] and those with unstable angina [22].

1.2.2 Diagnosis of Myocardial Infarction

Diagnosing cardiac infarction is a difficult task, especially in the ICU mainly due to the non-specificity of clinical signs and symptoms. Sometimes, the symptoms are non-specific and the disease can be misdiagnosed and attributed to gastrointestinal, neurological, pulmonary or musculoskeletal disorders, especially in diabetics and the elderly [23]. The criteria for diagnosis of AMI includes: Symptoms of ischemia, chest pain (when the infarction lasts for more than 20 min) or coronary occlusion, electrocardiogram (ECG) changes of new ischemia such as ST segment elevation or depression and development of pathological Q waves (see Figure 2), evidence of loss of myocardium (using imaging methods) or regional wall motion abnormality [24]. Moreover, changes in ECG present low sensitivity and sometimes the AMI could be silent with no chest pain or other symptoms. The methods to detect silent ischemia include the use of a treadmill or echocardiography. However, they tend not to be precise because the silent infarction usually occurs during periods of low activity including rest or sleep. A Holster monitor is also used because it provides the advantage of monitoring the patient during their daily routines; however the ST segments of the ECG recorded tend to be non-specific and there is high variability in the data recorded from day to day. In addition a Holster monitoring can only be used for 72 hrs. [25].

Continuous monitoring of the physiologic conditions and prompt treatment can reduce mortality and improve patient outcome.

a) b) c)

Figure 2 ECG representations a) P,Q,R,S & T Waves b) normal sinus rhythm [26] and c) myocardial infarction rhythm. Note the elevation of the ST segment in yellow.

1.2.3 Biochemical Markers for Diagnosis of AMI

Biochemical markers are macromolecules present in the sarcolemmal membrane of myocytes. Typically, they are not present in blood, but they begin to diffuse into the cardiac interstitial tissue and into the micro-vascular and lymphatic tissue after an injury. When these molecules are present in the blood circulation this can be taken as an indication of myocardial necrosis and most of the time it is confirmed using ECG and/or imaging techniques. The main proteins that appear in the circulation after heart tissue damage include: Myoglobin, cardiac troponin (cTn) T and I, creatine kinase (CK) and lactate dehydrogenase (LDH) [27]. Levels of myoglobin rise and fall rapidly after 24 hrs., whereas levels of cTn and CK can remain elevated for up to one week [28].

In patients with diagnostic ECG changes cardiac markers are only useful to confirm the diagnosis, but they become essential for patients with non-specific symptoms since the use of biochemical markers enhance previous clinical ECG information [23]. The advantage of combining cardiac markers with other methods resides in the possibility of determining the severity of the disease in addition to prognosis values that can be used to formulate the appropriate therapy.

1.2.3.1 Myoglobin

Myoglobin is a compact heme protein with a low molecular weight of around 17.8KD (kilo Dalton). It is mainly found in cardiac and skeletal muscle, and facilitates the transport of oxygen to the cell mitochondria [29]. Myoglobin is one of the earliest known and commercially available biochemical markers used for the detection of AMI. After the first symptoms of AMI are detected it is rapidly released from the site of injury and its sensitivity is greater than CK-MB and cTn.

The concentration of Myoglobin in serum levels increases within 2 hrs. after myocardial infarction and reaches a peak concentration after 6 - 9 hrs. [30]. A serum concentration of myoglobin greater than 110 μg/L is considered abnormal and indicative of AMI [14]. Nevertheless, when using this biomarker one has to consider that since it is present in both skeletal and cardiac muscle, it would be released into the bloodstream after damage to any of these. It is recommended that a combination of two biomarkers, such as cTn or CK-MB, be used to diagnose AMI as it serum levels of myoglobin are also elevated due to neuromuscular disorders, renal failure, exercise or drug intake [31].

1.2.3.2 Cardiac Troponin (cTn)

Troponin is a molecular complex with a relative mass of 80 KD and is formed by three subunits: TnC the Ca binding subunit, TnT the tropomyosin binding subunit and TnI the inhibitory subunit. The cTnI is expressed only in the myocardium. This protein plays a significant role in muscle contraction coupled with ATPase. In cardiac muscle, this protein regulates muscle contraction in response to intracellular Ca concentration [32].

The cTn biomarker has demonstrated high specificity and is sensitive to detect cardiac injury [33]. Elevations in this biomarker's levels are registered after 6 - 9 hrs. after onset of the infarction symptoms. It has excellent myocardial tissue specificity as well as high clinical sensitivity and reflects even microscopic zones of myocardial necrosis [27].

Blood samples are typically drawn from the patient within 6- 9 hrs. after the onset of symptoms, and additional samples are taken 12 - 24 hrs. if the initial measurements do not present high enough levels. cTnI is also useful for late or continuous monitoring of AMI because elevated concentrations in the blood can be detected after 5 - 8 days of AMI onset. In addition, a rising or falling pattern is needed to distinguish background levels of cTn, for example, patients with chronic renal failure from patients with AMI. The disadvantage of the current methods used is that when this type of analysis is performed the results are needed in 30 min, but the reality is that results are usually available after 2 hrs. [34].

1.2.3.3 Creatine Kinase (CK)

Creatine kinase is a dimeric enzyme with a molecular weight ~80 KD that exists as three different isozymes: MM (muscle), MB (hybrid), and BB (brain). The isozymes names indicate the tissue of origin. For instance, the CK-MB has its highest concentration in heart muscle, and that is the main reason to use it as a diagnostic of myocardial infarction [35]. As with cTn, an increase in CK-MB level can be used as a measurement for the diagnosis of myocardial infarction. For this particular enzyme, gender specific values should be taken into consideration. Similarly to the evaluation of cnT, the CK-MB measurement should be done at the time of the first evaluation of the patient and within 6–9 h later in order to demonstrate the rise or fall of CK-MB levels for the diagnosis of AMI. In addition, in a few cases patients may require an additional sample to be drawn between 12 and 24 h if the earlier CK-MB measurements were not high enough to account for AMI diagnosis. Nonetheless, measurements of CK-MB alone are not recommended for diagnosis of AMI because of the large skeletal muscle distribution and the lack of specificity of this enzyme [27].

1.3 Immunosensors

Immunosensors can play an important role in the improvement of public health by providing for rapid detection, high sensitivity, and specificity in areas such as clinical chemistry, food quality, and environmental monitoring [36]. In contrast to immunoassays, like ELISA (enzyme immunosorbent linked assay) the development of transducer technology allows for the detection of trace substances in the environment of interest using label-free detection methods. This allows one to analyze the target substance more quickly than with conventional methods such as ELISA.

The design of a biosensor involves the inclusion of a biological receptor, used for the detection of a target analyte. Typically the receptor is immobilized onto a physical or physicochemical transducer, which translates the biological interaction between the receptor and the target analyte into an electrical signal. Examples of biological receptors include: enzymes, antibodies or antibody fragments, membrane receptors, whole cells, and DNA fragments. In particular, the term immunosensor is specifically employed to describe devices that take advantage of the affinity and the specificity between an antibody and the corresponding antigen to detect and quantify the presence of substances such as viruses, microorganisms, and toxins in a mixture to be analyzed [36, 37].

In order to build an efficient immunosensor/biosensor, the immobilized molecule should possess a low degree of nonspecific binding (NSB). Although antibodies are highly specific to a particular antigen, NSB could occur due to the matrix or surface where the antibody is to be immobilized or different components in the sample serum that may interact with the sensor substrate [37].

Some of the most frequent transducer methods are based on electrochemistry, fluorescence, interferometry, resonance, and reflectometry. Figure 3 shows an illustration of several detection methods used to detect immunoreactions.

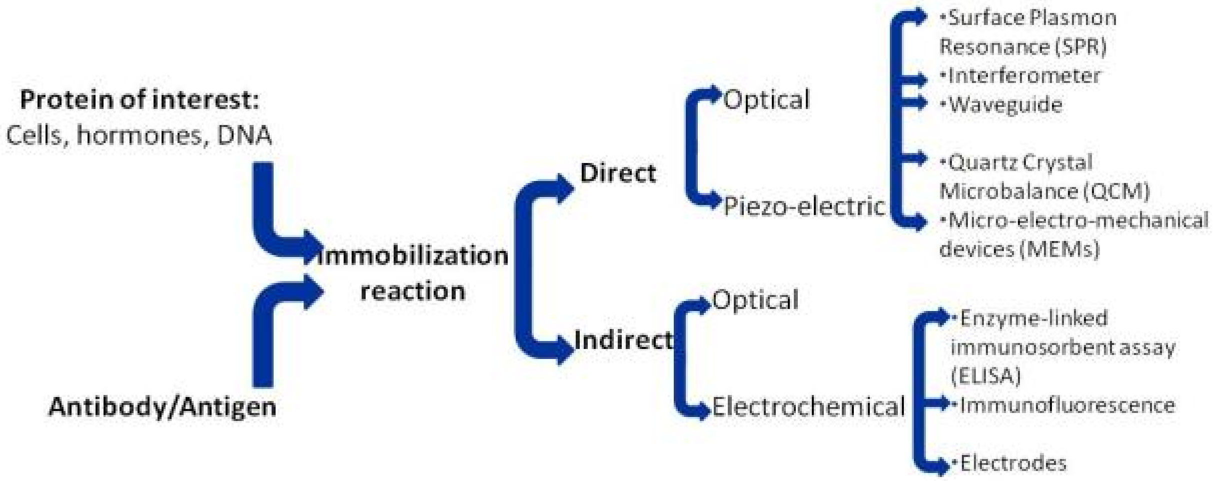

Figure 3 Detection methods for diagnostic applications using immunoreactions. Based on [36].

1.3.1 Immunoreaction/Biomolecular Recognition Element.

The use of an antibody as the recognition element in biological devices, has received increased attention because they can be obtained from natural sources and present a high degree of specificity to the molecule of interest.

1.3.1.1 Antibody Structure

An antibody is a globular protein with approximately 150 kD molecular weight and can have different amino acid sequences which makes them a diverse protein [38]. Since the function of an antibody is to bind to foreign molecules, the typical method used to synthesize them includes the use of B-lymphocytes in the presence of an antigen, i.e. a molecule that does not belong to the animal. Different classes of antibodies have a unique amino acid sequence that can bind to a specific epitope, located on the so called "arms" of the antibody; whereas the "stem" defines the biological activity that defines the response to an antigen including allergy, lysis or phagocytosis [36, 38].

The principal antibody found in serum is immunoglobulin or IgG. The simplified structure of an antibody is illustrated in Figure 4 using IgG as a typical example. It consists of two heavy chains (V_H and C_{H1}) and two light chains (V_L and C_L) that contain functional domains. The Fab portion contains the structural recognition domain while the Fc region does not bind to an antigen and is known as the effector domain. The Fab fragments can be obtained by using reducing agents, which could produce an improved immobilization and exposure of the binding sites for immunosensor device construction [38, 39].

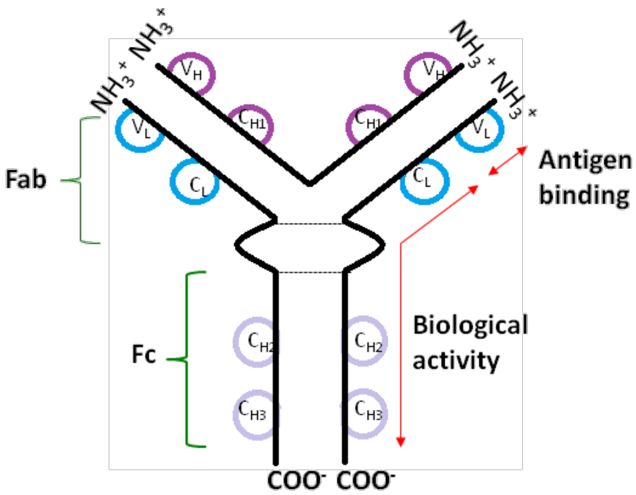

Figure 4 Immunoglobulin (IgG) simplified structure.

1.3.1.2 Antibody Immobilization

An effective immobilization of the biorecognition element, i.e. antibody, on the device surface is important. Complete loss of protein activity could happen due to random orientation and structural deformation of the antibody molecule once immobilized on the surface [40]. For this reason, the orientation, distribution and density of the antibodies on the surface should be controlled if possible. The use of self-assembled monolayers and Langmuir-Blodgett films [41, 42] are widely used for the mentioned purpose in addition to the use of a crosslinking agent [8, 43] or through entrapment in a gel matrix or polymer [44].

Immobilization techniques are mainly based on three mechanisms that include: physical, covalent or bioaffinity. There is no unique strategy that works for immobilizing all types of proteins and some work better compared to others when implemented in immunosensors.

1.3.1.2.1 Physical Immobilization

This method is based on the adsorption of proteins to flat surfaces via intermolecular forces, such as ionic bonds and polar interactions [40]. This is a fast and simple method but useful only in single-use assays because the proteins may be removed by buffers or detergents when performing and experiment [37, 40].

If this method is used for protein immobilization, the resulting layer may tend to be randomly oriented. Likewise, a high density packed layer may block the protein active site which interferes with their functional properties (e.g. it may prevent antigen-antibody binding) [40]. This method of protein immobilization is typically used in enzyme-linked immunosorbent assay (ELISA) preparation, for which polystyrene plates have been optimized to increase antibody adsorption [37]

1.3.1.2.2 Covalent Immobilization

The advantage of using a covalent binding method for protein (or antibody) immobilization is that the attachment of the molecule is more stable with long-term preservation of its activity, thus making it possible to regenerate the surface after performing the assay.

The covalent bond obtained after applying this method is formed between side chains exposed functional groups of the protein with the ones on the modified substrate. The latter ones are obtained by chemical modification of the surface using the techniques mentioned in section 1.4. The resulting bond is almost irreversible with high surface coverage [40].

Covalent binding is achieved with heterobifunctional and homobifunctional crosslinking reagents. One of the disadvantages of using covalent binding is that linking chemistries are not always selective. For instance, if coupling is done between a surface and an antibody and the lysine group is targeted, random orientation of the protein could be the product because this amino acid is found throughout the antibody structure.

1.3.1.2.3 Bioaffinity Immobilization

The immobilization of proteins through biochemical affinity reactions presents an advantage over the other immobilization techniques presented because this method provides oriented immobilization of the protein of interest. The idea being that not only the immobilization of the protein is achieved but also it allows the researcher to detach proteins and use the surface more than one time for different assays [40]. The most common system used for this purpose is the biotin-avidin/streptavidin system, which is a very strong non-covalent bond with an affinity ~ 10^{15}. Such a strong bond allows the use of harsh biochemical assays [37].

Avidin can bind with up to four molecules of biotin and this glycoprotein is soluble in aqueous solution. The bond between avidin and biotin is not affected by pH, temperature or organic solvents [45]. On the other hand, biotin is a small molecule and its conjugation to macromolecules does not affect its functionality. The use of sulfo-NHS of biotin is employed to target amine groups on surfaces (e.g. aminopropyltriethoxysilane) [46, 47].

1.4 Electrical and Electrochemical Impedance Sensors

1.4.1 Impedance Spectroscopy

The characterization of the electrical properties of materials, conducting or semiconducting electrodes, and their interfaces can be done using a very sensitive technique known as impedance spectroscopy. The use of impedance spectroscopy allows the investigation of the dynamics of bound or mobile charges in the bulk or interfacial regions of conductors, semiconductors and even insulators [48].

The general approach is to apply an electrical stimulus (i.e. AC voltage or current) to the electrodes and measure the response (resulting AC current or voltage) [48]. The applied AC voltage is sinusoidal given by (1), where ω is the radial frequency and V_m is the peak voltage. The current (e.g. response to the voltage stimulus) is characterized by the amplitude, I_m and the phase shift, φ as seen in (2).. In impedance based biosensors the applied AC voltage is small (c.a. 10 – 25 mV) because the I-V relationship is linear only for small perturbations [49]. Likewise, the probe molecules should not be disturbed (covalent bond energies are ~ 1-3 eV), which can be easily achieved with impedance spectroscopy.

$$V = V_m \sin \omega t \tag{1}$$

$$I = I_m \sin(\omega t + \varphi) \tag{2}$$

The ratio of V_m / I_m and the phase ϕ are used to determine the impedance of the device under test, represented as a complex number, as in (3), with magnitude and phase:

$$Z = R + jX \tag{3}$$

$$|Z| = \sqrt{R^2 + X^2} \text{ and } \varphi = \arctan X/R \tag{4}$$

If the voltage is applied at different frequencies an impedance spectrum is obtained. This is displayed in a Nyquist plot, that shows the imaginary component of the impedance on the y axis and the real component on the x axis and in a Bode plot.

Specific regions of the spectrum can be linked to characteristic frequency ranges linked to different phenomena that occur at the electrode interface [50]. The impedance spectrum is interpreted based on an equivalent circuit that best fits the data. The equivalent circuit usually consists of configurations of resistors and capacitors in series, parallel, or both. In Figure 5 we present the two main equivalent circuits used. The differences between the circuit in Figure 5a and Figure 5b is the inclusion of the Warburg impedance Z_w. This impedance is considered when a faradaic sensor is built due to the diffusion of charge that is transferred across the electrolyte/metal interface. For this reason, they require the addition of a redox species that will oxidize and reduce by the transfer of an electron to and from the metal electrode. On the contrary, non-faradaic sensors require no additional reagent and the value of R is ideally infinite but, in reality, that is not the case [51].

Figure 5 Common equivalent circuits used in impedance spectroscopy. a) Non-faradaic sensor b) Faradaic sensor. Adapted from [51].

The resistances in the circuit usually represent the solution resistance (R_s), which depends on the ionic concentration of the solution and the distance between the working and reference electrode. The charge-transfer resistance (R_{ct}) is due to electron transfer because of oxidation or reduction reactions at the electrode [51, 52].

The capacitance, C, can be modeled as the series combination of the electrode capacitance, C_{elec}, the modified surface of the electrode, C_s, and the double layer capacitance C_{dl}, as in (5). Because the double layer capacitance has a large value, its contribution is negligible. The value of C_s depends of the thickness of the modified layer and its dielectric constant given in (6), where ε is the relative dielectric constant, A is the electrode area and d is the layer thickness [53]. Because of the roughness of the electrode and other non-idealities of the surface, the system is modeled instead as a constant phase element with impedance $Y_o (j\omega)^{-n}$. Y_o is a proportionality constant, j=$\sqrt{-1}$ and n is -1<n<1, but it is typically between 0.7 and 0.9 [54].

$$\frac{1}{C} = \frac{1}{C_{dl}} + \frac{1}{C_{elec}} + \frac{1}{C_s} \qquad (5)$$

$$C_s = \frac{\varepsilon\varepsilon_o A}{d} \qquad (6)$$

The values of C, R_s and R_{ct} can be estimated using the Nyquist plot as seen in Figure 6. R_s and R_{ct} are obtained from the intercept with the Z' axis and C from the value of ω (2πf) at the value of Z" max. At low frequencies diffusion affects the mass-transfer control process, this is the Warburg impedance, Z_w with a phase of 45°.

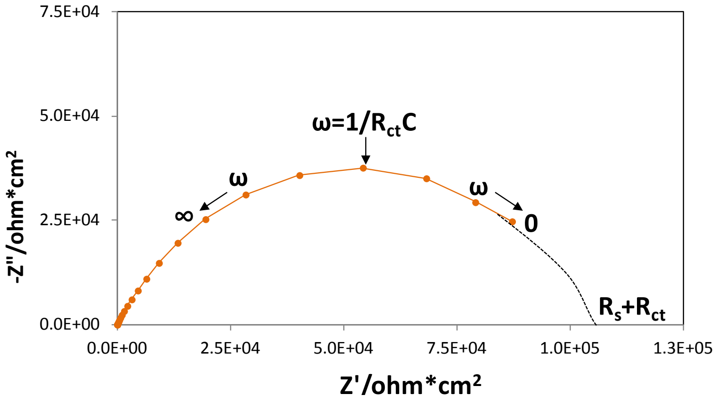

Figure 6 Nyquist plot for the equivalent circuit in Figure 5a.

1.4.2 The Double Layer Capacitance

When a metal electrode is polarized and is in contact with an ionic solution it attracts ions of opposite charge. Hence, an excess of ions buildup at the interface. Because of the accumulation of these ions at the interface, their concentration in the electrolyte decays exponentially and also the electric field produced in the vicinity of the metal/electrolyte interface [51]. This interface can be described as a capacitor whose plates are the metal surface and the ions adsorbed at the surface, which is commonly known as the Helmholtz layer. An adsorbed layer of water molecules at the interface separates the ions from the solid surface. The Helmholtz layer is formed by two planes: the inner Helmholtz plane formed by solvent molecules or ions in direct contact with the metal (i.e. specifically adsorbed), and the outer Helmholtz plane that is the region that is close to the solvated ions. There is also a diffusion layer in which ions in thermal motion counterbalance the charges in the Helmholtz layer, as illustrated in Figure 7. Outside the Helmholtz layer a region with excess ions of similar sign to the one in the outer Helmholtz layer exists. This region is known as the Gouy layer.

Because the distance between the metal surface and the adsorbed ions is so small (less than 1 nm), considering such a small distance in (6) the value of the capacitance is very high c.a. 50- 70 $\mu F/cm^2$ [52, 55]. If any coating covers the electrode, the double layer capacitance appears in series with it as was mentioned in section 1.4.1

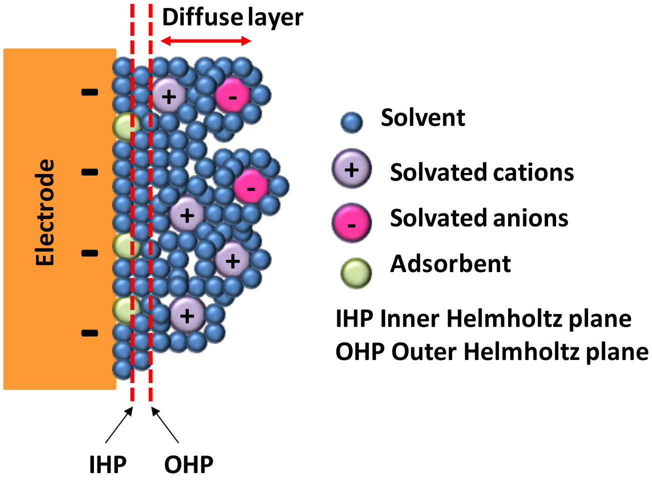

Figure 7 Simplified scheme of the Helmholtz layer that exists between an electrode and electrolyte solution. Based in [56].

1.4.3 Electrode Configuration

In impedance measurements there are two types of measurements that can be performed: One of them is electrical impedance, which is a two-electrode measurement performed with a working and a counter electrode, using a lock-in amplifier and frequency response analyzer (FRA). The counter electrode provides current to the cell and the working electrode provides measurements of the current through the cell. The electrodes may be of equal or different area [48, 57]. A two-electrode measurement is used to measure high impedance materials where the impedance of the cables is not significant [48].

The other type of impedance measurement is electrochemical impedance, which is a three or four electrode measurement, with a working, counter and reference electrode. The three-electrode measurement set-up is typically used in corrosion experiments while the four-electrode measurement technique is used with low impedance materials and to compensate for any voltage drop due to connections to the working electrode. Since the measurement is performed using a potentiostat, the reference electrode is used to reference the interrogating voltage that is applied to the cell [57]. In Figure 8, we present the basic instrumentation and set-up for an electrical/electrochemical measurements.

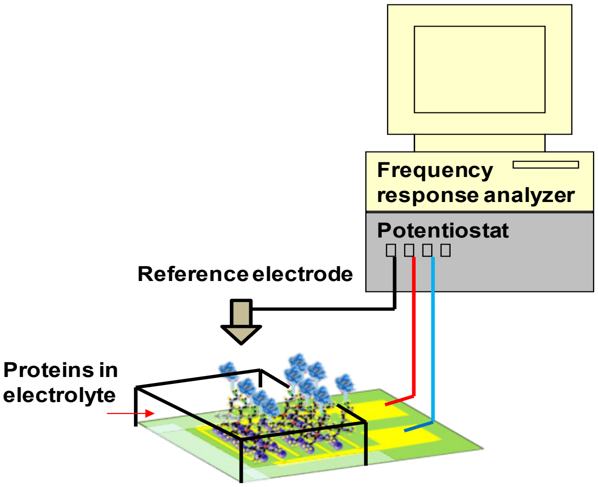

Figure 8 Illustration of the basic setup for the measurement of electrical or electrochemical impedance spectroscopy. A two-electrode impedance biosensor is shown connected to the FRA.

In an electrochemical cell the reference electrode maintains a fixed electrical potential between the working electrode and the solution. This allows a known voltage to be applied. A standard hydrogen electrode is the preferred option but a piece of wire can be used as a pseudoreference electrode and provides for a reproducible and stable potential in the cell [58].

1.4.4 Electrochemical Immunosensor

Electrochemical immunosensors are based on the detection of an immunoreaction using as a transduction method such as amperometry, potentiometry or conductometry which measures current, electrical potential or conductivity, respectively.

1.4.4.1 Amperometry Based Immunosensors

The principle of amperometric sensors is based on the measurement of a current flow generated by an oxidation-reduction reaction (redox) at a constant applied voltage. Since many proteins are not able to act as redox partners in electrochemical reactions, a catalyzing label of a redox chemical reaction is the target analyte at the sensing electrode [36, 59]. Enzymes such as horseradish peroxidase and glucose oxidase have been used as labels [60]. Some of the most popular amperometric sensors includes glucose electrodes and the detection of Escherichia coli in bacterial contamination of food [61, 62]

1.4.4.2 Potentiometry Based Immunosensors

Potentiometric biosensors measure the variation in charge-density on the surface of the electrode after a molecule has been bound to a surface or a catalytic process has taken place on it. This type of sensor operates at constant (almost zero) current [63]. Ion-selective field effect transistors (ISFET, a modified MOSFET) are based on the interaction of H ions from the solution and the surface of an insulating layer that induces an electric field in the transistor substrate between the source and drain. The substrate potential also changes with different analyte concentrations [59, 63]. An illustration of the basic structure of an ISFET device is presented in Figure 9.

Some of the applications include enzymatic-based reactions to detect urea, glucose oxidase, urease and pathogen detection [62, 64].

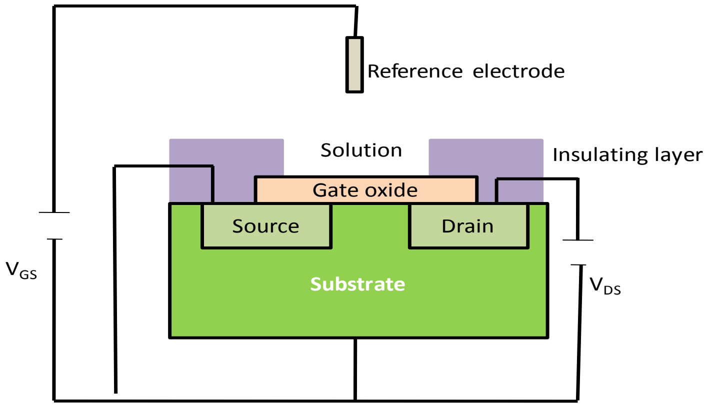

Figure 9 Schematic of a typical Ion-selective field effect transistor (ISFET) structure.

1.4.4.3 Conductometry Based Immunosensors

This type of sensor is based on the measurement of the electrical conductivity of a solution after the application of an electric field between two electrodes. The change in electrical conductivity is generated by biochemical enzymatic reactions that consume or generate ions. The mentioned enzymes are typically immobilized directly on two metal electrodes, usually Au or Pt [59, 63]. Conductometric devices are characterized by short response times, stability and ease of handling [36]. Few applications are available, including measurement of urea [65] and interdigitated microelectrodes (IDEs) that use conductive polymers to detect capacitance changes after enzyme modification [66].

Even though conductometric sensors are very precise for the detection of some molecules (e.g. urea detection) there are still issues to solve including reproducibility in complex biological solutions due to variations of pH and ionic composition [36].

1.5 Summary

The diagnosis and treatment of acute and silent myocardial infarction have concerned physicians for a long time. The development of strategies that could alert the patient and the medical specialist previous to a myocardial infarction event should greatly reduce the mortality risk. Materials that allow for the integration of sensing and drug delivery have a lot of potential to replace current diagnostic techniques. Semiconductor materials are ideal candidates as the substrate of such devices since they allow for the integration of ‘system on a chip’ platforms. In this work we present a study of the use of the electrical, chemical and polytypic properties of silicon carbide to build a sensor to diagnose acute myocardial infarction. Because this material has also shown biocompatibility and hema-compatibility properties, which will described in Chapter 2, there is a possibility that with the appropriate configuration it can be used in implantable applications to accurately detect silent myocardial infarction in real-time.

In this chapter we described the basic principles involved in building an immunosensor device for the mentioned purpose. Since this technique is based in cardiac biomarker recognition by an antibody, we explained the process to bind antibodies to a substrate and the basics of impedance spectroscopy as the technique to detect protein binding on the sensor structure.

This dissertation has been organized by chapters. In Chapter 2 we provide a short literature review regarding the versatility of SiC as a biosensor and biocompatible material. In addition, the physics principles behind building a potentiometric biosensor for detection of myocardial infarction are described. We explain the dynamics at the electrolyte/semiconductor interface and how the energy levels in the material are affected by it.

Chapter 3 covers the application of self-assembled monolayers (SAMs) on SiC, as the first layer in the immunosensor construction. We explore the use of SAMs, both to increase cell proliferation on 6H-SiC and to immobilize anti-myoglobin on 3C-SiC for the detection of myoglobin, one of the biomarkers related to myocardial infarction. We employed surface characterization techniques such as: XPS, AFM and surface water contact angle to characterize the functionalized surfaces and the quality of the anti-myoglobin immobilization process on 3C-SiC and the cell morphology on modified 6H-SiC.

Chapter 4 presents an overview of the development of a potentiometric sensor using 3C-SiC as the platform. We investigate the changes in the flat band potential of 3C-SiC after the surface modification with aminopropyltriethoxysilane (APTES) and the immobilization of different concentrations of myoglobin. We use Mott-Schottky plots and impedance spectroscopy to study the changes in the space charge region of the semiconductor that are affected by the charges of the antibodies and proteins immobilized on its surface. Finally, Chapter 5 covers the conclusions and future work that will lead into the construction of long-term cardiovascular SiC sensors.

CHAPTER 2: FUNDAMENTALS OF SILICON CARBIDE BASED IMMUNOSENSOR

2.1 Note to Reader

Parts of this chapter have been previously published [67] and are utilized with permission of the publisher.

2.2 SiC as a Biomaterial for Biosensors

The realization of bioelectronic devices based on wide bandgap (WBG) compound semiconductors has shown increased interest in recent years. The application of such materials for the realization of field effect transistors (FETs) [68, 69] are just one example of the multifunctional properties that make them promising materials in the fabrication of high performance microelectronic devices to interface with biological systems. One of the main concerns in materials research for biomedical applications is the search for materials that produce low or no adverse reaction when implanted in the body and that can therefore be implanted long-term. In the field of semiconductors, silicon (Si) has always been the preferred substrate material for micro-devices due to its low-cost and high-quality. However, it presents several drawbacks that limit its use in biomedical applications. Si has been used in Ion Sensitive Field Effect Transistors (ISFETs) for interfacing with neuronal networks or living tissue [70, 71].

Nevertheless, the implantation of a Si Utah probe in a cat's brain has resulted in a chronic astroglial response that limits the time of functionality of the device [72]. The fact that Si is also opaque to visible wavelengths limits its applicability in certain fields (e.g. retinal implants) and may be undesired in others, where optical inspection/sensing might be required (e.g.

labeled biomarker detection). In general, the properties of WBG materials are superior to those of Si for biological applications, and can yield long-term stability under chemically harsh environments and physiological conditions [69]. A few examples of the extensive use of some WBG materials in the biomedical field include: GaN and AlGaN which have proven to be chemically stable and naturally biocompatible [73]. AlGaN, AlN and ZnO present piezoelectric properties ideal to build resonator devices for high mass sensitive sensor devices and for biosensor applications [74, 75].

AlN-based light emitter devices (LEDs) are expected to emit in the deep UV (wavelength ~ 210 nm) which makes it appealing for the detection of small toxic and cancer causing particles [76]. Silicon carbide (SiC) possesses good biocompatibility [5, 77-79] in addition to high chemical inertness and can be used to make different types of electronic devices with similar processes used in Si processing. For example, gas sensors [68, 80] have been built, strong needles for organ transplantation monitoring [10] and Schottky devices for high power applications, which are commercially available [81], among others.

In this chapter we present a survey of the progress in SiC biosensor related research and the basics of semiconductor/electrolyte physics involved in semiconductor immunosensor construction.

2.2.1 SiC Polytypes, Synthesis and Preparation

SiC is a material that consists of the covalent bonding of Si and C atoms, in a tetrahedron form in which Si (or C) is the central atom. The high mechanical and chemical stability of the material are determined by the very short bond length, shown in Figure 10 and, hence, a very high bond strength is present in the SiC structure [82, 83]. It belongs to the class of wide band gap (WBG) semiconductors with band gap energy from 2.4 to 3.2eV depending on the polytype.

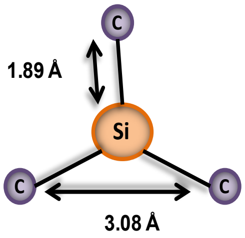

Figure 10 All SiC crystals are formed via bi-layers of C and Si, covalently bonded to form a tetrahedron that forms the basic building block of SiC, adapted from [84].

SiC can be formed in amorphous, polycrystalline and monocrystalline solid forms. It has more than 200 polymorphic forms, called polytypes, but 3C-SiC, 4H-SiC and 6H-SiC are the most readily grown and can be purchased on the market. The stacking order of the double layers of Si and C atoms defines the different polytypes of SiC. In Figure 11, the three different positions that the stacking sequence assumes in the lattice are reported as A, B and C, where k and h denote crystal symmetry points that are cubic and hexagonal, respectively. For example, 3C-SiC (or β-SiC), is the cubic form where the 3 delineates that 3 bi-layers of Si-C are needed to form the basic structure and C indicates that the crystal form is cubic. This polytype presents an ABC… sequence (Figure 11far right). 4H-SiC and 6H-SiC (α-SiC) are the hexagonal forms, where the 4 and 6 delineate that 4 and 6 bi-layers are needed while the H indicates that the crystal form is hexagonal. They have stacking sequences that are ABCB (Figure 11far left) and ABCACB (Figure 11 middle) for 4H-SiC and 6H-SiC, respectively.

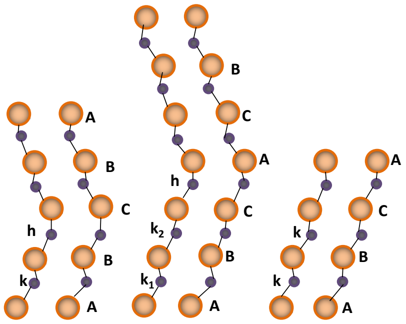

Figure 11 Atomic stacking sequence of the relevant SiC polytypes viewed in the 11-20 plane. From left to right, 4H-SiC, 6H-SiC, and 3C-SiC, adapted from [84].

Amorphous silicon carbide, denoted typically as *a*-SiC, is inherently insulating, it has high-K dielectric properties, high wear resistance, and works well as a durable coating, which is the product of the amorphous microstructure and low deposition temperatures used. The lower deposition temperature prevents any dopants that may be present during the deposition process from being electrically activated [85]. *a*-SiC is now being used as an inert encapsulating coating for *in vivo* prosthetics and it has been approved for commercial use as a coating for heart stents [86]. The deposition of *a*-SiC can be performed in a number of ways. including sputtering, chemical vapor deposition (CVD or PECVD) , and pulsed laser deposition (PLD) [85].

Polycrystalline materials consist of several small crystalline regions, called grains or crystallites, bonded together by crystallographically defective regions called grain boundaries. Grain formation in polycrystalline films grown using CVD processes is sensitive to several parameters such as temperature, deposition rate, dopant concentration, pressure, and impurity concentration. Unlike single-crystal SiC, poly-silicon carbide, or poly-SiC, can be grown on a wide variety of substrates, at lower temperatures (500–1,200 °C), and a wider set of processes exist compared to monocrystalline epitaxial film growth. Poly-SiC growth has been demonstrated on widely used surface micromachining substrates such as Si, Si_3N_4, and SiO_2 [87]. Likewise, the deposition of a poly-Si seed-layer on oxide to realize MEMS structures such as cantilevers and membranes can be easily released leaving behind high-quality 3C-SiC structures [88]. For the crystalline form of SiC the dominant application is power electronic devices, where the crystal of choice is 4H-SiC due to it having the highest band gap (3.2 eV) while 6H-SiC is ideally suited for solid-state lighting (LEDs) as its lattice constant is close to that of the GaN family of alloys used in advanced LEDs [84].

2.2.2 SiC a Unique Material for Biosensing

SiC’s electrical, mechanical and thermal properties determine its suitability as a biomaterial and biosensing substrate. It possesses high thermal conductivity, on par with copper at room temperature [89], its Young's modulus is higher than that of Si, and its high breakdown field ~ 2 MVcm^{-1} [90], is double than that of Si. SiC has been recognized as a viable material for applications involving high temperatures or hostile environments [89]. The chemical inertness of SiC suggests a high resistance to corrosion in harsh environments such as body fluids. In addition, its high elastic modulus, and low friction coefficient [91], make SiC an ideal material for smart-implants and *in-vivo* biosensors [92].

Compared to other semiconductors, SiC's wide band-gap increases its sensing capabilities. For instance, 4H-SiC presents a bandgap of 3.23 eV thus greatly reducing the number of electron-hole pairs formed from thermal activation across the band-gap, which allows high temperature operation of SiC sensors (indeed the intrinsic carrier concentration of SiC is ~10^{-6}-10^{-8} cm^{-3} while for Si is ~10^{10} cm^{-3}, more than 16 orders of magnitude lower than Si [91, 93, 94]). In addition to the fact that its refractive index is greater than that of other materials, such as diamond, its transparency to visible light and UV wavelength absorption, make it an ideal material for optical-based biosensing devices [95].

One of the main biomedical applications of SiC has been as a hard coating for non-fouling coronary heart stents [6, 7, 96, 97]. *In-vitro* and *in-vivo* tests done by Amon *et al*. showed that *a*-SiC on stainless steel stents had no cytotoxic reaction to L929 mice fibroblasts, and that there was no thrombus formation on stented vessels after blood perfusion for three days [98]. Moreover, they found that fibrin formation was significantly reduced at the *a*-SiC surface as compared with 316L stainless steel heart stents. Rzany *et al.*, exposed both 316L stainless steel uncoated and coated with *a*-SiC to circulating human blood for 15 min, and observed a dense fibrin network with incorporated blood cells on the metallic surface whereas only single thrombi and erythrocytes were observed on the *a*-SiC-coated surface [6]. In a two-year clinical study that was conducted on 300 patients using the BIOTRONIK (Germany) Tenax stent covered with *a*-SiC, the authors concluded that *a*-SiC stents significantly reduced early and late coronary events, possibly due to the attenuation of progressive endothelial cell growth at the site of intervention [97]. Several studies found similar results when implanting *a*-SiC stents with low rates of death, emergency revascularization, stent-related myocardial infarction and stent thrombosis [99-101]. For a complete review in the topic see [7].

SiC is also considered a popular material to be used as a passivation layer for prosthetic bone and hip implants. Biomorphic SiC ceramics are very promising as load bearing and base materials for dental and orthopedic implants, mainly due to its excellent mechanical properties. Will *et al.* [102] used biomorphous SiC that was processed from sipo wood by heating in an inert atmosphere and infiltrating the resulting carbon replica with a liquid silicon melt at 1450°C. After performing in-vitro experiments using simulated body fluid, the authors observed the formation of a bone-like apatite reaction layer on the biomorphic SiC surface [7]. On the other hand, Santavirta *et al.* [103] investigated the cytotoxicity of Ti based pins for hip replacement implants compared to coated SiC-Ti pins. By using a colony outgrowth inhibition test of JCRB0603 cells, they found that SiC-Ti particles did not inhibit colony outgrowth [103]. In their work, Saki *et al.* [104] investigated the viability and cell attachment of osteoblast like cell (Saos-2) on a ceramic bio-scaffold of hydroxyapatite-alumina and SiC (HA-Al_2 SiC). Cell growth and viability studies using trypan blue showed that the scaffold is able to support osteoblast attachment and growth, with 89% of the cells harvested alive on the scaffolds compared to 97.5% of the cells harvested from tissue culture polystyrene after one week. [104].

It has been reported in the literature that some SiC-based whiskers and powders show a certain degree of toxicity [105]. For this reason, it is necessary to understand what form of SiC is needed for a particular application because SiC shows different biocompatibility trends according to the SiC type and the organism that it is brought in contact with [5]. Svensson *et al.* have studied the toxicity of asbestos and compared the hazardous crocidolite to SiC whiskers by studying the cloning efficiency of V79 cells [105]. These authors concluded that if the materials are not handled or processed properly they can exhibit high cytotoxiciy levels, dependent also on the concentration of the material. Nevertheless, Rödelsperger and Brückel demonstrated that carcinogenicity of SiC based particles is related to the shape and size of the fragments; whiskers being carcinogenic while granular SiC has a lower carcinogenic potency [106]. Bluet *et al.*, reported on a selective cytotoxicity of 3C-SiC QDs *in-vitro* to epithelial and cancer cells. They investigated AT-84 cells, derived from oral squamous carcinoma as well as HSC-2 cells and S-G cells which are immortalized gingival epithelioid cells. The authors observed that significant changes of the AT-84 cells occurred after incubation with the SiC-QDs with indented borders and irregular shapes. Using MTTs assays they were able to show that treatment of the cells with 10 µg/ml and 50 µg/ml of NPs did not affect their viability after 72 hrs, however this was not so for the immortalized epithelioid cell line, which suggests the potential of SiC QDs as anti-tumoral agents [107].

Other authors have found that the effect of single crystalline SiC on cells or tissues proved to be non-invariant. The fact that SiC can be formed in different polytypes, as explained before, could be one of the reasons for this behavior. For instance, Colleti *et al.* tested the biocompatibility of crystalline SiC using *in-vitro* techniques with B16-F10 mouse melanoma, BJ human fibroblast, and human keratinocyte (HaCaT) cell lines, and found that there was qualitatively no difference between 3C, 4H- and 6H-SiC in terms of cell viability and proliferation [77]. An *in-vitro* study performed by Frewin *et al.* on 3C-SiC and nanocrystalline diamond with PC12 (rat pheochromocytoma) and H4 (human neuroglioma) cell lines showed superior lamellipodia permissiveness on 3C-SiC compared to Si. But the cells on the other polytypes, 6H- and 4H-SiC, showed reduced cell viabilities and substrate permissiveness [78, 108]. The same group also investigated biocompatibility of 3C-SiC *in-vivo* using C56BL/6 mice. They compared the response of 3C-SiC against Si at 5, 10, and 35 days after implanting the materials in a wild-type mouse's brain. Using CD45 dye to observe the activation of microglia and macrophages, the authors showed that the 3C-SiC surfaces revealed limited immunoresponse and significantly reduced microglia compared to the Si substrate [109].

It has also been determined that less biofouling and platelet aggregation occurred on 3C-SiC when exposed to blood, which can be an advantage for bioelectronic device fabrication. Schettini *et al.*, concluded that 3C-SiC is a hema-compatible material compared to 4H- and 6H-SiC which did not show the same behavior. In fact 4H- and 6H-SiC were similar to Si, a known non-hema-compatible material [110]. The different responses of the skin, brain and blood cells to the three popular SiC polytypes may be attributed to the surface charge, roughness and the chemical properties of the surface. Clearly it is very important to know which form of SiC is being exposed to biological matter as it may indeed affect the biological response.

Finally, implantable biosensors formed from 3C-SiC, while bio-benign, must also adopt approaches to address the challenges of chronic indwelling biocompatibility. Among these are; design approaches that eliminate sharp edges that will otherwise be a source of tissue irritation that provoke the inflammatory response [111], surface modification with biomimetic chemistries such as polyethylene glycol (PEG) and methacryloyloxyethyl phosphorylcholine (MPC) that have been shown to resist extracellular matrix protein adsorption/denaturation [112, 113], the use of bioresponsive hydrogels [114] in support of the chronic release of anti-inflammatory and immunosuppressant drugs such as dexamethasone [115, 116] and the release of factors such as vascular endothelial growth factor (VEGF) that promotes vascularization [117] and basic fibroblastic growth factor (bFGF) that promotes angiogenesis [118]. These approaches are among those actively under investigation as a means to limit fibrotic encapsulation [119] of implantable biosensors [120].

The major advantages of 3C-SiC in biosensor applications are its chemical inertness and thus likely robustness to wear and oxidative degradation following implantation. The ease and reproducibility of quantitative surface modification and functionalization also supports quantitative immobilization of biomolecules leading to high reproducibility and a likely low coefficient of variation in bioanalytical applications. The principal disadvantage is its cost due to the high growth temperatures needed to form the material as well as the lack of wet-chemical etching (indeed, a benefit in terms of material stability) which poses some challenges in the device fabrication arena.

2.2.3 Biosensor Configurations Employing SiC

From the device design perspective, SiC has been considered an ideal material for power devices and systems. However, as we have described in the previous sections, its properties also make it suitable for biomedical applications. For the construction of biological MEMs devices, 3C-SiC is the material of choice because it is less expensive, less polar than other SiC polytypes and is grown on Si which permits the implementation of the processing techniques used for that material [121, 122].

Depending on the device to be built, the different forms/polytypes of SiC provide specific advantages.

Table 1 Main sensors application and SiC polytype and requirements, adapted from [95].

Device application	SiC polytype/form	Material criteria for application
Biomedical sensors	Semi-insulating hexagonal polytype (4H-SiC /6H-SiC)	- Transparency - Low leakage (at room temperature)
	Porous hexagonal polytype (6H-SiC)	- Thick free standing layers
	SiC (amorphous) coating	- Biochemical inertness
Hall and temperature sensors	Semi-insulating 4H-SiC with epilayer	- Low leakage (at high temperature)
MEMs-NEMs resonators	Heteroepitaxial (3C-SiC)	- Low gradient and in-plane stress
Pressure sensors, accelerometer, HT gas sensors	Heteroepitaxial (3C-SiC)	- Low gradient and in-plane stress - Appropriate electrical characteristics

For instance, for biomedical devices that require low leakage and/or biochemical inertness one polytype may prove to be superior while films needed for the construction of MEMs devices demand certain mechanical properties and processing tools that may favor a difference polytype. In Table 1 we provide a list of the typical applications with the potential for success and the material type recommended, based on the work of [95].

2.2.3.1 Electrically-Based SiC Biosensors

The electronic properties of SiC have made it a suitable material for biomedical devices, especially those that are based on a surface impedance change or are electrochemistry related. For these particular applications, doping level, surface termination and choice of SiC polytype play an important role, since the background current and voltammetric reactivity of SiC electrodes would be affected. When SiC is appropriately doped, the conductivity of this material dramatically increases and exhibits electrical characteristics similar to carbon materials [123]. But in contrast to carbon, the close-packed hexagonal or cubic-SiC structure should afford a well-defined surface for electron transfer [124]. Thus, the use of doped SiC as an electrode material has not been widely researched for electrochemistry based applications. In the work performed by Hume and Kolthoff, a SiC electrode was used as an oxidation-reduction indicator electrode in potentiometric titrations of potassium iodide with permanganate and with ceric sulfate of ferrous iron with permanganate, of titanous chloride with ferric chloride, and of hydrochloric acid with sodium hydroxide [125]. The electrodes were made with single crystal SiC and their behavior was studied by measuring their potential against a calomel electrode. The authors concluded that the SiC electrode behaved similarly to an oxidation-reduction indicator material such as Au and Pt. Meier *et al*. implemented a chemical vapor deposition method using tetramethylsilicon and a resistively heated carbon fiber to produce a concentric SiC conductor that proved to be suitable for voltammetric measurements [126]. They found that the SiC electrode in 0.1 M H_2SO_4 showed a wide potential window, free from interference from +1.4 V to -1.2 V vs. a Ag/AgCl electrode.

Singh and Buchanan built a SiC-C fiber electrode for detection of electroactive neurotransmitters, namely dopamine and vitamin C [127]. The fabrication of this electrode was based on an electrolytic etching technique developed by the authors. The SiC provided insulation near the carbon tip and highly localized charge transfer, stiffness and protection by inhibition of O_2, H_2O and ionic diffusion. The sensing of dopamine hydrochloride and vitamin C was done by voltammetric and impedance spectroscopy techniques, monitoring oxidation currents that varied linearly with their concentration. They also recorded in-vivo action potentials from anesthetized rat brains with very high signal to noise ratio. Wu *et al*. also worked on the detection of ascorbic acid (AA) and dopamine (DA) [128]. In their study they were able to resolve the overlapping voltammetric responses of AA, DA and uric acid (UA) on a SiC-coated glassy carbon (GC) electrode, and the selective determination of DA in the presence of AA and UA with a sensitivity of 16.9 A M^{-1} cm^{-2} and a detection limit of 0.05 µM [128].

Salimi *et al*. used SiC nanoparticles to modify a GC electrode to detect insulin concentrations via electrocatalytic oxidation [129]. Using cyclic voltammetry, differential pulse voltammetry (DPV) and flow injection analysis (FIA), the authors found a dynamic linear range of detection up to 600 pM, sensitivity of 710 $pApM^{-1}cm^{-1}$ and a detection limit of 3.3 pM. Their electrode demonstrated high sensitivity, excellent catalytic activity, short response time, and long term stability [129]. A superoxide dismutase (SOD) biosensor based on SiC nanoparticles has been reported by Rafee-Pour *et al*. The characterization and analytical performance of the biosensor was based on direct voltammetry and amperometry of immobilized SOD onto the surface of a GC electrode modified with SiC nanoparticles. They found that the response of the sensor was stable after 24 hrs. of storage in a pH 7 solution, perhaps due to the chemical stability of the SiC film. In addition, they demonstrated that the sensor presented a sensitivity of 1.46 $nA{*}\mu M^{-1}$ and 1.375 $nA{*}\mu M^{-1}$ with a detection limit of 1.66 µM and 1.4 µM for cathodic or anodic detection of superoxide, respectively [130]. In the recent years, research has been focused on the detection of DNA bases via electrochemical methods on SiC modified sensors. Ghavami *et al*. implemented a glassy carbon (GC) electrode modified with SiC nanoparticles for simultaneous determination of DNA bases using differential pulse voltammetry (DPV) [131].

They found that no specific electron transfer mediator or reagent was necessary to build the biosensor. The detection limit of the GC/SiC electrodes toward guanine (G), adenine (A), thymine (T) and cytosine (C) determinations were 0.015, 0.015, 0.14, and 0.14 μM, respectively and the sensitivities were 0.3877 0.3289 0.0175 and 0.0499 μA/ μM, respectively. The sensor exhibited good stability, reproducibility and long lifetime [131]. Yang *et al*. presented the surface modification of nanocrystalline SiC with diazonium salts via electrochemical methods for later DNA bonding with a nitrophenyl film to the modified electrodes [132]. They showed that the modified electrode presented a wider potential window and lower background current than GC electrodes. The authors also demonstrated successful DNA immobilization on the modified SiC surfaces using Cy5 labeled cDNA with increased red fluorescence on the nitrophenyl|SiC surfaces compared to the bare SiC. Likewise, the voltammogram of hybridized DNA indicated the presence of target DNA [132].

Godignon's group has focused their efforts on developing temperature and impedance based sensors on SiC. Mainly needles for open heart surgery monitoring or graft monitoring of organs during transplantation and transportation. They concluded that the control of the surface properties of the material is a challenge when building biomedical devices [95] . Their impedance microsystem consisted of four Pt electrodes on an isolated semi-insulating SiC substrate. A Pt serpentine conductor served as the temperature sensor with the aim of distinguishing impedance changes due to either tissue or thermal effects. In their work, the authors also identified the advantages and potential of using SiC for DNA polymerase chain reaction (PCR) electrophoresis chips because of the high electric field strength and resistivity of semi-insulating SiC, in addition to its high thermal conductivity [95]. The same group expanded the description of myocardial ischemia monitoring probes and transplantation organ/tissue ischemia monitoring with SiC impedance based needles in the articles by Pascual *et al*. [133], Gabriel *et al*. [10] and Gomez *et al*. [134]. The article by Pascual *et al*. focuses on the fabrication, packaging and mechanical properties of the devices for such application, whereas the last two also consider the electrical characterization of the probes.

In their study, Pascual *et al*. described the fabrication of the needles on both 6H-SiC and 4H-SiC wafers with four Pt electrodes insulated from the substrate and passivated with SiO_2 and Si_3N_4 layers including the temperature sensor structure described above. The mechanical tests they performed included simulations with ANSYS 5.6 and an INSTRON 4464 system to test compression and bending of the needles. The authors also determined the forces needed to penetrate heart tissue. The values obtained were 1.32 N, which was lower than 1.35 N for Si. Likewise, the maximum bending force that could be applied to the needle tip without breakage of the same was 17.4 N compared to 16.4 N for Si. The fact that the needles fulfill the mechanical requirements for this application are an indication of the possibility of using these types of probes to reduce organ bleeding upon needle insertion [133].

In terms of the benefits of using SiC as ischemia monitoring probes, both Gomez *et al*. [134] and Gabriel *et al*. [10] concluded that there is less leakage current in a SiC impedance sensor compared to Si-based devices that present current leakage paths across the substrate at high frequencies (i.e. above 5 kHz), which generates a false impedance change [134]. In fact, Gomez *et al*. compared in-vitro experiments of four electrode measurements in 0.09% or 0.9% NaCl from 10 Hz to 1 MHz with a modified in-vivo system where the probes where placed close to the cortico-medullar junction of male Wistar rats (Ifa Credo) and measured the impedance in the 100 Hz to 100 kHz range. They demonstrated that the operating range of SiC-based impedance probes can be extended up to the 100 kHz range with the possibility of performing multi-frequency analysis and the creation of more accurate frequency-dependent analytical models of impedance [134]. Besides performing in-vitro characterization of the device, Gabriel *et al*., presented in their article an extensive mechanical analysis of the Si and SiC wafers used to build their probes [10]. They confirmed the values for hardness, elastic modulus and fracture toughness of the SiC and Si substrates but also the modulus of rupture for the fabricated probes. They emulated real-life conditions in a deflection test whereby they anchored the needle at one end and applied force from the nanoindenter on the other. The critical load at which the SiC needles fractured was 2.5 times higher than for Si needles (1053±200 mN vs. 452±37 mN). In addition, they found a modulus of rupture 4 times higher for SiC needles than that of Si needles (774 MPa vs. 188 MPa), which demonstrated the superior mechanical and electrical properties of SiC for impedance based needle probes [10].

Multi-electrode arrays (MEAs) with semi-insulating 6H-SiC have also been demonstrated by Godignon *et al.* In their article, the authors describe the construction of a 16 electrode MEA with locally grown carbon nanotubes (CNTs) on Pt electrodes to improve the electrode to medium impedance and growth of neurons on the MEAs. A reduction in the electrode impedance was obtained with CNTs grown on the Pt electrodes compared to bare Pt electrodes. In addition uniform CNT growth on SiC based MEAs was achieved because of the better temperature uniformity on the material.

In the same work the authors describe the material considerations to build a micro-fluidic chamber with 3C-SiC on silicon-on-insulator (SOI) wafers, for magnetic resonance imaging (MRI) equipment [121].

The area of Field Effect Transistors (FETs) on SiC has not been significantly exploited for biological applications. FETs made of SiC can function at high temperatures, in particular FET-based gas sensors that operate around 1000°C have made use of this property [9]. Also, prototypes and commercially available devices can be found that operate at very high frequency, high power and in harsh environments, such as Schottky devices from Infineon Technologies (Germany) [81], UV flame detectors from General Electric (U.S.A.) [135] and gas sensors developed by SenSiCAB (Sweden) [136] . The possibility to integrate SiC and grow other materials on its surface, for example AlN that enables a wider bandgap of ~ 6 eV (depending on the polytype), allows the integration with resonators on the same chip [68]. Lloyd Spetz *et al.* reported the measurement of NO, an interesting gas to measure due to its participation in the metabolism in an individual's breath [137]. They proposed a multifunctional sensor device with an integrated transistor, resonator and resistivity change measurements. A heterostructure that may be realized, for example SiC|ZnO, as in Figure 12, can provide biosensing based on the current change between the source and drain as a function of the gate voltage after immobilization of biomolecules in the gate area. A FET biosensor of this type, responsive to E_H changes in the environment modulated by a biological reaction, is known as an ion specific FET (i.e., ISFET) device. An ISFET is in essence a transistor without a gate electrode that requires an external reference electrode for operation. For this reason, the authors investigated a preliminary device using a MOS (metal on semiconductor) structure using Ti/Au, Al_2O_3 and a Si substrate [137].

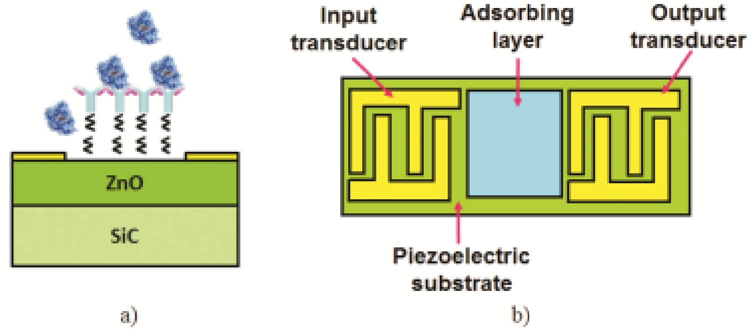

Figure 12 Scheme of a sensor device that includes a transistor, a resonator and resistive measurements between the finger electrodes. a) Side view and b) Top view of the device proposed by [137].

2.2.3.2 Optically-Based SiC Biosensors

As was mentioned in Section 2.3, SiC also presents appropriate optical properties to develop biocompatible optical based detection sensors. In particular, quantum dots (QDs) have proven to be a growing research field for SiC. QDs are interesting tools for cell tagging because of their properties including: their size and tunable emission spanning from the ultraviolet to the near infrared, the high extinction coefficient combined with a comparable quantum yield to fluorescent dyes, and resistance to photo-oxidation (i.e. photobleaching) [138]. Botsoa *et al*. bio-imaged living cells with SiC QDs. They fabricated 3C-SiC nanoparticles by means of electrochemical anodization of a low resistivity 3C-SiC polycrystalline wafer and subsequent grinding and centrifugation to collect particles less than 10 nm in size. Different concentrations (0.1 to 2 g/l) of the SiC QD suspension was added to 3T3-L1 fibroblasts and incubated for 15 hrs. and then analyzed with fluorescent microscopy, using UV/violet excitation. The authors found that the QDs are strongly localized inside the cells, mainly at the nucleus and they noted a heterogenous distribution of the fluorescent intensity. The cells were also incubated for one week with QDs and were found to be alive, which evidenced the non-toxic effect of the 3C-SiC particles to the cells [138]. Another material that is showing good promise as an optical biosensor substrate is amorphous SiC, or *a*-SiC.

Caputo *et al*. have reported on a two-color *a*-Si/a-SiC photosensor for DNA detection. The sensor is based in the detection of DNA strands labeled with two fluorochromes (Alexa Fluor 350 and Cy5) using a p-i-n-i-p *a*-Si/*a*-SiC stacked structure that basically detects different spectral regions depending on the voltage applied to the diode structure [139]. They used a UV radiation source that excited the biomolecule markers inducing fluorescence; the re-emitted light that passed through a glass/TCO layer and was absorbed by the *a*-Si/*a*-SiC photosensor producing a photocurrent that was proportional to the quantity of fluorochromes present. In this work, the authors reported detection limits of 10 nmol/l and 400 nmol/l for Alexa Fluor 350 and Cy5 labeled DNA strands, respectively [139]. But SiC can also be used for biological imaging in fluidic environments. Taubner *et al*. reported the successful development of a 3C-SiC based superlens for near-field scanning optical microscopy (NSOM) [140]. A free standing 440 nm thick 3C-SiC film grown on a (100) Si substrate is the core of the superlens with a 220 nm thick SiO_2 film that allows the thin film superlens to be displaced at the required distance (~880 nm) from the specimen when applying the NSOM technique. The use of a SiC superlens structure allowed them to enhance the spatial resolution of the subsurface features by a factor of 4 compared with near-field imaging without superlensing of the SiC slab. The possibility of incorporating a 3C-SiC superlens to a microfluidic device could enable in-situ NSOM imaging of biological samples. An evanescent waveguide structure microfabricated in SiC on Si substrates was recently reported by Pandraud *et al*. Interestingly, the relatively large index of refraction of *a*-SiC, compared to similarly-deposited Si_3N_4 and SiO_2, enhances the ability of the waveguide structure to sense chemicals. The authors concluded that surface roughness of the *a*-SiC is such that the propagation loss was reduced to 1–5 dB/cm [141].

2.2.3.3 SiC MEMs Biosensors

The mechanical, chemical and electrical properties of SiC that were described in the previous sections also make SiC an attractive structural material for MEMS and NEMS applications. SiC MEMs have been typically used in applications that include harsh chemical, high-radiation or high-temperature environments; for which Si is not suitable. The evaluation of MEMs materials performed by Kotzar *et al*., demonstrated the biocompatibility of seven MEMs materials including single crystal 3C-SiC [79]. The materials were evaluated using a baseline of the ISO-10993 standard for physicochemical and biocompatibility tests. The main focus of the article was to understand the effect of sterilization on the material surface and its cytotoxic effect by culturing L-929 mouse fibroblast cells on the surfaces for 48 hrs. The authors showed that neither Si_3N_4 nor SiC elicited significant non-biocompatible responses which renders them suitable for future BioMEMs applications [79].

The high Young’s modulus of SiC enables the fabrication of wide frequency resonators. Until now, this has been the main structure developed and studied on 3C-SiC, with cantilevers or bridge structures that could be very useful for mass detection, gas sensing or biomolecule identification [95]. SiC membranes vary in thickness and typically a 2 µm-thick membrane is able to withstand pressures of over 100 PSI without breaking. For practical, long-term micromachined BioMEMS pressure sensors, one would need to incorporate biocompatible and antifouling characteristics [122]. *a*-SiC is also an attractive material for MEMS and NEMS applications because it retains the mechanical and chemical durability of its crystalline counterparts [142], while being electrically insulating and being processed at much lower substrate temperatures. Its electrically insulating properties enable its use for dielectric isolation instead of SiO_2 and Si_3N_4. Typically *a*-SiC is used as an etch mask for bulk micromachining as in the work by Iliescu *et al*. [143] where *a*-SiC is implemented as a protective mask to increase the etching resistance towards SiO_2 with the aim to fabricate microfluidic channels. In some cases, *a*-SiC is used as a planarizing membrane to cover the microchannel. Later, Iliescu *et al* studied the use of 2.5 μm low stress a-SiC membranes for cell culture, potentially valuable for bioMEMs applications. They pre-treated micromachined *a*-SiC membranes with 40% NH_4F and incubated NIH3T3 fibroblasts for 24 and 48 hrs on the membranes. Using microscopy they found that the cells proliferated more on the *a*-SiC membrane than on monocrystalline SiC [144].

2.3 Electrochemistry of Semiconductors

In this work we aim to use Silicon carbide (SiC) as an electrode that will produce a change in its electrical properties after protein binding for the diagnosis of acute myocardial infarction. The use of SiC for this purpose requires the understanding of solid state physics and electrochemistry because phenomena associated with both disciplines will be seen in the SiC/electrolyte (e.g. Phosphate Buffered Saline) system. In this section we will present a brief introduction to the semiconductor physics content related to semiconductor electrochemistry.

2.3.1 Energy Levels in Semiconductors

A semiconductor is characterized by electron energy levels which are described by energy bands. In all semiconductors there is a forbidden energy region or gap in which energy states cannot exist in the absence of crystal defects. This energy gap (i.e. the semiconductor band gap) determines the properties of the material. Energy bands are only permitted above and below this energy gap. The upper bands are called conduction bands and the lower ones are called valence bands [145].

Electrons can be excited to the conduction band thermally, optically or photochemically. In order to achieve doped semiconductor films, an additional element is introduced into the semiconductor such that these processes are satisfied at low temperatures (ideally below room temperature). For example, the addition of P in a Si crystal introduces occupied energy levels into the band gap close to the lower end of the conduction band, which allows for an easier promotion of electrons to the conduction band [146]. Thus P doped Si is n-type due to the fact that the conduction band is populated with electrons independent of device electrical bias, surface charge and band bending.

2.3.1.1 Fermi Level and Band Bending

The Fermi level (E_F) is defined as the energy level at which the probability of occupation by an electron is 0.5. A more meaningful way to think of this is that this is the ‘halfway point’, meaning half of the electrons in the semiconductor are above and half below this value. For an intrinsic, or undoped, semiconductor the Fermi level is found at the mid-point of the band gap [146]. If the position of the Fermi level within the bandgap is known, the density of electrons and holes can be calculated from equations (7) and (8), where $E_{F,n}$ and $E_{F,p}$ are quasi Fermi levels for electrons and holes, respectively, n and p, are the density of electrons and holes, N_C is the density of states at the lower edge of the conduction band and N_V is the density of states at the upper edge of the valence band [145].

$$E_{F,n} = E_C - ln\left(\frac{N_C}{n}\right) \tag{7}$$

$$E_{F,p} = E_C - ln\left(\frac{N_V}{p}\right) \tag{8}$$

At equilibrium, the Fermi level is constant throughout the semiconductor. For an n-type semiconductor, the Fermi level lies above the midgap level and below the conduction band, whereas for a p-type semiconductor it is found below midgap and above the valence band (see Figure 13a. and b.). The Fermi level of a semiconductor varies with the applied potential; for example, moving to more negative potentials will raise the Fermi level [146].

Figure 13 Fermi level at equilibrium in a) n-type and b) p-type semiconductor. E_C and E_V are conduction and valence band edges, respectively.

2.3.2 The Electrolyte

Electrical current in liquid electrolytes is carried by ions that are formed by dissociation of salts like KCl or Na_2SO_4 in a suitable polar solvent, which is usually water. Both positive and negative ions are produced by dissociation and are found in equal concentrations in the water. For reference, electrolyte conductivities > $10^{-2}\Omega^{-1}$*cm^{-1} and with ion concentrations of > 10^{-1} M are required in order to achieve an adequate level of conductance in an electrochemical cell [147].

In term of electronic energy levels, an ion or molecule in solution presents a tendency to release (occupied level) or to accept (free level) electrons when the molecule approaches an electrode or another ion. The energy level model in electrolytes can be more complicated than the one of semiconductors, because of the interactions of ions with the solvent and thermal fluctuations. As a result of thermal fluctuations it is not possible to determine the exact energy of the ion at a specific time. Hence, ionic energy levels in solutions are described in terms of probability distributions, similarly to the case presented for semiconductors [148].

In Figure 14 the ideal probability distribution of the energy levels in the electrolyte is represented by two Gaussian functions centered at E_{ox} (potential of oxidizing species, i.e., accepts an electron) and E_{red} (reducing species, i.e., donates an electron). E_{redox} refers to a state where equal numbers of reducing and oxidizing agents are present in solution [148, 149].

$$E_{redox} = \frac{1}{2}(E_{red} + E_{ox}) \tag{9}$$

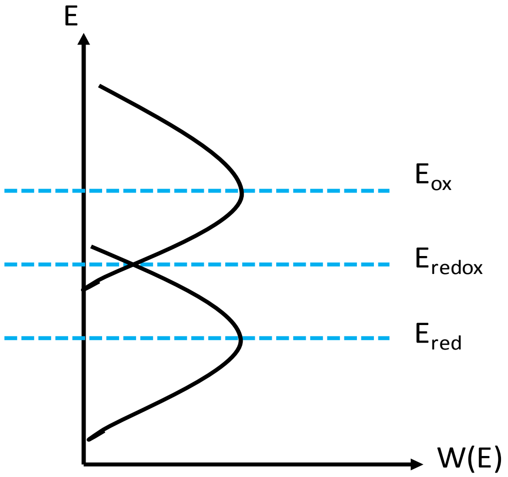

Figure 14 Representation of energy levels in a polar solution. Adapted from [148].

An effective Fermi energy in the solution is defined as E_{redox}. If equilibrium is reached with an electrode in solution the Fermi energy of the electrode will move to E_{redox} due to electron exchange with the redox couple [149]. This is the definition of equilibrium in the electrolyte/electrode (or semiconductor) system.

2.3.3 The Semiconductor|Electrolyte Interface

The distribution of charge and potential in a semiconductor and an electrolyte when they are brought into contact is similar to the case described in section 1.4.2. However, given that semiconductors have lower carrier density than metals, the counter charges described before are distributed below the interface and a layer known as the space charge region (SCR) in the semiconductor is formed [150]. The SCR in the semiconductor is in contact with the Helmholtz layer in the electrolyte which is followed by the Gouy layer as seen in Figure 15 [149, 150].

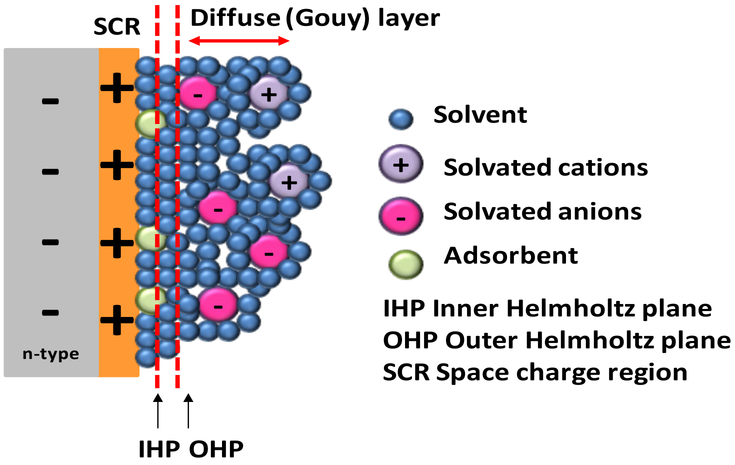

Figure 15 Double layer at the semiconductor|electrolyte interface.

The total charge at the semiconductor|electrolyte interface consists of the fixed charge in the SCR, the surface state charge, the charge of ions adsorbed in the Helmholtz layer and the ions in the diffuse, or Gouy, layer. The typical thickness of the Helmholtz layer is ~ 0.4-0.6 nm, the SCR is ~10-1000 nm and ~ 1-10 nm for the diffuse layer [150, 151]. Because the thickness of the SCR depends on the concentration of mobile charge carriers it is proportional to the Debye length. The Debye length defines the distance over which a charge imbalance (i.e. caused by an applied electric field) is neutralized by majority carriers under steady state or equilibrium conditions [152]. The Debye length is approximately 100 nm for semiconductors with a doping concentration of ~ 10^{15} cm^{-3} and around 10 nm in dilute 0.01 M ionic solutions [153].

The capacitance of this interface can be represented as the series capacitances in (10), where C_{SC}, C_H and C_d are the capacitance of the SCR, the Helmholtz and the Gouy layers, respectively.

$$\frac{1}{C}=\frac{1}{C_{SC}}+\frac{1}{C_H}+\frac{1}{C_\mathrm{d}} \tag{10}$$

For highly concentrated electrolytes (> 0.01 M) the contribution of C_d can be neglected [154]. For an ideal semiconductor|electrolyte interface the major potential drop will be across the space charge layer and the total capacitance of the system will be due to C_{SC}. In addition the values of C_{SC} are between 0.001-1 μF/cm^2 in contrast to those of C_H that are between 10-100 uF/cm^2 and the region with the lower capacitance tends to dominate the total capacitance of the system [155]. In the case when the semiconductor is degenerately doped (i.e. doping concentration is 10^{19}-10^{21} cm^{-3}) or when it is in accumulation the system behaves as a metal|electrolyte interface and C_H dominates the total capacitance in the system [151].

2.3.3.1 Space Charge Layer in Accumulation and Depletion

If a potential is applied to a semiconductor electrode in solution a reorganization of charges takes place until equilibrium is re-established. This means that the Fermi level in the semiconductor must equal the Fermi level of the solution. The Fermi level in the bulk of the semiconductor remains constant but the change in potential in the SCR produces a degree of bending at the edge of the conduction and the valence bands.

Three situations can be identified which are referred to as flat band potential (the bands are flat), depletion (the semiconductor surface is depleted of mobile charges) and accumulation (the semiconductor surface is full of mobile charges). When at the applied potential the Fermi level is equal to the redox potential of the electrolyte the flat band condition is achieved and there is no band bending (see Figure 16a). The potential is therefore known as the flat band potential. For an n-type semiconductor, if the applied voltage is anodic (positive potential) the SCR is depleted of majority carriers, the bands bend upwards and the SCR presents an excess of fixed positive charge (see Figure 16b). On the contrary, if the voltage is cathodic (negative potential), there is an accumulation of mobile charges in the SCR and the band edges bend downwards (see Figure 16c). When the semiconductor electrode is in accumulation it will act like a metal due to the high density of charges at the surface [155]. The thickness of the accumulation layer is typically close to 10 nm [149].

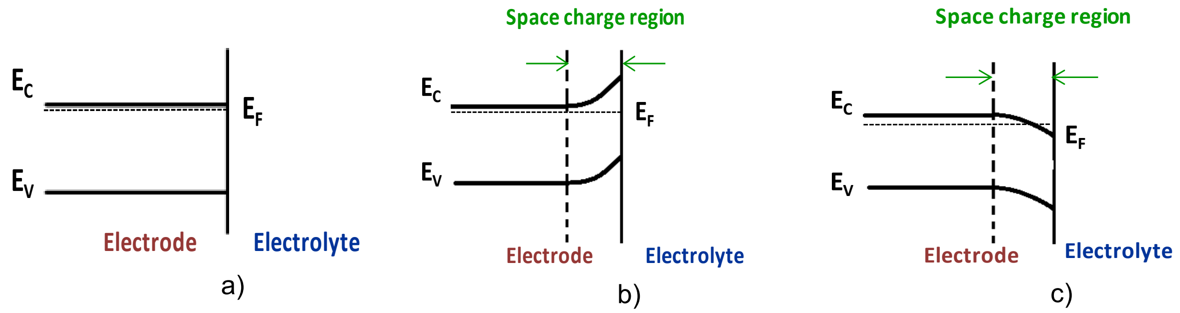

Figure 16 Band bending in an n-type semiconductor a) Flat band potential b) depletion and c) accumulation.

2.3.4 The Determination of the Flat Band Potential Using Mott-Schottky Plots

The measurement of the capacitance across the SCR provides important information about possible changes in the energy bands of the semiconductor due to the reaction with the electrolyte or when charged molecules are deposited on its surface. If the position of the band edges is of interest one can perform capacitance-voltage measurements, also known as Mott-Schottky plots [151, 155]. The Mott-Schottky relation for an n-type semiconductor is shown in equation (11). Where N_D is the doping concentration, ε_o is the permittivity of free space, ε is the dielectric constant of the semiconductor, q is the charge of the electron, T is temperature, k is Boltzmann's constant, V is the applied voltage and V_{FB} is the flat band potential at which the bands are "flat" across the semiconductor-electrolyte interface.

$$\frac{1}{C_{SC}{}^2} = \frac{2}{N_D \varepsilon \varepsilon_o q}\left[V - V_{FB} - \frac{kT}{q}\right] \qquad (11)$$

A plot of $1/C_{SC}{}^2$ as a function of the potential (vs. the reference electrode) should be a straight line with a slope proportional to the doping density and in which the intercept with the V axis equals the flat band potential [155]. The depletion width can also be determined using equation (12)

$$W = \frac{2}{N_D \varepsilon \varepsilon_0 q}\sqrt{V - V_{FB} - \frac{kT}{q}} \tag{12}$$

It is important to emphasize that there can be deviations from the ideal behavior presented in this section due to irregularities in the surface including surface roughness [156], non-uniform spatial doping and the presence of deep donor and acceptor impurities [151, 157]. Also, a contribution from the Helmholtz capacitance [158], ionic adsorption at the surface [159], presence of an oxide film [160] may also result in non-ideal behavior.

2.4 Summary

In the first part of this chapter we have provided an overview of the major types and possible applications of SiC for biomedical sensors. The possibility of the integration of other materials and systems on SiC increases the possibilities to create complex devices that can perform multiple biomolecule detection and analysis on a single platform. We also discussed several SiC material properties that put it in the advantage to be used as a biosensor substrate with respect to other materials. For instance, the remarkable chemical and mechanical properties, and the fact that SiC can be produced into different forms (e.g. BioSiC made from wood, *a*-SiC, nanoporous SiC, etc.), and polytypes (i.e. cubic, rhombahedral and hexagonal) make it suitable for a wide variety of applications.

After exposing the reasons to use SiC in electrically-based biosensors, the second part of this chapter dealt with the basics and physics behind the use of the Mott-Schottky technique which we plan to use to detect myoglobin on SiC sensor surfaces. We describe the principles behind the semiconductor|electrolyte interface since the measurement is based on the capacitance changes in the space charge region of the semiconductor. The concepts described both in this chapter and chapter 1 provide the basics for the promising technique to detect myocardial infarction using impedance and field effect based SiC biosensors.

CHAPTER 3: SIC FUNCTIONALIZATION

3.1 Note to Reader

The results presented in this chapter have been published [161-165] and are utilized with permissions of the publisher ("Reprinted with permissions").

Most biomolecule recognition-based systems require immobilization of specific molecules with controlled structural order and composition. A viable immobilization approach is covalent attachment [166]. Surface functionalization provides many advantages in the development of semiconductor based biosensors, including the control of the interfacial properties of the substrate material itself. In addition, surface functionalization is one of the main tools used for covalent biomolecule immobilization. It may be used for imparting molecular functionality to the substrate, thus enabling sensitivity towards chemical stimuli [167].

Self-assembled monolayers (SAMs) are composed of organic molecules that are covalently immobilized on the surface of the semiconductor via suitable linker groups [168-170]. In general, hydrogen- (H-) or hydroxide- (OH-) terminated surfaces provide the reactive sites necessary to obtain high quality monolayers. Hydrosilylation and silanization are two common surface functionalization processes that have been used extensively on Si substrates [167, 170, 171] and SAMs synthesized in this way have been analyzed in detail, with either suppression or enhancement of cell spreading and proliferation depending on the identity of the molecular end-group of the SAM [172].

Hydrosilylation of Si typically involves the attachment of long-chain alkenes to the surface of the H-terminated semiconductor through addition reactions, resulting in formation of Si-C covalent bonds with the surface [170, 173]. Silanization, on the other hand, requires an OH-terminated surface which can react with the alkoxy groups of organosilane molecules [167, 173]. The functionalization of SiC is possible using both alkenes and organosilanes, similar to the processes used for Si, but certain differences in the surface preparation must be addressed [168, 173-176]. Treating 6H-SiC (0001) with HF creates a nearly perfect OH-terminated surface [177]. Alkoxylation using alkenes is possible on OH-terminated surfaces via a Markovnikov addition reaction, but leads to a Si-O-C bonding configuration that is chemically less stable than direct Si-C bonding [173].

3.2 SiC Chemical Functionalization (SAMs)

Practical studies have been performed by different groups to gain insight into the bio-functionalization of SiC. Rosso *et al*. demonstrated successful alkyl monolayers covalently bound on HF-treated SiC surfaces, including 6H-SiC (0001) and 6H-SiC ($000\bar{1}$) and polycrystalline 3C-SiC, through thermal reaction [173] and UV irradiation [174] with 1-alkenes. They concluded that the attachment of alkyl chains on the SiC surfaces seemed to occur via the formation of an ether bond between a thin oxycarbide layer and the second carbon of the double bond. Their results included very hydrophobic methyl-terminated surfaces on flat SiC, which they showed to be stable under harsh acidic conditions (e.g., no change in water contact angle after 4 h in 2 M HCl at 90 °C), while their stability in alkaline conditions (pH 11 at 60 °C) also superseded that of analogous monolayers such as those on Au, Si, and SiO_2. Similarly, Schoell *et al.* demonstrated the covalent functionalization of aminopropyldiethoxymethylsilane (APDEMS) and octadecyltrimethoxysilane (ODTMS) on n-type 6H-SiC (0001) (i.e., Si-face) surfaces via wet chemical processing techniques [176]. Desorption temperatures in the range of

830 K proved the covalent bonding of the organic molecules to the SiC surface. They also immobilized fluorescence-labeled proteins on patterned APDEMS monolayers to prove the functionality of the surface and the wettability contrast obtained on a micropatterned ODTMS-modified 3C-SiC surface [176]. This group also developed a plasma-based method to passivate n-type 6H-SiC with chlorine and obtained almost flat band conditions on the 6H-SiC (0001) surface. Hence, they were able to perform successful ultraviolet light-induced grafting of trifluoroacetamid (TFAAD-protected long-chain ω-unsaturated amine (10-aminodec-1-ene)) and thermally induced alkylation with 1-octadecene on both 6H-SiC (0001) and 6H-SiC (000$\bar{1}$) [178]. Later, Howgate *et al.* focused on the impact of UV photocatalytic cleavage on n- and p-type GaN and SiC with covalently bound self-assembled monolayers (SAMs) formed from ODTMS. They found that significant and rapid photocatalytic degradation of the organic layer occurred on n-type GaN. Their results proved that the charge-transfer processes between semiconductors and organic systems depends on the positions of the conduction and valence band edges and can be tailored by appropriate choice of the semiconductor Fermi level [179].

Aghdassi *et al.*, investigated the suitability of octadecylsiloxane (ODS) on 6H-SiC (0001) as an insulating dielectric for electronic passivation of the surface. They used XPS, ultraviolet photoemission spectroscopy (UPS) and inverse photoemission (IPE) experiments and concluded that a large HOMO–LUMO energy gap of about 9 eV is present in the ODS-SiC system. Barrier heights of 3.3 eV and 2.7 eV were observed for electron and hole transport from the substrate into the adlayer and contributed to demonstrate their hypothesis. They also presented an extensive description of the electronic and structural properties of the silane-SiC interface [180].

Williams *et al.* also looked into the immobilization of proteins onto functionalized SiC. They demonstrated selective immobilization of streptavidin via biotinylation of 4H-SiC (0001) functionalized with APTES. The biotin-streptavidin is a strong bond (K_d, on the order of 4×10^{-14} M; ca. 425 pN) [181] that is routinely used as a model substrate for biomolecule detection. The authors found, using different characterization techniques that included XPS, ellipsometry, contact angle and fluorescence microscopy, that an optimization of the APTES layer was critical to the successful streptavidin immobilization, in addition to a biotinylation step prior to the streptavidin attachment to prevent non-specific binding of this protein with the 4H-SiC|APTES surfaces [182]. What is interesting in their work is that they present an alternative hydroxylation to the diluted HF dip step used by other authors, and employed instead a treatment with oxygen plasma (20% O_2/ 80% Ar) to grow a thin oxide followed by exposure to air for 2-3 hrs to allow for chemisorption of water molecules that facilitates the silanization process [182].

Petoral *et al.* reported on the surface functionalization with mercaptopropyltrimethoxysilane (MPTMS) of wide band gap semiconductors including SiC, ZnO, and GaN. They used n-type 4H-SiC (both 4H-SiC (0001) and 4H-SiC $(000\bar{1})$), and the MPTMS monolayers were prepared by evaporation of a pure solution in a sealed vacuum chamber for 1 hr. Using XPS and water contact angle measurements they observed the formation of a monomolecular layer of MPTMS on the SiC surfaces [183]. In addition, they immobilized an amino acid derivative pTyr-PT but only on MPTMS-functionalized ZnO and GaN surfaces. Yakimova *et al*. used a similar process to functionalize SiC and, in addition to MPTMS, also studied APTES films on 4H-SiC. They also evaluated the electrical contribution from the organic layers and their behavior as a possible insulator on SiC, similar to SiO_2. They used silver epoxy as a back contact and a thick probe as the gate contact. What they found was that the device exhibited a Schottky diode like I-V characteristic similar to a reference sample with no isolation layer and one sample with a 1 nm thick SiO_2 film [69].

Bhowmick *et al.* demonstrated the successful covalent functionalization of quartz and n-type 6H-SiC with APTES and benzo(ghi)perylene-1,2-dicarboxylic dye. The authors used XPS to show the presence of the APTES layer but concluded that not all amino groups of the APTES-functionalized surfaces reacted to bind the dye molecules [184]. They also found that the dye functionalization was not uniform throughout the surface, showing different island sizes of the dye and including different chemical environments on SiC. Nevertheless, their fluorescence lifetime measurements indicate the presence of more than one local environment for surface-bound benzo(ghi)perylene-1,2-dicarboxylic anhydride independent of the substrates and that the single-crystal SiC surface provided a more homogeneous environment than the quartz surface [184]. Protein-resistant SiC surfaces, to prevent device failure due to fibrous encapsulation, were investigated by Qin *et al.* The authors prepared films terminated with oligo(ethylene glycol) (OEG) via photochemical grafting onto 3C-SiC. By immersing the OEG coated samples in a 0.1% fibrinogen solution in PBS for 1 hr they determined, using the N-1s signal from XPS, that the OEG coating reduced the non-specific adsorption of fibrinogen on the substrates by 99.5% and remained resistant after storage in PBS for 4 weeks at 37.1°C [185].

3.3 Increased Cell Proliferation on Surface Modified 6H-SiC

In this section, we demonstrate that the proliferation and attachment of two immortalized neuronal cell lines can be enhanced after bio-functionalization of 6H-SiC using both hydrophobic and mildly hydrophilic SAM layers. The contrasting properties of the functionalized surfaces are shown to affect the cell response to the surfaces, which were assessed through the observation of PC12 and H4 cell proliferation and morphology.

3.3.1 Substrate Preparation

Two 6H-SiC off-axis n-type wafers (3.43º off-axis, Si (0001) face, 420 μm thick), purchased from Cree, Inc. were diced into 5x5 mm^2 die. A hydrogen etching process was first performed in order to obtain well-ordered, atomically flat surfaces free of polishing scratches and with reduced defect densities [186, 187]. The samples were then ultrasonically cleaned in acetone, methanol, and isopropanol, followed by a 10 min. immersion in piranha solution (H_2SO_4:H_2O_2 2:1). A sequence of oxygen plasma (2450 MHz, 200 W, 1.4 mbar) treatment and etching for 5 min in 5% diluted HF to obtain the hydroxyl (-OH) termination was performed twice before functionalizing the surfaces. The thermal alkylation process with 1-octadecene was performed directly on OH-terminated surfaces. For the silanization processes, using aminopropyldiethoxymethylsilane (APDEMS) and aminopropyltriethoxysilane (APTES), the oxygen plasma step was replaced with an HCl (1:2, HCl:H_2O) dip followed by a 5% diluted HF dip, the last step was performed to obtain the hydroxyl (-OH) termination.

3.3.2 Preparation of APTES, APDEMS and Octadecene on 6H-SiC Substrates

After cleaning and etching of the samples, alkylation of 6H-SiC (0001) was performed by reaction of the hydroxylated surfaces with 1-octadecene for 120 min at 200 °C under Ar. The samples were then ultrasonically cleaned in hexane, chloroform, and methanol for 10 min each. The silanization reactions were performed by immersing the samples in 10% APDEMS (or APTES) in anhydrous toluene for 90 min at room temperature in an N_2 environment, followed by ultrasonic cleaning in toluene and isopropanol, for 20 min each. After SAM formation, the samples were placed in ethanol to prevent bacterial growth and surface oxidation before cell seeding.

3.3.2.1 Methodology for Surface Characterization

Static water contact angle (SWCA) measurements were performed using a KSV CAM101 system from KSV Instruments. Briefly, a 3 µl droplet of DI water was deposited on three different samples for each of the surfaces prepared. The droplet contact angle was determined by measuring the angles between the baseline of the drop and the tangent of the same. In addition, atomic force microscopy (AFM) topography measurements of the surfaces were performed using an XE-100 Advanced Scanning Microscope from Park Systems under ambient conditions. Surface scans of 5µm x 5µm area were collected in tapping mode, and the overall RMS roughness (*Rq*) was calculated using the Park Systems XEI image analysis software.

3.3.2.2 Biocompatibility Assessment

Two immortalized neural cell lines obtained from American Type Culture Collection (ATCC, Manassas, VA) were used for this study: H4 human neuroglioma (ATCC # HTB-148) and PC12 Rat pheochromocytoma (ATCC # CRL-1721). The H4 cell line was cultured in advanced Dulbecco's Modified Eagle's Medium (DMEM) supplemented with 10% fetal bovine serum (FBS), 2.2 mM L-glutamine GlutaMAX-1, and 1% penicillin-streptomycin (PS). The PC12 line was grown in Kaighn's F-12K media supplemented with 10% FBS, 10% horse serum, and 1% PS. The media and sera were purchased from Invitrogen.

In order to perform the MTT assay and determine the cell proliferation on the substrates, each of the tested samples was placed into one well of a 12-well plate. Cell concentrations of $5x10^5$ cells/ml for both the H4 and PC12 cell lines were seeded in each well while adding 2 ml of cell media, followed by incubation at 37 °C for 96 hrs. in a 5% CO_2 and 95% relative humidity atmosphere. MTT assays were then performed in accordance with the procedures outlined in [78], with each assay repeated three times and in triplicate for each type of sample and for the polystyrene (PSt) control. The results were normalized with respect to the PSt control reading and statistical analysis was performed using ANOVA and the Tukey test, with an established statistical significance of $p < 0.05$. For the cell morphology and evaluation of filopodia and lamellipodia extensions, 12 well plates were also used, and $5x10^3$ cells/ml were seeded under the same environmental conditions. After 48 hrs., the samples were removed from the media and the cells were fixed using 4% paraformaldehyde and methanol. The AFM micrographs were taken in contact mode and the live cells were immersed in DPBS solution during the measurements. The AFM images were used to identify the filopodia and lamellipodia by relative height (~200-300 nm) and to assess spreading on the different surfaces.

3.3.2.3 SiC Substrate Characterization

The characterization of SAM-functionalized SiC substrates using X-ray photoelectron spectroscopy (XPS), ellipsometry, contact angle measurements, AFM topography, and Fourier transform infrared spectroscopy (FTIR) have been previously reported [169, 173, 176, 184]. We confirmed the characteristics of the functionalized SiC surfaces that are most pertinent to the current study (i.e. topography and wettability) prior to cell seeding. Static water contact angle (SWCA) measurements give an indication of the degree of hydrophobicity and hydrophilicity of the functionalized substrates. Table 2 contains the SWCA and RMS roughness values (reported as the statistical mean ± standard deviation of the mean) for the surfaces tested. We observed hydrophobic behavior for the 1-octadecene-treated sample, consistent with molecular methyl end-groups [173, 188].

Table 2 SAM characterization via AFM and water contact angle analysis.

Substrate	Surface Roughness, Rq[a] (nm RMS)	Contact angle [b](°)
6H-SiC untreated	0.30±0.1	19±2
6H-SiC with 1-octadecene	0.34±0.1	101±5
6H-SiC with APDEMS	0.36±0.1	48±4
6H-SiC with APTES	0.38±0.2	54±2

[a] Average surface roughness calculated from 5μm x 5μm scan areas averaged over 5 scans per surface.

[b] Contact angles measured with 3 μL water droplets and averaged over 3 different surface readings.

The APDEMS and APTES surfaces were moderately hydrophilic, with values in the expected range for amino end-groups [172, 176]. The untreated sample exhibited hydrophilic behavior, consistent with a native oxide. Surface topography analysis with AFM showed a very smooth surface following etching and prior to functionalization as seen in Figure 17a with a ~ 0.3 nm RMS value. The 1-octadecene-treated surface showed a similar topography to the pre-functionalized 6H-SiC surface with no aggregates (See Figure 17b). On the other hand, on the APDEMS and APTES-functionalized surfaces, some signs of oligomerization, most likely due to homogeneous methoxy cross-linking, were observed as particulates, and a difference of RMS roughness is obtained with respect to the 6H-SiC substrate (see Figure 17c and Figure 17d).

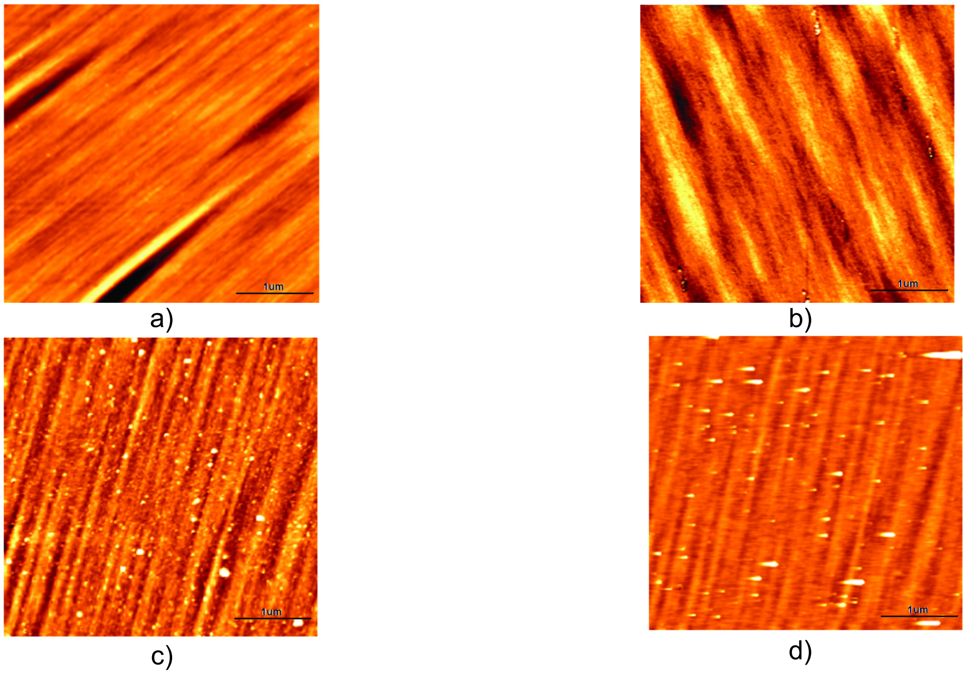

a) b) c) d)

Figure 17 AFM micrographs comparing the morphology of (a) 6H-SiC, (b) 1-octadecene functionalized 6H-SiC after alkylation, (c) APDEMS, and (d) APTES functionalized 6H-SiC after silanization. AFM data were recorded in non-contact mode with scan areas of 5 µm x 5µm and the scale bar range is 0 to 3.5 nm.

3.3.2.4 Cell Viability and Morphology

MTT assays were performed to quantify the cell viability on 6H-SiC (0001) substrates with and without the three SAMs described above. Although both cell lines exhibited qualitatively similar behavior, the PC12 cells showed a generally lower proliferation than the H4 cells. For the H4 cells, the Tukey test determined that the mean viability values of 0.44±0.03 and 0.76±0.07 relative to PSt obtained on the unmodified 6H-SiC substrates and on the 1-

octadecene functionalized surfaces were statistically similar. These results are in agreement with the lower permissiveness values determined through optical inspection of the cell morphology on these two surfaces. On the other hand, the APDEMS and the APTES treated surfaces showed dramatic increases in cell viability, exceeding the PSt control surface with mean viability values of 2.14±0.19 and 2.72±0.26 relative to PSt, respectively. These two values were statistically similar, as per the Tukey test, but different from octadecene modified and bare 6H-SiC. Of the two cell lines, the PC12 cells displayed the lowest proliferation on the bare 6H-SiC surface, with a mean viability of only 0.22±0.04 relative to PSt. A statistical difference of the bare 6H-SiC compared to the 1-octadecene functionalized surface was obtained with the Tukey test, with the octadecene-modified surface exhibiting a viability of 0.66±0.06 relative to PSt, an indication that the surface termination clearly affects this cell type. The APDEMS functionalized surface yielded a 1.26±0.09 proliferation with respect to PSt, whereas cell proliferation after functionalization with APTES was close to 1.86±0.15, much higher than the PSt control.

The average cell viability values obtained for the four surfaces tested were significantly different (*p-value* < 0.05) which is an indication that the response of the cells to the surface is indeed due to the material with which they are interacting and not to random factors involved in the experiment. More importantly, these results show a statistically significant degree of higher cell proliferation than previous studies performed with PC12 cells on porous Si [189] and SAMs on Si and glass substrates [172]. Figure 18 displays a summary of the cell viability obtained for both cell lines on each of the surfaces tested.

Insight into the cell morphology was obtained via AFM analysis. Figure 19 displays selected AFM micrographs of the H4 cell line for both the unmodified and SAM-modified surfaces, including a living cell and a fixed cell for each (3 cells were scanned per surface and a representative image was selected that best illustrates the cell morphology). Figure 20 shows the same for the PC12 cell line. Although some subtle differences in cell morphology exist, both cell lines exhibited certain trends on each type of surface.

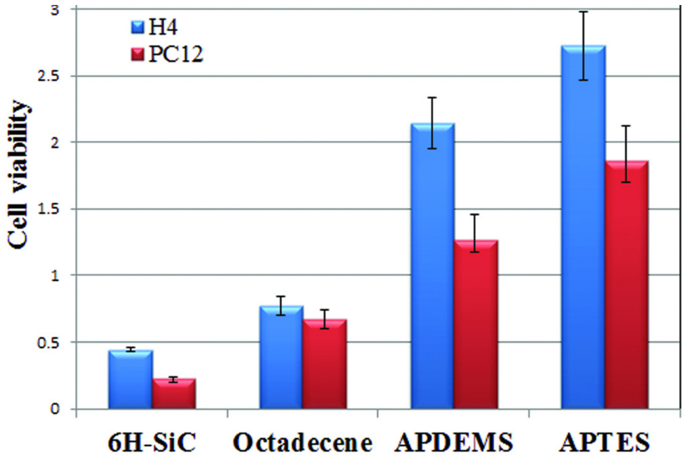

Figure 18 Proliferation of H4 and PC12 cell lines on the (0001) 6H-SiC substrates as a function of surface termination, as determined by MTT assay analysis. Results are normalized to the polystyrene control well and are expressed as the sample distribution of the mean $(\overline{x})$ and standard error of the mean (σ_M), normalized to the PSt readings.

For the bare 6H-SiC and 1-octadecene modified surfaces, AFM micrographs showed elongated or rounded cells with few focal points or filopodia and lamellipodia extensions. Indeed, the lamellipodia areas seen on those surfaces were not significant with respect to the total cellular areas (see Figure 19 and Figure 20). For both cell lines on the APDEMS and APTES treated surfaces, cells with elongated shapes that were flattened and expanded over larger surface areas were observed, suggesting good attachment and consistent with the high proliferation observed using MTT assays.

Additionally, there was evidence of focal point attachment, filopodia and lamellipodia extensions, as well as intercellular interaction. These results compliment the MTT assays, which showed greater proliferation on these surfaces compared to the untreated and 1-octadecene modified 6H-SiC surfaces.

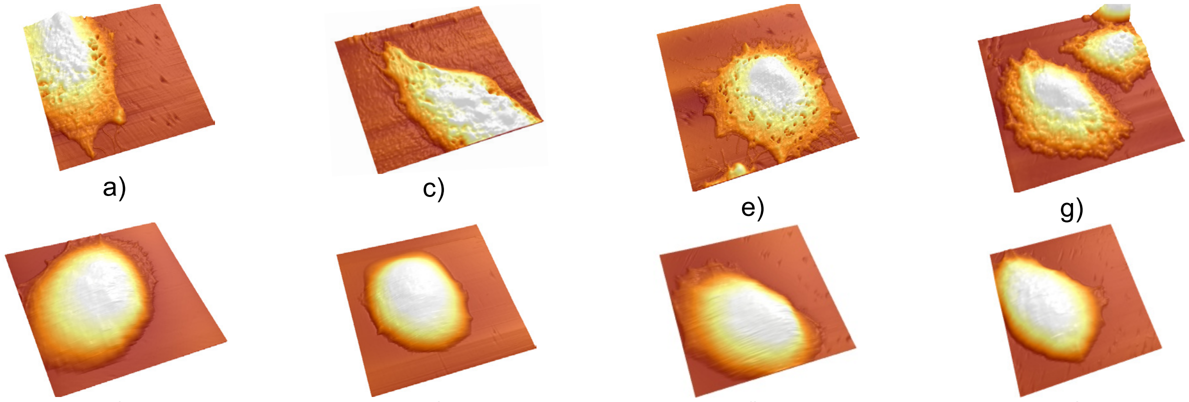

a) c) e) g)

b) d) f) h)

Figure 19 AFM micrographs for H4 cells, fixed (top row) and live (bottom row), on the untreated a) and b) and modified c) through h) 6H-SiC substrates. a) and b) are untreated 6H-SiC, c) and d) are 6H-SiC after alkoxyylation with 1-octadecene, e) and f) are 6H-SiC after silanization with APDEMS, and g) and h) are 6H-SiC after silanization with APTES. Scan size: 45µm x 45µm.

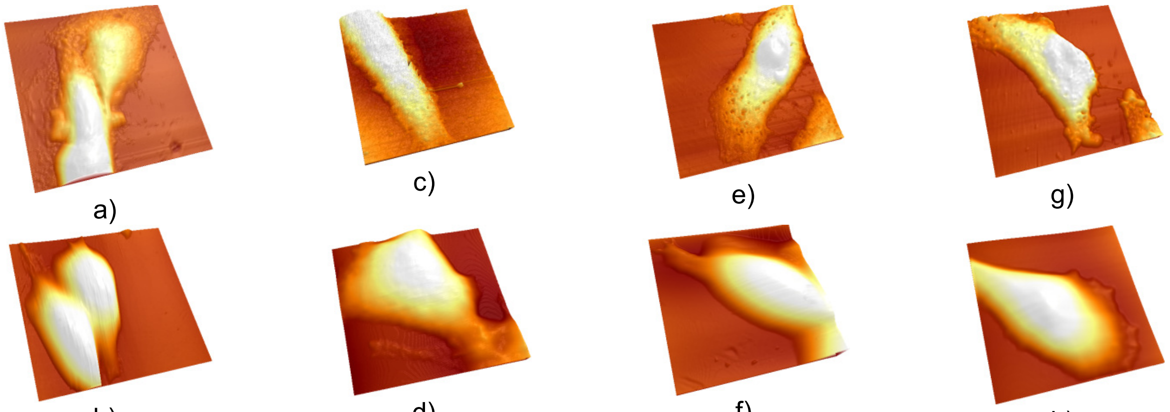

a) c) e) g)

b) d) f) h)

Figure 20 AFM micrographs for PC12 cells, fixed (top row) and live (bottom row), on the untreated a) and b) and modified c) through h) 6H-SiC substrates. a) and b) are untreated 6H-SiC, c) and d) are 6H-SiC after alkoxyylation with 1-octadecene, e) and f) are 6H-SiC after silanization with APDEMS, and g) and h) are 6H-SiC after silanization with with APTES. Scan size: 45µm x 45µm..

3.4 Surface Modification and Covalent Immobilization of Anti-Myoglobin on 3C-SiC

In this section we describe the surface modification of 3C-SiC (100) with 3-aminopropyltriethoxysilane (APTES) and the subsequent immobilization via covalent conjugation of anti-myoglobin on the modified surfaces, which are the critical initial steps for the fabrication of immunosensing based devices.

3.4.1 Preparation of 3C-SiC for Surface Modification

3C-SiC was grown in a horizontal, low pressure, CVD reactor on (100) silicon (Si) substrates at 1385°C [190]. The 3C-SiC samples were prepared by solvent cleaning, first in acetone then in isopropanol for 5 min each, followed by piranha cleaning (H_2SO_4:H_2O_2) (1:1) for 10 min and then immersed in HCl: H_2O (1:2) for 2 min to remove any residual sulfur and finally dipped in 5% aqueous hydrofluoric acid (HF) to remove any native oxide. Surface hydroxylation (-OH termination) was achieved with a final HF treatment done immediately prior to the functionalization reaction.

3.4.2 Surface Functionalization of 3C-SiC with APTES

Surface functionalization of 3C-SiC with APTES (Sigma-Aldrich) was done by immersion in a 1% APTES/toluene solution for 90 min. The samples were then rinsed by ultrasonication with toluene, toluene/isopropanol (1:1) and isopropanol for 20 min and 10 min for the last two steps. This was followed by a baking step at 100°C for 1 hr in an oven. Static water contact angle (SWCA) measurements were acquired using a KSV CAM 101 system in which 3 ml DI water droplets were deposited on the hydroxylated 3C-SiC and the APTES modified 3C-SiC surfaces. In addition, XPS was used (SPECS XR-50 Mg-Anodex-ray source, EKα = 1253:6 eV and photoelectron detection with a SPECS Phoibos 100 hemispherical analyzer and a MCD-5 detector) to measure the elemental composition and the chemical state of the elements on the SiC surface. The comparison of the survey and core level spectra of the hydroxylated SiC and the functionalized surfaces were used to confirm the successful formation of APTES layers on SiC. In addition, a XEI 100 scanning probe atomic force microscope (Park Systems) was used to analyze the surface topography before and after functionalization.

3.4.2.1 Characterization of the 3C-SiC|APTES Surface

SWCA measurements following surface cleaning and hydroxylation of the 3C-SiC substrates was found to be 16±3° and after APTES surface modification it was 62±1°, which shows an increase in surface hydrophobicity similar to the findings of Schoell *et al*. for 3C-SiC functionalization with aminopropyldiethoxymethylsilane [191],

Bierbaum *et al.* of aminopropyltrimethoxysilane on Si (111) [171] and Baur *et al.* of APTES on GaN and AlN [192]. AFM analysis of the surface topography of the 3C-SiC and chemically modified surfaces demonstrated that no surface aggregates or new features were produced, which is evident in the small change of the value of the surface roughness. For the bare surface the RMS roughness was ~0.9 nm and for the APTES-modified surfaces the RMS roughness value was 1.1 nm. These observations suggest formation of a smooth uniform organic layer (Figure 21a and Figure 21b).

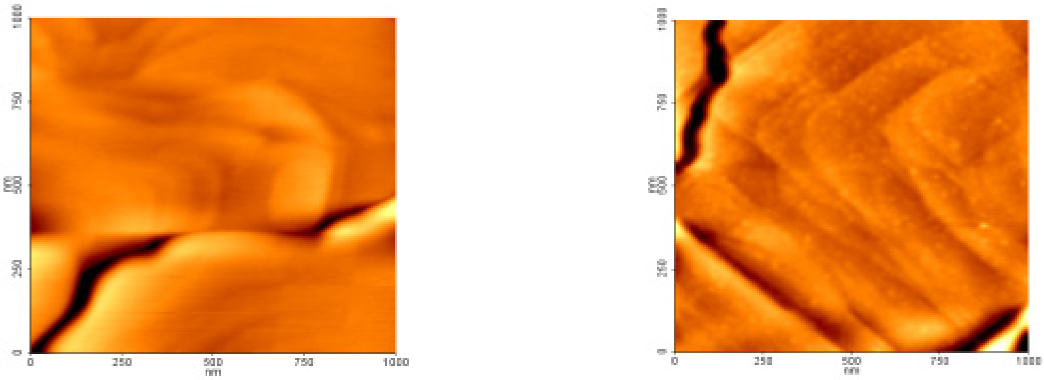

a) b)

Figure 21 AFM micrographs (1000 X 1000 nm^2, z scale 3 nm) of a) hydroxylated 3C-SiC b) Corresponding APTES modified surfaces. Images taken in non-contact mode.

XPS analysis revealed that the 3C-SiC was successfully modified by the identification of new carbonaceous and amino species on the modified surfaces. The deconvolution of the C-1s spectra resulted in two components, one at 283.5 eV that can be attributed to the C of the SiC substrate, and another one at 285.5 eV (Figure 22) due to the APTES-modified samples, which can be attributed to hydrocarbons at the surface. These peaks have also been identified by Schoell *et al.* and Rosso *et al.* in previous reports on 6H-SiC and 3C-SiC surface functionalization [173, 176, 191]. Following surface modification with APTES, an attenuation of the SiC substrate peaks for the C1s core level was observed, as seen in Figure 22a, due to the presence of overlying organic layers.

For the N-1s core level spectra, two components were resolved at 400.5 eV and 404.2 eV (Figure 22b), which arise from terminal -NH_2 and -NH_3^+ functional groups [171, 191]. This result demonstrates the effective formation of thin organic layers with a high concentration of reactive NH_2 groups that would allow for successful attachment of the anti-myoglobin on the surface.

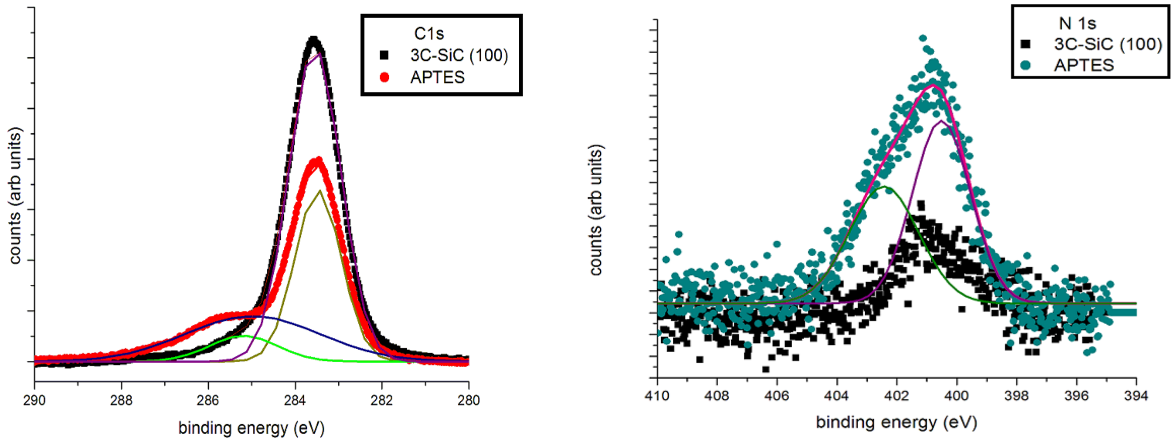

a) b)

Figure 22 a) C-1s core level spectra and b) N-1s core level spectra of the 3C-SiC after HF dip and APTES surface functionalization. The solid lines give the fitted spectral components of the deconvoluted data.

3.4.3 Anti-Myoglobin Immobilization on the 3C-SiC|APTES Surfaces

The immobilization of anti-myoglobin (Fitzgerald Industries) on the APTES modified SiC surface was performed via covalent conjugation at a concentration of 100 μg/ml. Covalent coupling was achieved by activating carboxylic acid groups of anti-myoglobin with 2 mM 1-ethyl-3-(3-dimethylaminopropyl)carbodiimide hydrochloride (EDC) (Proteochem^{TM}). Since EDC produces a reactive unstable intermediate, 5 mM *N*-hydroxy-sulfosuccinimide (Sulfo-NHS)

(Proteochem^{TM}) are also added in MES buffer (2-(*N*-morpholino)ethanesulfonic acid) at a pH of 5. The EDC, sulfo-NHS and antibodies are deposited directly on the APTES|SiC surface and incubated overnight at 4°C, this process is illustrated in Figure 23. After incubation of the antibodies, subsequent washes with PBS and 0.05% Tween 20 were performed followed by a blocking step consisting of washing with 1% Bovine Serum Albumin (BSA) in Phosphate Buffered Saline (PBS).

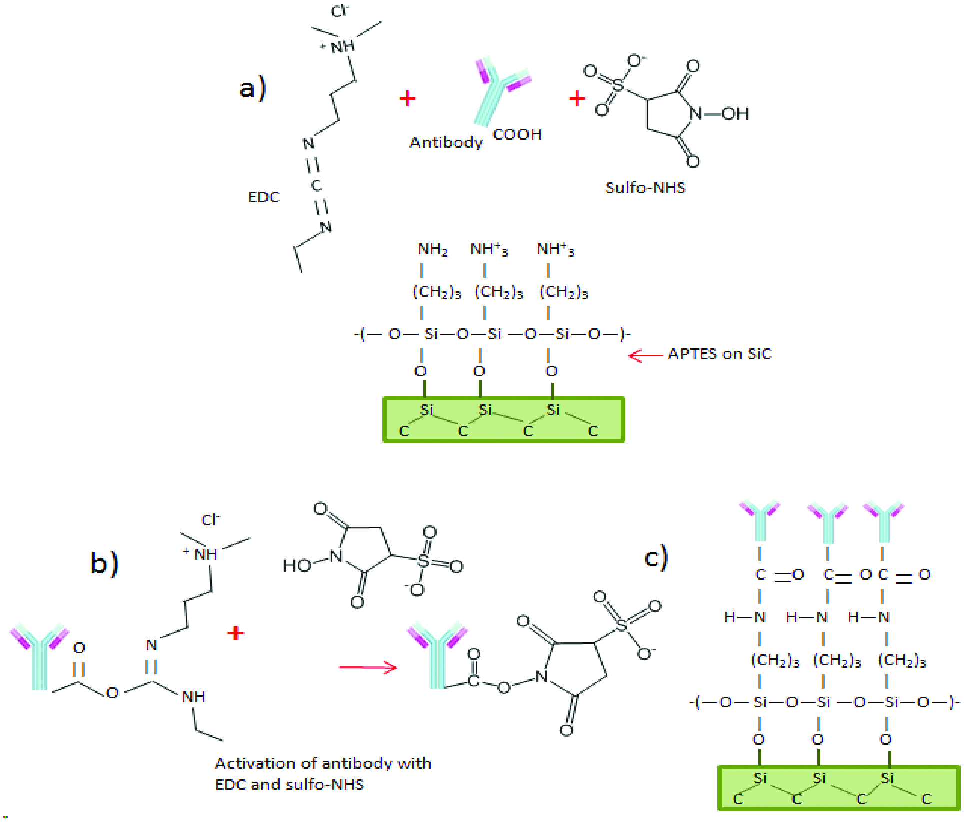

Figure 23 Process followed for anti-myoglobin immobilization. a) EDC-Sulfo NHS solution and anti-myoglobin are deposited on APTES|SiC samples, b) Activation of the antibody carboxylic group with EDC, sulfo-NHS produces a semi-stable amine-reactive ester and c) Antibodies coupled to the surface.

The surfaces used as controls for this experiment included, i) physical adsorption of the antibody on the surface, which was studied by omitting the EDC-Sulfo NHS covalent conjugation step, and ii) omission of the BSA blocking step. The former control reports differences between covalent and non-covalent immobilization of anti-myoglobin. The latter control investigated blocking by the adsorption of BSA as a means to prevent non-specific adsorption of Myoglobin. AFM was employed to monitor the surface topography after antibody immobilization and to check the uniformity of the surface. Likewise, fluorescent microscopy was used as a means to test the specificity of the Myoglobin to the anti-myoglobin immobilized on the 3C-SiC surfaces.

3.4.3.1 Evaluation of Anti-Myoglobin Immobilization On 3C-SiC|APTES Surfaces Via AFM

The qualitative evaluation of the anti-myoglobin immobilization was done with AFM. Three types of surfaces were evaluated: Surface A, covalent conjugation of anti-myoglobin to the surface followed by BSA blocking, Surface B, non-covalent linkage of anti-myoglobin to the surface followed by BSA blocking, and Surface C, with no BSA blocking step following the EDC/Sulfo-NHS covalent coupling of anti-myoglobin to the surface.

Surface A shows a uniform and densely packed antibody film with some isolated proteins. Some of the images present particles with a diameter ~20 nm while for others the length was close to 50 nm (Figure 24a). We also observed that the particles have a globular shape due to its protein nature, as was reported by several authors [193-195]. On the other hand, Surface B presents smaller particles packed in molecular arrays where the antibodies appear to adsorb in clusters. However, there are certain regions where no antibody adsorption occurred as seen in Figure 24b. This surface presents non-specific adsorption of anti-myoglobin because of the absence of covalent conjugation with EDC/Sulfo NHS. In addition, there are lower amounts of anti-Myoglobin on Surface B compared to Surfaces A and C. A blocking agent was used to fill up those gaps where covalent immobilization of anti-Myoglobin has not occurred and to prevent cross-reactivity and/or non-specific adsorption of other proteins.

For Surface C, where the BSA blocking step was omitted, similar images to Figure 24a were obtained; however, there were fewer clusters and less protein accumulation, which can be seen in some of the darker spots in Figure 24c. The larger aggregates on Surface A are likely due to the presence of BSA, a well know sticky protein, that readily adsorbs and forms aggregates. Surface C reflects the absence of the blocking protein, as the size of the particles have been reduced to an average of 30 nm. If the blocking step with BSA is omitted, the antibody immobilization process is not affected. However, it may impact the successful quantification of the antibody-antigen interaction because non-specific binding of the myoglobin (antigen) could possibly take place on the surface, which leads to poor results.

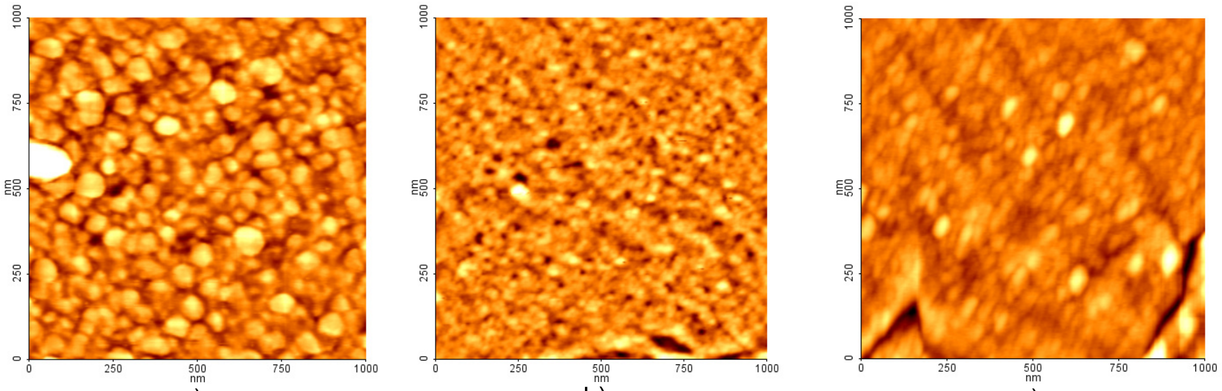

a) b) c)

Figure 24 AFM micrograph (1000 X 1000 nm^2, z scale 5 nm, non-contact mode) after myoglobin immobilization a) surface A (covalent immobilization and BSA blocking), b) surface B (non-covalent adsorption) and c) surface C (covalent immobilization and no BSA blocking).

3.4.3.2 Analysis of the Specificity of the 3C-SiC|Anti-Myoglobin Surface to Myoglobin

Specificity of an immunosensor to the antigen of interest is one of the main properties that can be accomplished with immunosensors, as was explained in Chapter 1. For this reason, after performing the characterization of the anti-myoglobin immobilized on the APTES modified 3C-SiC we used fluorescent microscopy to detect anti-myoglobin/myoglobin binding.

In this experiment we labeled myoglobin (Fitzgerald Industries) and hemoglobin (Sigma-Aldrich) with Alexa Fluor-488 (Life technologies) and incubated for 2 hrs. [196, 197] the anti-myoglobin immobilized on functionalized SiC surfaces. The idea being that when the myoglobin binds to the respective anti-myoglobin (Surface A*) it will produce a strong green luminescence signal. The hemoglobin was used as a negative control (Surface B*), since hemoglobin should not bind to anti-myoglobin functionalized surfaces. In addition, the incubation of the proteins directly on the SiC|APTES surfaces (Surface C*) is considered the second negative control.

The fluorescent intensity of the anti-myoglobin surfaces (Surface D*) was also measured as a negative control with lower values expected than on Surface A* because there is no presence of the labeled protein on the surfaces. As a positive control, anti-hemoglobin was immobilized on 3C-SiC|APTES surfaces and the labeled hemoglobin was used as the target proteins. In addition, myoglobin was incubated on anti-hemoglobin as the negative control. We refer to the respective surfaces in the positive control as Surface A** for SiC|APTES|anti-hemoglobin|BSA|hemoglobin, Surface B** for SiC|APTES|anti-hemoglobin|BSA|myoglobin, Surface C** for SiC|APTES|anti-hemoglobin|BSA| and Surface D** for SiC|APTES|BSA|hemoglobin.

In Figure 25 we present an illustration of the surfaces tested in this section and the steps followed to test the specificity of the SiC|APTES|anti-myoglobin surfaces to myoglobin. The protocol used for the anti-myoglobin (or anti-hemoglobin) was initially the one we described in Section 3.3.3. However, some modifications were made to this protocol because a strong signal due to non-specific binding of myoglobin was observed in Surface B** and of hemoglobin on Surface B*. For these reasons, the concentration of BSA as the blocking solution was increased to 3% with 0.25% of Tween 20 [198, 199]. It has been shown by other authors that the addition of Tween 20 to PBS helps to prevent non-specific adsorption of proteins on ELISA microtiter plates [199] and of IgG on silanized Si surfaces after adding it to fetal calf serum blocking solution [198].

The EDC-SulfoNHS protocol to crosslink the anti-myoglobin (or anti-hemoglobin) to the SiC|APTES surfaces was also modified to prevent hydrolysis that could cause regeneration of the carboxyl group in the antibodies after these are brought in contact with the 2 mM EDC-5mM SulfoNHS solution [200, 201]. After mixing the anti-myoglobin (or anti-hemoglobin) in EDC-SulfoNHS solution for 20 min we added 20 mM mercaptoethanol to quench the activation of the carboxyl group in the antibodies according to the steps followed in [202]. After the activated proteins reacted with the amino-terminated SiC|APTES surfaces, 10 mM hydroxylamine was added. This step hydrolyzes any un-reacted NHS that could interact with myoglobin that we are planning to detect [200, 201].

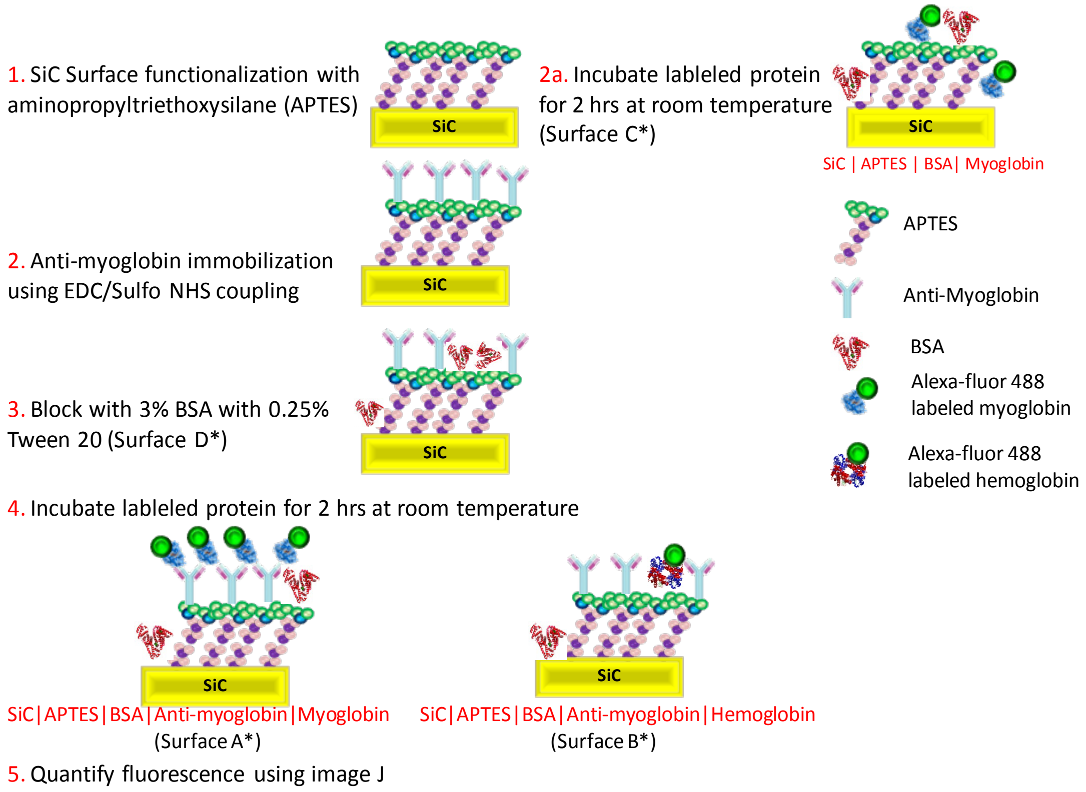

Figure 25 Illustration of the sequence followed to test the specificity of the SiC modified surfaces. The surfaces has been labeled from A* to E* to identify each of the treatments tested and the * to differentiate them from the surfaces tested in section 3.3.3.1.

To take the fluorescent images we used a Leica compound microscope with a CCD camera (SPOT5) and an exposure time of 5 sec. We took 5 images for each of the surfaces tested and the green intensity was quantified by calculating the integrated density of the images with ImageJ [8]. In order to process the data we subtracted the background (SiC substrate without surface modification) from surfaces A* to D*. In addition, for simplicity all of the results were normalized with respect to the average integrated density obtained on the surface where we expected the highest fluorescence to be generated (Surface A*) and are reported in Figure 26. The data is reported as the sample distribution of the mean $(\overline{x})$ (n= 9) and the standard error of the mean (σ_M). A t-test was performed for each surface with respect to their controls.

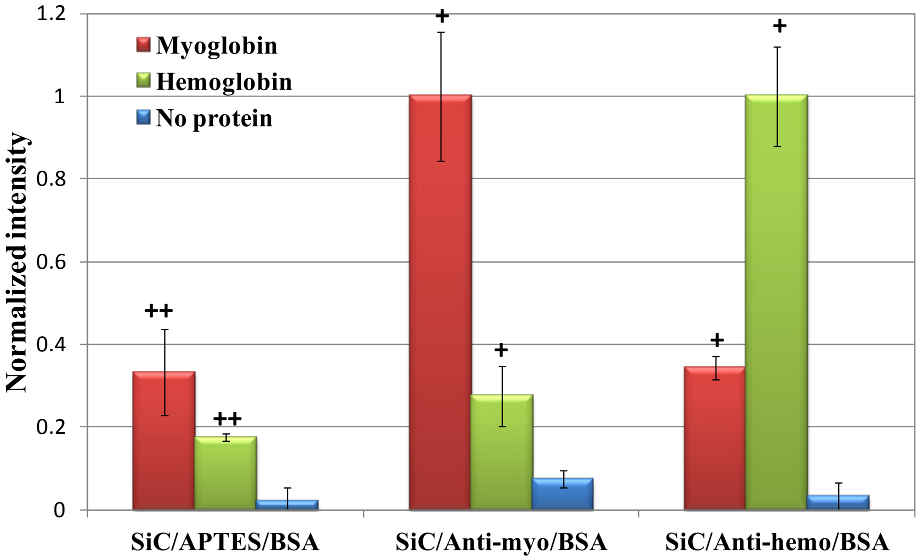

Figure 26 Normalized fluorescent intensity of Alexa-Fluor 488 labeled myoglobin and hemoglobin bound to APTES (left), anti-myoglobin (center) and anti-hemoglobin immobilized on SiC (right) with their respective controls. The results are expressed as the sample distribution of the mean $(\overline{x})$ and standard error of the mean (σ_M) and normalized to the positive control experiments in each test. $^{+}$ denotes p-values < 0.05 with respect to the antibody immobilized control and $^{++}$ denotes p-values < 0.05 with respect to the surface after APTES modification.

From the results presented in Figure 26 and Figure 27 we confirm the successful immobilization of anti-myoglobin on SiC and the specificity to the target protein, i.e. myoglobin. The fluorescent intensity levels on Surfaces A* and A** were higher compared to the control surfaces, with a higher fluorescent level on surface A** compared to A*. On the other hand, surfaces B* and B** did not show zero fluorescence and the degree of fluorescence was higher than surfaces D* and D** but comparable to surfaces C* and C**. This is an indication that a low degree of non-specific binding could occur on the surface but is not significant compared to surfaces A* and A**. In addition this may not affect the detection of the target protein. Lastly, surfaces D* and D** showed was very low fluorescence intensity (close to zero). The fact that D** is lower than D* could be due to the higher fluorescence intensity on A** than on A*, which influences the normalized results.

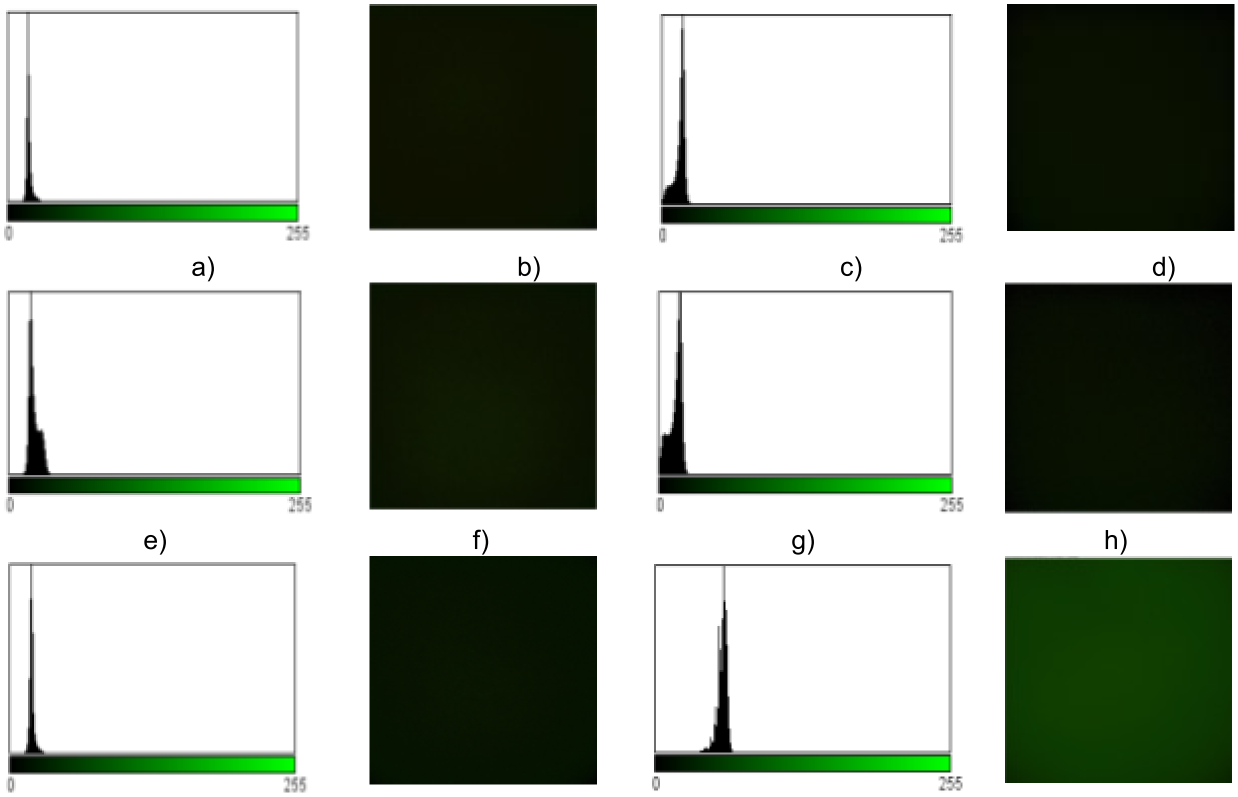

a) b) c) d)

e) f) g) h)

i) j) k) l)

Figure 27 Green signal extracted from fluorescent images before background subtraction for the tested surfaces. The fluorescent intensity is represented in the RGB histogram (green channel) and microscope image a) and b) non-treated SiC, c) and d) Surface C* (no protein), e) and f) Surface C*, g) and h) Surface D*, i) and j) Surface B*, and k) and l) Surface A*.

3.5 Summary

In this chapter we presented two different applications of self-assembled monolayers (SAMs) on SiC surfaces. The first one illustrated the process to tailor the SiC surface to study the effect of chemical termination in cellular attachment and proliferation. In section 3.1 we presented a brief overview of the different works regarding SAM formation and quality on SiC.

Then, in section 3.2 we studied the possibility of increasing cellular proliferation and attachment on 6H-SiC (0001) with PC12 and H4 cells using SAMs with terminal methyl and amino groups.

The results obtained from two *in-vitro* techniques, MTT assays and AFM cell morphology inspection, confirmed the characteristics of substrate viability and permissiveness, which were significantly better for the amino (NH_2)-terminated surfaces with an increase of ~5x and ~3x (APTES and APDEMS, respectively) for PC12 cells and ~8x and ~6x (APTES and APDEMS, respectively) for the H4 cell line with respect to the pre-treated 6H-SiC substrates.

This study indicates that the application of SAMs on 6H-SiC can greatly increase cell viability and substrate permissiveness while providing the ability to modify specific surface properties. This method allows for direct control of the wettability, surface chemical reactivity, and surface charge, which can directly impact the adsorption of ECM proteins that mediate cell adhesion and spreading.

The second application of SAMs on SiC (section 3.3), shows a way to produce a specific functionality to the surface to immobilize antibodies. This technique has been widely used for protein concentration detection in immunosensors. We were able to demonstrate that 3C-SiC (100) functionalization with APTES has successfully proven to be a starting point to link antibodies to the substrate. The fact that the APTES layer was uniform, as seen with AFM, and showed a change in surface wettability after chemical treatment of 3C-SiC, allowed the antibodies to attach to the functional moiety of the self-assembled monolayer. The use of covalent conjugation agents like EDC/Sulfo-NHS on Surface A compared to Surface B (where no EDC/Sulfo-NHS was used) yielded appreciable differences in the molecule conformation on the surface, i.e. homogeneous and uniform for Surface A while Surface B had areas where no proteins have been attached. We have also seen ovoid protrusions with diameters from 45 to 60 nm similar to the work done by Ehrhart *et al.* for hepatitis detection on polystyrene [19]. This could be due to the superimposition of two Y shaped immunoglobulins (IgG) that were randomly distributed on the surface. We would not expect the molecules to exhibit a Y shape because of the conformational flexibility of IGgs and interactions with the substrate.

On the other hand, in the experiment performed to test protein specificity we observed higher fluorescence values on sample A** compared to A*. The difference in the average fluorescence values was also compared using the t-test (p-value < 0.01). We could attribute this difference to possibly more uniform anti-hemoglobin (surface A**) layers that were formed on the SiC|APTES surfaces. The antibody immobilization performed via covalent heterobifunctional linkers produces random orientation and conformation of the antibodies on the target substrate as mentioned in section 1.3.1.2. Some degree of non-specific adsorption of myoglobin and hemoglobin was observed on surfaces C* and C**. Both surfaces presented fluorescence intensities higher than the SiC|APTES surface and it was not surprising that the values were similar to surfaces B* and B** in some specimens. The non-specific adsorption could be due to electrostatic binding of myoglobin and hemoglobin on areas of the samples where BSA has been displaced by the target molecule or regions where the APTES did not conform properly on the surfaces. For instance, Williams *et al* have found that BSA and streptavidin could non-specifically bind to APTES modified 4H-SiC, due to protonation of the APTES terminal group at a pH ~ 7.4 causing electrostatic binding of the proteins to the surface [203]. Other reasons for non-specific adsorption include the effect of surface roughness and defects in the formation of homogeneous self-assembled monolayers and non-immobilized bioreceptors as presented by Choi *et al*. This group has also shown that BSA can sometimes be displaced by other proteins or form a multilayer with proteins with opposite charges [204]. Even though we observed a similar behavior on our surfaces while looking for particular reasons for the non-specific adsorption on SiC, modified surfaces are outside of the scope of this work. Also because of the lower fluorescence intensity (2 times lower) on surfaces B* and B**, we concluded that the signal due to non-specific adsorption is not high enough to generate a false response when trying to target myoglobin. The results presented in this chapter suggest that SiC is a suitable substrate material for cell-based and immunosensing devices as was shown in sections 3.2 and 3.3.

CHAPTER 4: MYOGLOBIN DETECTON VIA IMPEDANCE SPECTROSCOPY ON 3C-SIC (100)

In Chapter 1 we described the concepts behind the construction of a SiC-based immunosensor. This includes the detection analyte, the antibody, the covalent immobilization of the antibody to solid surfaces, and the principal techniques employed to translate the antigen-antibody binding mechanism in terms of a measureable signal. Then, in Chapter 2 we discussed the properties and major works related to SiC biosensors, in addition to the physics behind the semiconductor|electrolyte interface that provides an understanding in the principles behind an immuno-electrochemical based device.

Before building a SiC CHEMFET to detect myocardial infarction we have decided to understand how each of the layers involved in the immunosensor construction affect the space charge region (SCR) of the semiconductor. For this reason, in this chapter we focus on the application of the concepts and protocols described in the previous chapters to study the changes in flat band potential and impedance in the SCR of 3C-SiC after formation of the APTES (i.e. the starting point for antibody immobilization), anti-myoglobin immobilization and afterwards, and the impact of adding different concentrations of myoglobin on top of the sensor surface. This last step is done with the purpose of identifying if we can detect levels of myoglobin similar to the those found in patients prone to AMI as well as healthy individuals using electrochemical means. However, due to the limited number of SiC samples available, we only tested one concentration of myoglobin (1 ug/ml), the same used in Chapter 3.

4.1 Electrochemical Cell Construction

4.1.1 3C-SiC (100) Working Electrode Fabrication

The 3C-SiC (100) films used in this work consist of a ~2 μm thick low-doped ($N_d \sim 10^{14}$ cm^{-3}) epitaxial film grown on a 4" Si (100) wafer as in [190] followed by a ~2 μm in-situ heavily-doped 3C-SiC film. In-situ doping is accomplished during the epitaxial growth phase by including 50 sccm of UHP N_2 into the precursor gas mixture in [190].

4.1.1.1 Characterization of In-Situ Doped 3C-SiC (100) Films

The surfaces of USF1-12-017 and USF1-12-018 were characterized by means of scanning AFM and electron microscopy (SEM), so that morphological information of the semiconductor surface could be correlated with device performance presented later on in this chapter.

Figure 28 shows topological data of the (100) SiC surface after AFM characterization of USF1-12-017. The AFM micrograph shows large flat mesas, called anti-phase domains (APD), with abrupt changes in height between the mesas, called anti-phase boundaries (APB). These are a characteristic topographical feature of 3C-SiC grown on (100) Si substrates. The height data shows many islands that are several tens of nanometers high with respect to the local surrounding film clustered along the APB and loosely scattered on the domains. Plan-view SEM micrographs of USF1-12-017 shows a surface morphology consisting of jagged, abrupt edge discontinuities of the phase boundaries separating the large mosaic-like regions of the anti-phase domains.

Close examination of the domain regions at magnifications >10 K (Figure 29b and 29d) reveals subtle square-shaped terraces resulting from the step-flow growth of the heteroepitaxial film.

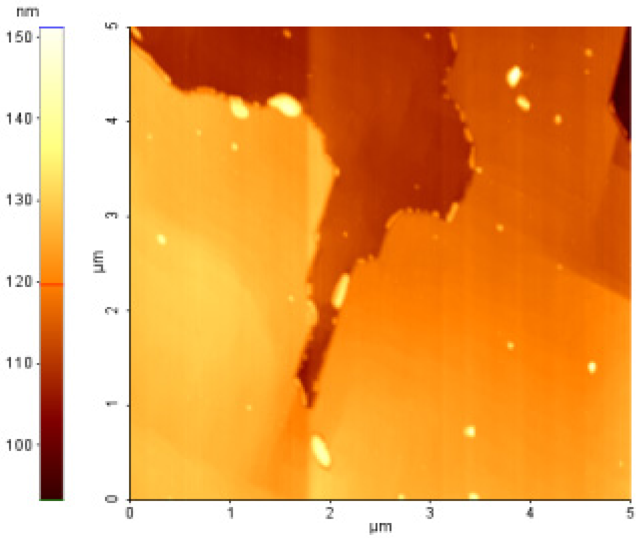

Figure 28 AFM micrograph of the in-situ doped SiC films (USF1-12-17) used for the electrochemical measurements. Rq = 7.2±3 nm and classic anti-phase domains are clearly evident, as expected.

The SEM images of USF1-12-017 show small dark areas covering the surface. It is interesting to note that the size of these features appear to be larger and more numerous along the APB edges, while smaller dark anomalies are evenly-distributed across the APDs along the step-edges of the terraces. Electron dispersion spectroscopy (EDS) analysis using an EDAX-Phoenix EDS system was performed on the anomalous features. The EDS spectrum of the dark areas indicated the anomalies were regions of carbon-rich silicon carbide. Analysis of the x-ray spectrum by percentage of the number of atoms detected for the carbon-rich SiC reveals 63.5% C and 36.5% Si, whereas the surrounding SiC demonstrated 49.5% C and 51% Si. A possible hypothesis for the presence of these features could be due to a carbon-rich precursor gas chemistry.

During the CVD growth process, the precursor gases decompose and adhere to the substrate surface as adatoms. These adatoms diffuse along the surface until they encounter an area of low energy, i.e. step edges on the film surface, and bind to the surrounding atoms. The slightly higher bond energy of the C-C bond (346 KJ/ mol) may favor the formation of C-C bonds over Si-C (318 KJ/ mol). Also, given that computational simulations have demonstrated that carbon adatoms experience a lower surface diffusion energy barrier than silicon adatoms on the

(100) SiC surface [205], the likelihood of carbon adatoms bonding to one another in a carbon-rich environment seems very plausible. Assuming the possibilities of the hypothesis, it would make sense to see large and numerous anomalies present at the APBs. These results also seem to suggest that any stoichiometric imbalances in the precursor gas composition that favor a carbon-rich chemistry do not produce films with the excess carbon evenly distributed within the film, but produce films consisting of localized areas of carbon-rich SiC embedded in a 1:1 stoichiometric SiC matrix.

The plan-view SEM images of USF1-12-018 also show the characteristic APB and APD features seen on USF1-12-017. However, the surface does not demonstrate the same character as the anomalies seen with the C-rich SiC film. The anomalies seen on the surface of USF1-12-018 are larger, more isolated and far less numerous than the features seen on USF1-12-017.

These features appear to protrude from the surface, much like a hillock or an inclusion. EDS analysis of the features show a very similar stoichiometric composition as the surrounding film.

In order to determine the approximate doping concentration of the 3C-SiC films, the wafers where RCA cleaned and CV (capacitance vs. voltage) measurements performed using a Hg probe (LEI 2017B, Lehighton Electronics Inc.). Figure 30a and Figure 30b show the Capacitance vs. applied potential (E) curve and the corresponding calculated doping concentration with respect to the depletion width. Using the equations (11) and (12) described in section 2.2 we obtained an average doping density for the in-situ doped 3C-SiC wafers of ~3.64 x 10^{18} cm^{-3}.

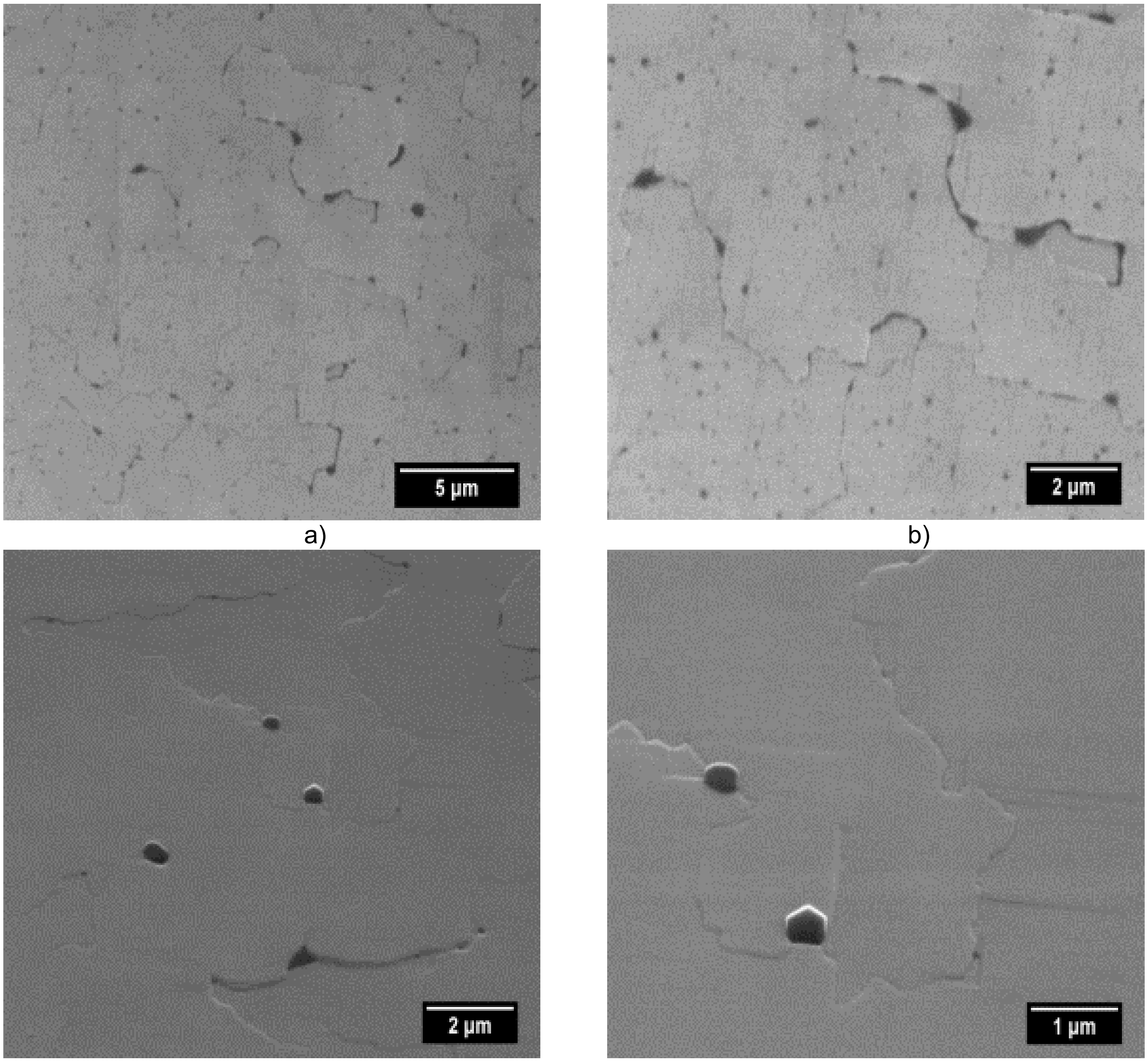

a) b)

c) d)

Figure 29 SEM images taken on the in-situ doped SiC films used for the electrochemical measurements. The first wafer (USF1-13-17) corresponds to a) 5K magnification and b) 10K magnification, the second wafer grown (USF1-13-18) corresponds to a) 10K magnification and b) 20K magnification. The surface contains cluster defects in addition to anti-phase domains. Cluster defects can act as surface recombination centers that will directly impact CHEMFET operation.

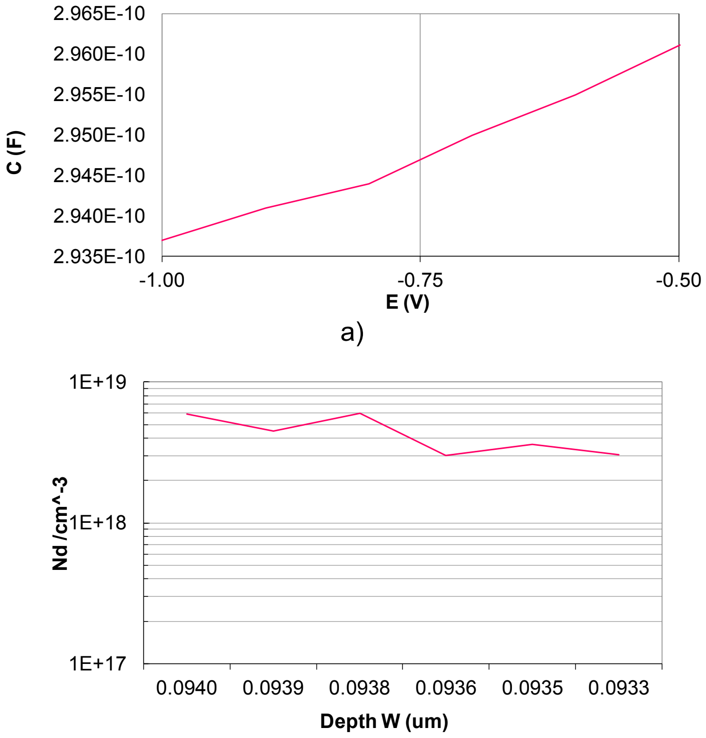

a)

b)

Figure 30 Characterization of the in-situ doped 3C-SiC wafers using Hg probe. a) CV measurements and b) calculated doping concentration (N_d). An acceptable level of doping (~3.64×10^{18} cm^{-3}) was achieved during growth which should be suitable for electrochemical measurements.

After confirming that the doping concentration was appropriate to make ohmic contacts to SiC, we proceeded to e-beam evaporate Ti/Ni (20 nm/150 nm) followed by Ti/Au (25 nm/150 nm) where the Au layer was deposited to prevent oxidation of the contacts. A schematic of the fabrication process of the SiC electrodes is shown in Figure 31. After contact formation, the contacts were annealed for 3 min (10 cycles of 20 sec each) at 1050°C in a rapid thermal annealer (Temp Teck Inc). Figure 32a shows the change in the inter-contact resistance before (9.8±3 Ω*cm^{-1}) and after (7.2±1 Ω*cm^{-1}) annealing the specimens while Figure 32b shows a picture of the contacts on the 3C-SiC sample. It is worth mentioning that two concentric electrodes were fabricated in order to reduce any reduce any edge effects on the electric field/current profile.

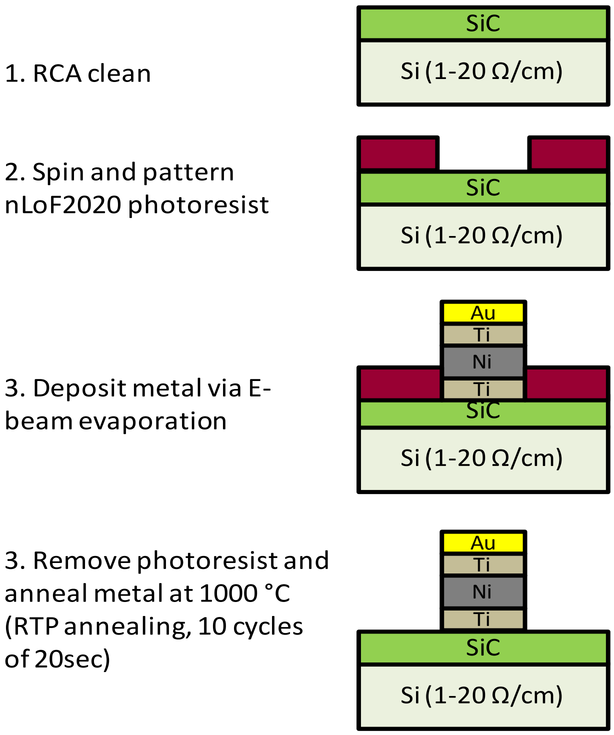

Figure 31 Process steps to fabricate ohmic contacts on in-situ doped 3C-SiC (100). The contact details are shown in Figure 32.

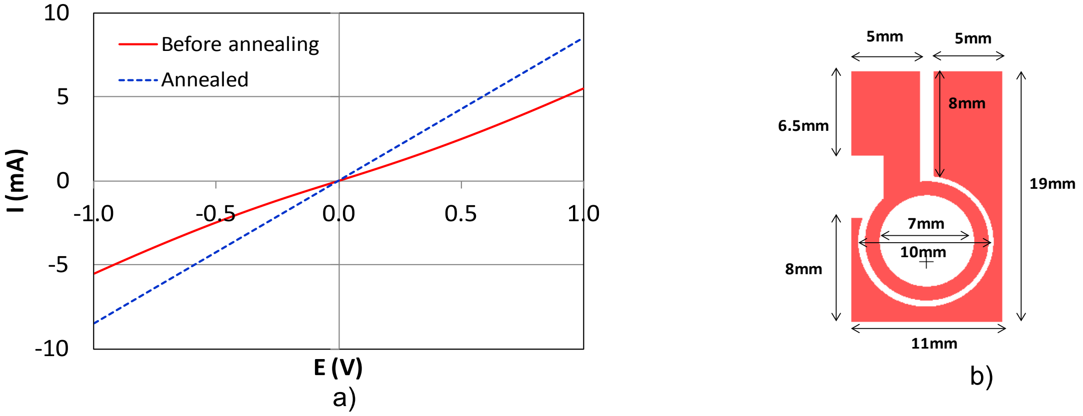

a) b)

Figure 32 a) Inter-contact resistance for ohmic contacts fabricated on in-situ doped 3C-SiC and b) pattern of the SiC electrode. Note: pink represents the metal. The contact resistance after annealing was ~ 7.2±1 Ω*cm^{-1}.

4.1.2 SiC Electrochemical Cell

In order to test the sensor an electrochemical cell was designed and constructed. The electrochemical cell consisted of an acrylic cover mount to hold the electrolyte, an o-ring (with an effective area of 0.13 cm^2) to create a seal when introducing the electrode in the cell, and a nylon base to which the cover mount was adjusted with two screws (see Figure 33a and Figure 33b).

The working electrode is the SiC specimen which consists of two concentric circular electrodes as described in the previous section. This shape was chosen to have a uniform current distribution across the SiC film when the current is applied from the potentiostat, as shown in Figure 33a. The inside electrode is the one where the current is applied and the outer one is where the voltage is probed with respect to the reference electrode. The reference electrode was a miniature Ag/AgCl electrode for the potentiodynamic tests and, for the Mott-Schottky and impedance spectroscopy tests, a Ti wire electrode with an outer mixed-metal-oxide surface was used as a low impedance reference electrode [58]. This later electrode was previously calibrated against the Ag/AgCl electrode. In all cases, the potentials have been converted to the saturated calomel electrode (SCE) scale for reporting purposes [8].

A Ti wire was used also as the counter electrode to provide a pathway for the current through the electrolyte. The four-electrode configuration was employed to avoid any voltage drop at the current insertion contact that could be caused by non-idealities of the ohmic contacts [206].

The electrochemical cell arrangement is presented in Figure 33a. We also show the equivalent capacitance and resistance in the same figure for reference. For simplicity, we have not included the double layer capacitance in this figure.

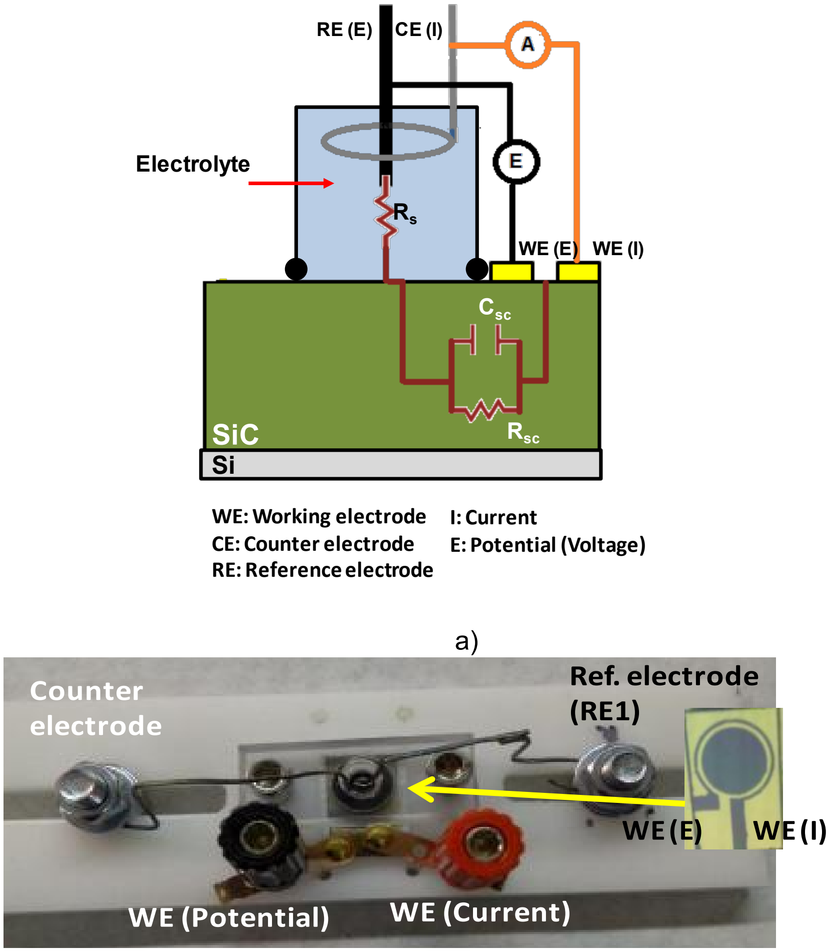

a)

b)

Figure 33 a) Diagram for the electrochemical cell used to study the SiC electrode before and after surface modification. Equivalent electrical parameters are shown to indicate their position with respect to the device and measurement apparatus. b) Picture of the SiC cell used in the laboratory. The WE (E) and WE(I) are circular electrodes as shown on the right.

4.2 Specimen Preparation and Testing Methodology

The SiC samples were solvent cleaned in an ultrasonic bath for 5 min in acetone and isopropanol and rinsed in DI water. The specimens were then immersed in diluted HF (1:100, HF: DI water) for 5 min to remove the native oxide and to obtain a hydroxyl (-OH) terminated surface. After cleaning the specimens and modifying the surfaces as described in section 3.3.3.2., three different tests were performed: 1) Impedance spectroscopy in the frequency range of 0.01Hz - 300kHz at 10 mV$_{rms}$. 2) Mott-Schottky plots were obtained from 1kHz and 10kHz with a voltage sweep of -0.6V to 0.6V (vs. SCE) with an amplitude of 10 mV$_{rms}$ and

50mV/s scan rate. This voltage range was chosen in order to avoid modifying the test due to H_2 evolution or O_2 reduction on the surfaces. 3) Cyclic polarization was performed in the same voltage range used for the Mott-Schottky experiments (5mV/s scan rate) to determine the open circuit potential (OCP) and the degree of passivation of the SiC electrodes before and after surface functionalization (including the antibody immobilization step). All the experiments were performed in Dr. Alberto Sagüés' laboratory in the dark at ~ 21 ± 2°C using a Gamry Reference 600 potentiostat. In all cases the electrolyte used was 0.1 M Phosphate buffer saline, PBS (KCl 2.68mM, KH_2PO_4 1.47 mM, NaCl 136.89 mM and Na_2HPO_4 8.10 mM).

4.3 Impedance Spectroscopy of the Functionalized 3C-SiC Surface

For the impedance spectroscopy, a total of seven specimens were tested. The idea was to perform these experiments to understand trends and identify the passivation of the surfaces after surface modification. This experiment was planned to test the same surfaces described in section 3.3.3.2. However, due to availability of the material the surfaces included in the impedance and Mott-Schottky experiments were surface A* (i.e. myoglobin bound to anti-myoglobin modified surfaces), surface B* (i.e. hemoglobin bound to anti-myoglobin modified surfaces) and surface C* (i.e. myoglobin immobilized on SiC|APTES surfaces) described in the mentioned section. The purpose of using surfaces B* and C* was to have two different controls that would allow us to identify if there are changes, or not, in impedance and flat band potential in the cases where the target protein myoglobin should bind to the anti-myoglobin modified SiC.

The impedance spectra (as well as Mott-Schottky) were collected after each step of the preparation of the surfaces. That means that for surface A* we did an impedance test after hydroxylation of SiC, after APTES functionalization, after anti-myoglobin functionalization and finally after myoglobin incubation. In the following section we will discuss the results for each of the mentioned surfaces.

4.3.1 Analysis of Impedance Spectroscopy Results for Surface C*

The first control surface tested was surface C*. The Nyquist plot obtained for two of the three specimens tested is presented in Figure 34. The results for the third specimen are not presented due to the similarity to the ones obtained for sample 17R shown in Figure 34b. By looking at the Nyquist plots we could say that 18F shows an indication of passivation due to the APTES layer compared to specimen 17R because the increase in the amplitude of the semicircular plot. Likewise on Figure 34a we see that after the incubation of myoglobin there is no increase in impedance whereas we see the opposite in Figure 34b. This could be an indication of some binding of the myoglobin to a defective APTES film.

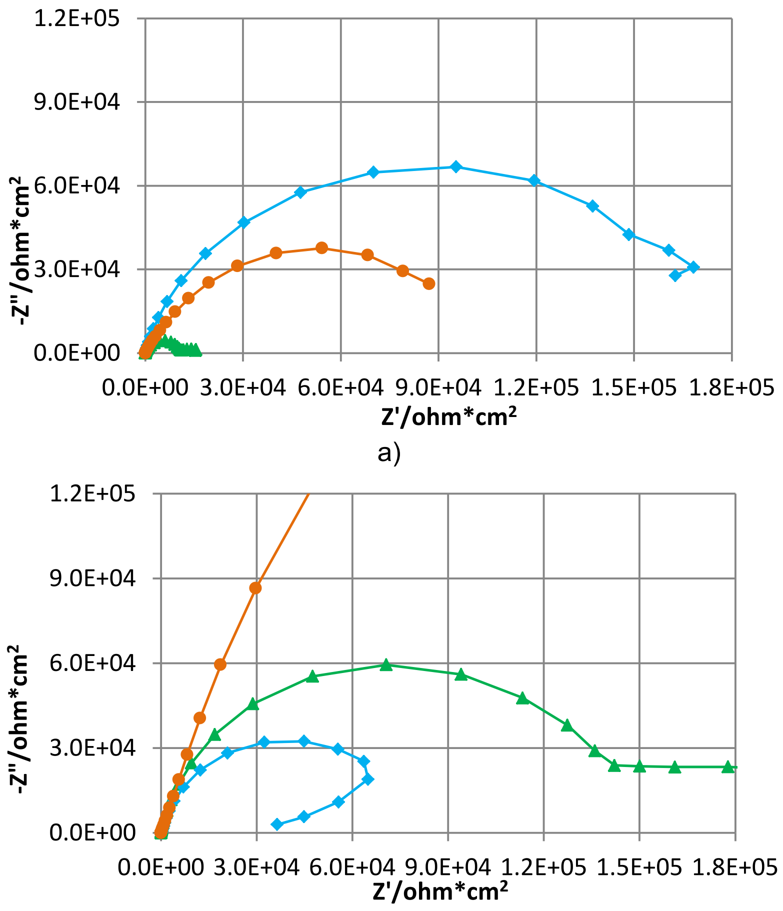

a)

b)

Figure 34 Nyquist plots obtained for each layer needed to form surface C* on specimen a) 18F obtained from wafer USF1-13-18 and b) 17R from wafer USF1-13-17. ▲ Bare SiC ◆ APTES, ● Myoglobin.

The Bode plots shown in Figure 35 show evidence of the non-idealities in the impedance magnitude for both specimens prior to the functionalization, especially at lower frequencies. The lower frequencies (f< 1Hz) typically represent the behavior of the double layer capacitance [207]. As can be seen from the insets of Figure 35b and Figure 35d, at higher frequencies (> 100 kHz) the curves do not fully converge to the same impedance value due to differences in the solution resistance. This behavior may be due to variations in the position of the reference electrode when the samples are withdrawn and reintroduced in the electrochemical cell after performing surface modification steps. In addition, we see that for specimen 17R the magnitude of impedance is almost the same as that for the bare SiC surface after APTES functionalization but decreases for frequencies < 1kHz. It could be that the APTES layer formation on this sample did not result in a homogeneous layer. For sample 17R, the myoglobin incubation step seems to result in the highest impedance from the Nyquist plots, higher than the curve obtained for the APTES modified surface. In the Bode plots (see Figure 35) the impedance appears to be higher at lower frequencies (< 1Hz) but lower than APTES at higher frequencies. For 18F, the impedance presents a different behavior than on 17R, with a small increase after APTES functionalization, mostly at < 1Hz and then decreases after myoglobin incubation on the samples for all the frequency range tested.

4.3.2 Analysis of Impedance Spectroscopy Results for Surface B*

For surface B*, the one in which anti-myoglobin immobilization has been performed and hemoglobin is incubated to test for non-specific binding, three samples were also tested. However we noted metal residue (maybe from the liftoff step) on one of the samples and it was therefore not included in the analysis. From Figure 36 we identify similar trends on both specimens but the impedance tends to be higher on 17Q for the Bare SiC and APTES treated surface compare to 17P. There is an indication of an increase in the real and imaginary components from the starting hydroxylated SiC surface to the anti-myoglobin surface. We observed no or very small binding of hemoglobin because no significant change in impedance was observed after this step.

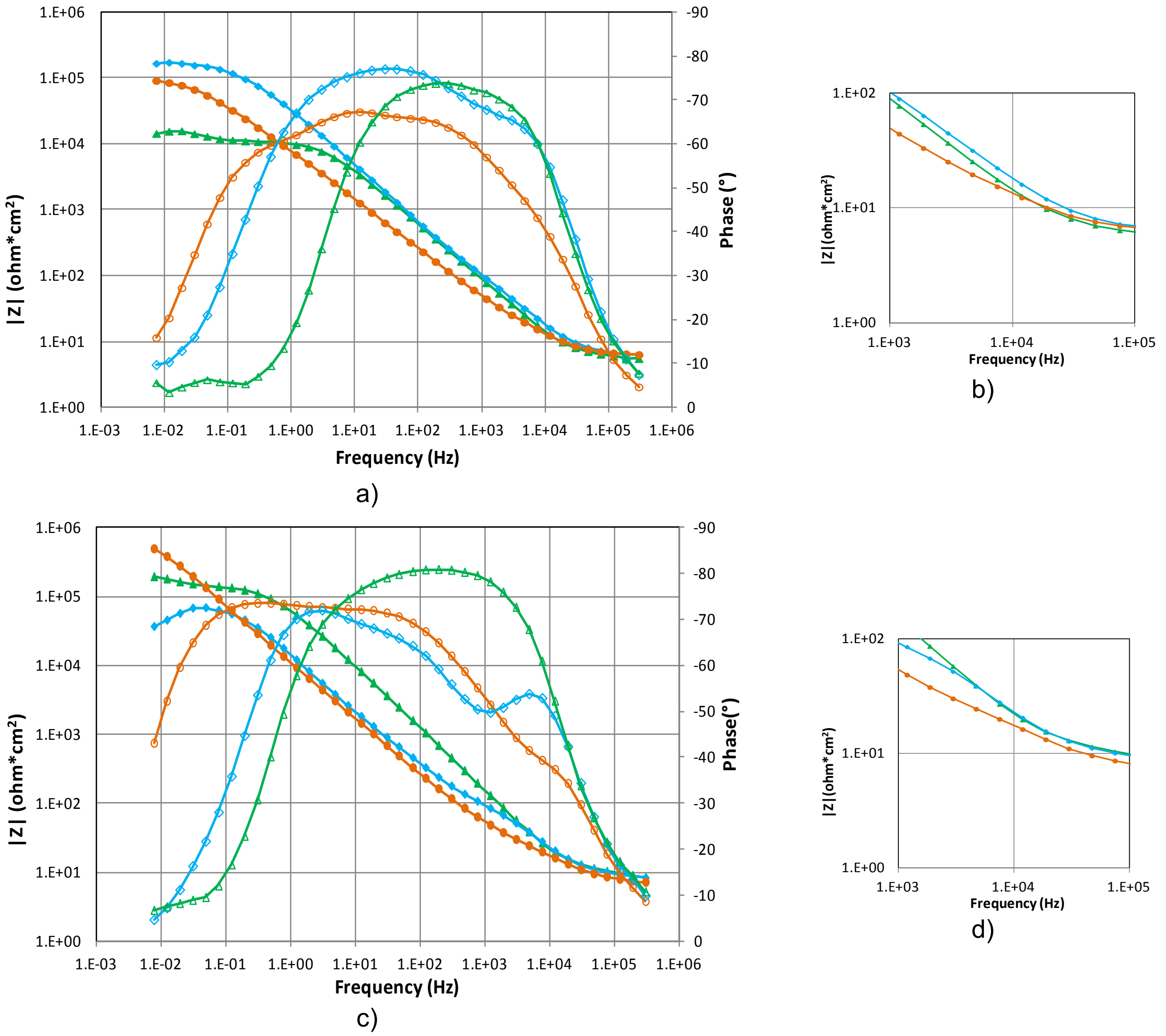

a) b) c) d)

Figure 35 Bode plot on SiC, after APTES and after myoglobin incubation (surface C*) on specimen a) 18F obtained from wafer USF1-13-18 b) inset for the |Z| at high frequencies for 18F c) 17R from wafer USF1-13-17 and d) inset for the |Z| at high frequencies for 17R. ▲ |Z| Bare SiC ◆ |Z| APTES, ● |Z| Myoglobin. The open symbols represent the phase.

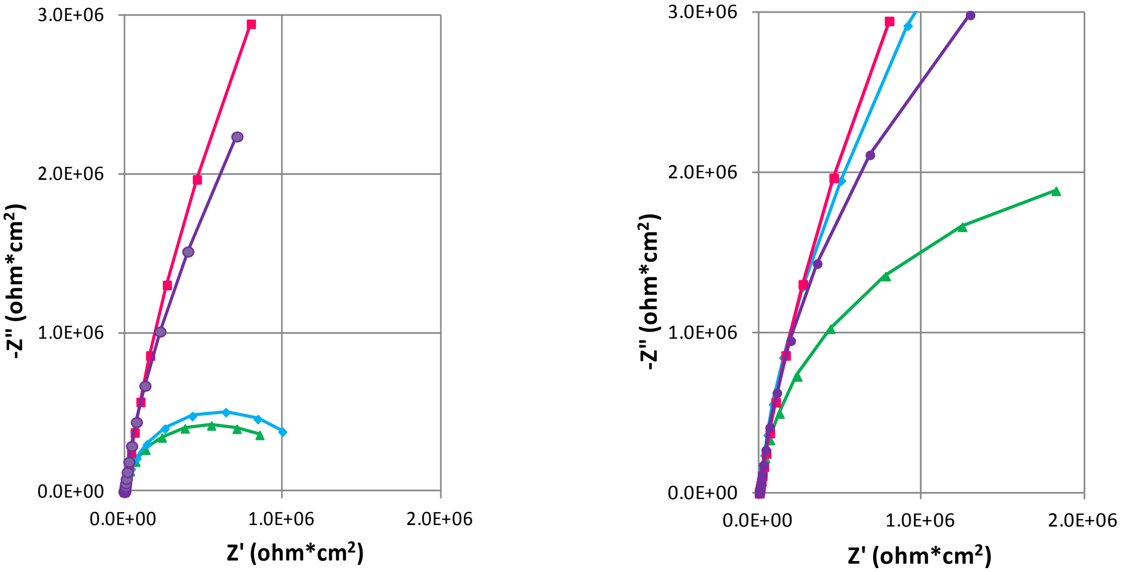

a) b)

Figure 36 Nyquist plots obtained for each layer needed to form surface B* on specimen a) 17P and b) 17Q both from wafer USF1-13-17. —▲— Bare SiC —◆— APTES, —■— Anti-Myoglobin —■— Hemoglobin.

The Bode plots for surface B* are shown in Figure 37. The inset shown in Figure 37b and Figure 37d illustrates a similar tendency for the impedance magnitude on both specimens. However, we have to be careful when judging the results because of the variability in the solution resistance. Similar to what we observed in Figure 35a for specimen 18F, there is an increase in impedance after APTES functionalization suggesting passivation of the surfaces due to increased impedance with respect to the surfaces with no treatment (Bare SiC). This effect is increased after the anti-myoglobin linking step in the Nyquist plot presented in Figure 36, but it shows a decrease in impedance. For specimen 17P, the impedance is higher after anti-myoglobin immobilization at f < 1Hz, but is lower at all frequencies for 17Q (see Figure 37).

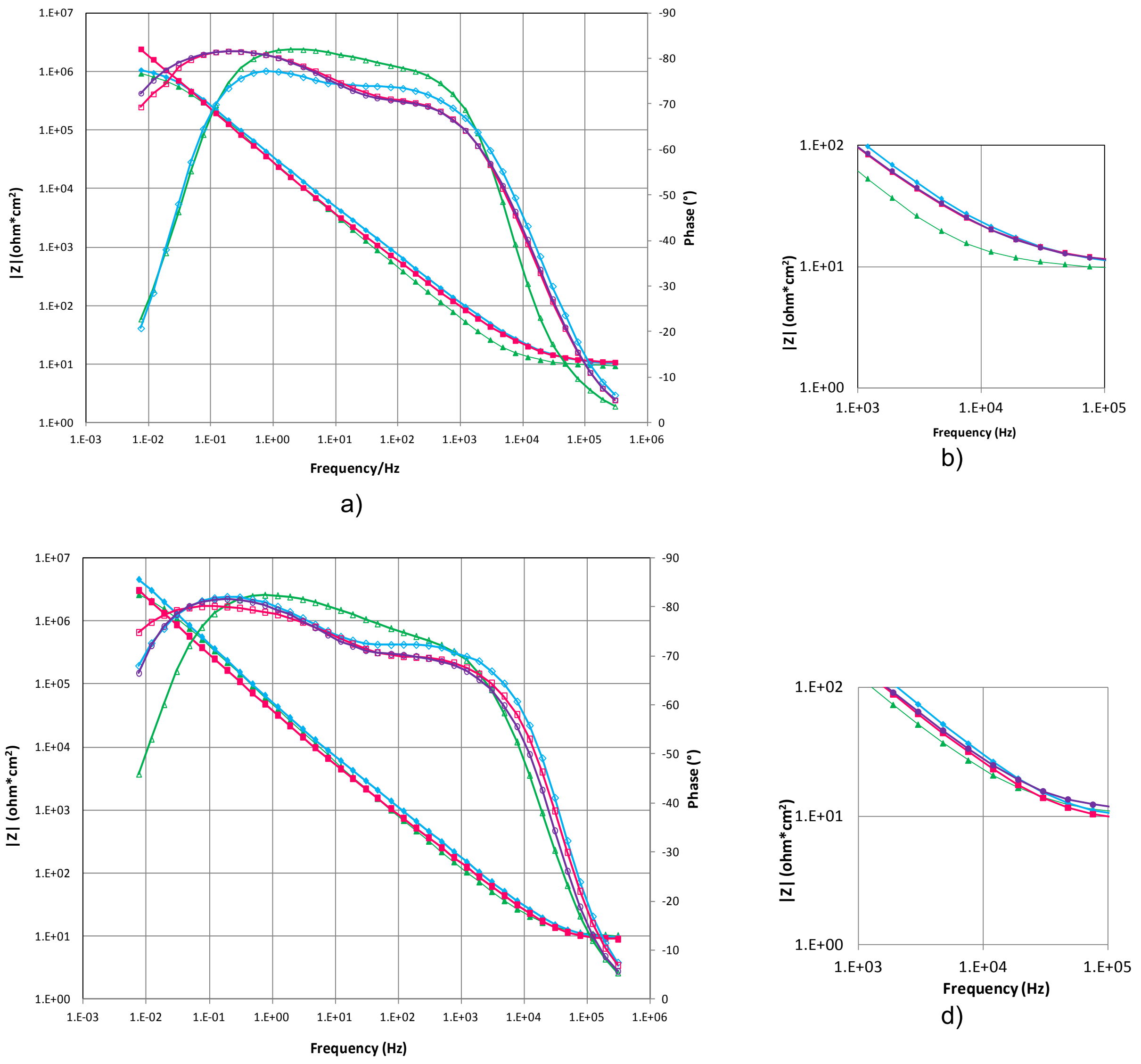

a)

b)

c)

d)

Figure 37 Bode plot of each layer that forms surface B* on specimen a) 17P b) inset for the |Z| at high frequencies for 17P c) 17Q and d) inset for the |Z| at high frequencies for 17Q. Both specimens were obtained from wafer USF1-13-17. ▲ |Z| Bare SiC ◆ |Z| APTES, ■ |Z| Anti-Myoglobin ■ |Z| Hemoglobin. The open symbols represent the phase.

4.3.3 Analysis of Impedance Spectroscopy Results for Surface A*

The last surface that we tested was surface A*, our target protein, myoglobin, immobilized on anti-myoglobin linked to SiC. In this case one out of three specimens showed evidence on myoglobin immobilization on the surfaces. From the Nyquist plots we observed an increase in the real and imaginary components of the impedance after APTES functionalization and anti-myoglobin linking to the surfaces. The situation was different after the myoglobin incubation, where we saw this behavior for only one specimen. However, for this specimen we also saw a different behavior in the impedance magnitude after linking the anti-myoglobin to the APTES surfaces as can be seen in Figure 39a and Figure 39b. Since the values observed for the impedance in the Nyquist plots were similar for both specimens 17C and 18C but different in the bode plots we considered that another effect besides the surface treatment may be responsible for these unexpected results. Different apparent capacitances due to different effective areas when taking one measurement after APTES or anti-myoglobin can cause deviations in the expected response. This could produce erroneous values of the magnitude of the impedance in combination with the variations in the position of the reference electrode.

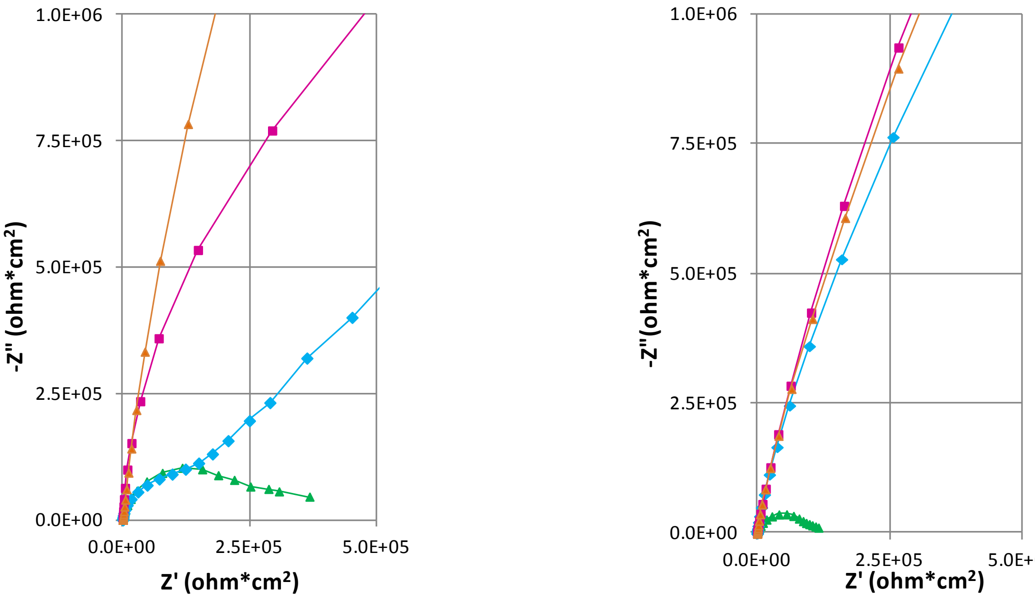

a) b)

Figure 38 Nyquist plots obtained for each layer needed to form surface A* on specimen a) 17C obtained from wafer USF1-13-17 and b) 18C from wafer USF1-13-18. ▲ Bare SiC ◆ APTES, ■ Anti-Myoglobin ● Myoglobin.

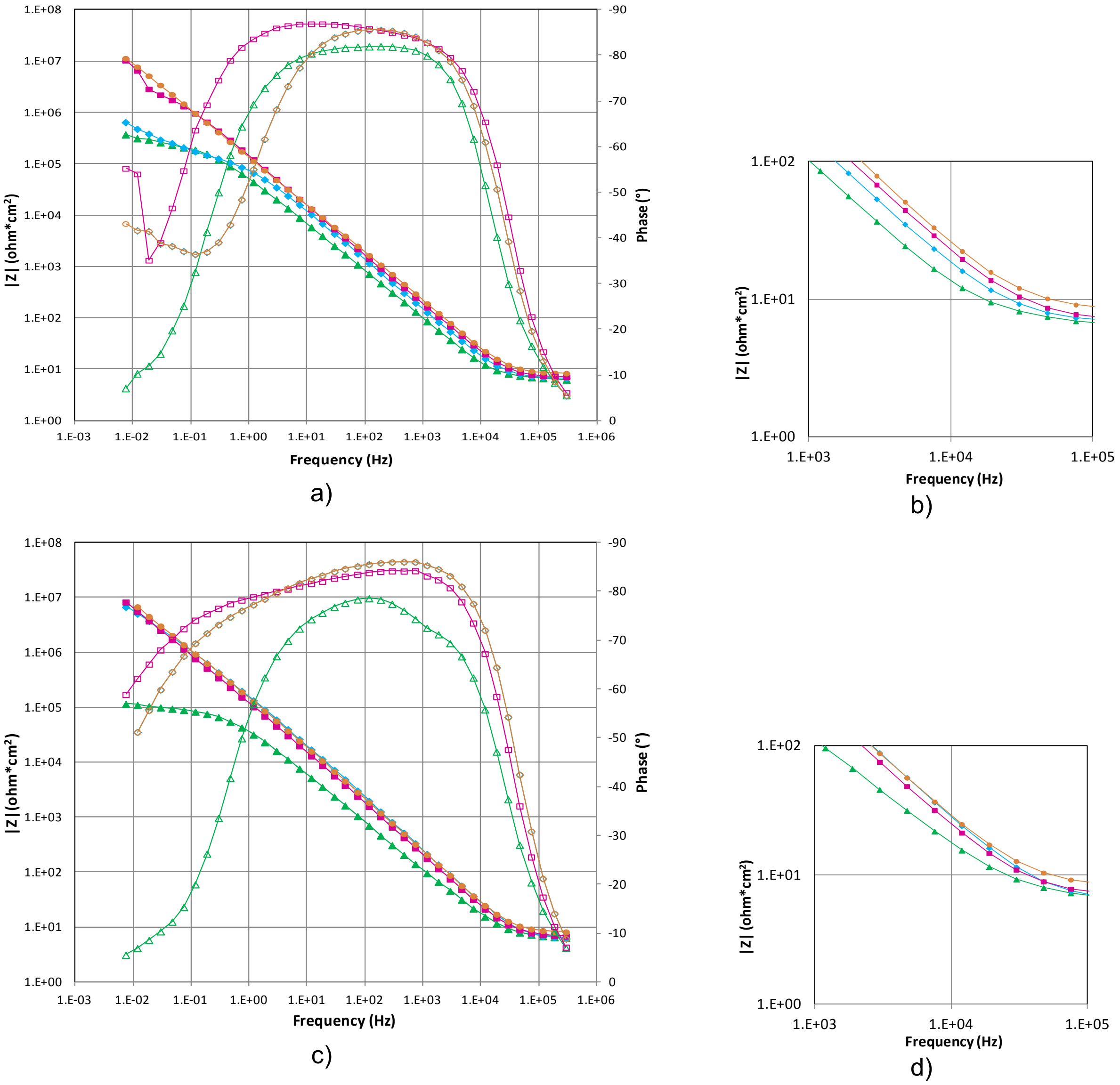

a)

b)

c)

d)

Figure 39 Bode plots obtained for each layer that forms surface A* on specimen a) 17C obtained from wafer USF1-13-17 b) inset for the |Z| at high frequencies for 17C c) 18C from wafer USF1-13-18 and d) inset for the |Z| at high frequencies for 18C. ▲ |Z| Bare SiC ◆ |Z| APTES, ■ |Z| Anti-Myoglobin ● |Z| Myoglobin. The open symbols represent the phase.

4.4 Equivalent Circuit Used to Fit the Impedance Spectroscopy Results

As was explained in section 1.4.1, Nyquist and Bode plots can be associated with an equivalent circuit of resistors and capacitors. Fitting our data to an equivalent model will provide more information regarding the quality of the films and the changes in the SCR after the surface modification. In Figure 40 the equivalent model used in this work is presented. It includes two constant phase elements (CPEs) to include the non-linearity observed in bode plots. Because of the surface roughness and the irregular structure of the coatings, in this case APTES and antibodies, a CPE is used to describe this kind of systems appropriately, just as we described in section 1.4.1.

The first CPE reflects the changes in the double layer capacitance (C_{dl}) that dominates the frequency range 0.1Hz -1Hz. After surface modification, the double layer capacitance is considered to be in series with the layer obtained after modification, as shown in Figure 40b. After performing the model fitting the value of n obtained for this CPE was between 0.8 to 1.0, which is close to an ideal behavior, except for specimens 17R, 18H and 18F that presented the less ideal behavior with $0.6 < n < 0.9$. The second CPE corresponds to the SiC SCR (C_{sc}) that dominates the frequency range 1 kHz -10 kHz. After fitting the data to the model the value of n for this CPE was between 0.8 to 1.0, which is close to ideal behavior, except for specimens 17P and 17Q that presented a less ideal behavior of $0.6 < n < 0.9$.

The model also includes the solution resistance (R_s), the charge transfer resistance (R_{ct}) that is related to the passivation of the films, and the resistance associated with the SCR (R_{sc}) in the SiC.

The variations of each of the parameters that conform to the equivalent circuit are presented in Figure 42 and Figure 43. In addition, the percentage change is included in Tables 3, 4 and 5. Because of the variability in the results, we decided not to average the values obtained for each sample used to test surfaces A*, B* and C*. This could provide a better way to understand the expected behavior when the target surfaces (and the controls) are tested.

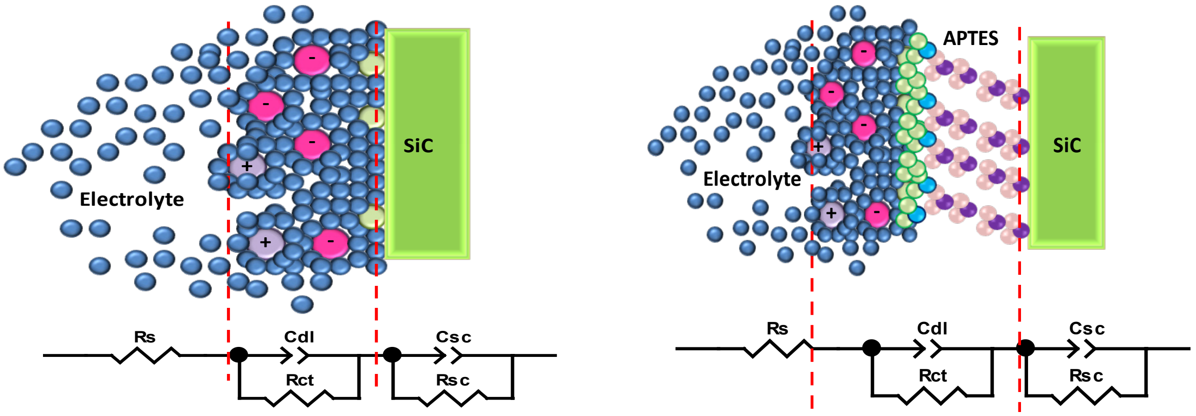

Figure 40 Equivalent circuit used to perform the fitting of the impedance spectra obtained for surfaces A*, B* and C*. Left model for bare SiC. and right model for functionalized SiC.

4.4.1 Model Fitting for Surface C*

In general R_{ct} increased after the APTES functionalization, except for samples 18H and 17R where the value decreased. This indicates less passivation of the APTES film on these two specimens. Likewise, APTES is known to form in islands which could cause that part of the SiC is exposed to the electrolyte leading to subsequent myoglobin binding directly to the SiC surface. This can be concluded from the higher R_{ct} and the decrease in C_{dl} after myoglobin immobilization for samples 17R and 18H in Table 3.

The increase in C_{sc} after APTES modification can be due to protonation of the monolayer from an NH_2 to NH_3^+ end group. Both terminations are typically obtained on the surface after modification of SiC [191]. A positive net charge on the semiconductor surface will cause a decrease in the depletion layer width and, hence, an increase in C_{sc}. It is still not clear why the value for R_{sc} increases for sample 18F contrary to what is expected due to a lower depletion width, and is seen in sample 17R.

4.4.2 Model Fitting for Surface B*

For the other specimens used to test surfaces B* and A*, similar trends in R_{ct} and C_{dl} were seen, which gives an indication of the degree of APTES layer passivation. However, the rest of the parameters do not present the percentage increase that was expected for all the specimens. In the case of specimens 17P and 17Q (surface B* test) the R_{ct} after anti-myoglobin immobilization was reduced. One could think that the cross-linking of the anti-myoglobin surfaces did not result in a uniform film. From Figure 37, the change in the impedance magnitude is small which can be misinterpreted when fitting the model or perhaps a different model should be used to fit the data. However, C_{sc} shows an increase that could indicate the presence of the positive charges due to the antibodies. It could also be an increase in protonated end-groups of the APTES films that could prevent the anti-myoglobin from linking to the surface. The final treatment that included the hemoglobin immobilization showed very small changes in R_{ct} for sample 17P but much higher increase on sample 17Q, which could suggest NSB on the later sample. These results were not completely clear because the analysis of C_{sc} gives an indication of very little changes in the depletion width in the semiconductor.

4.4.3 Model Fitting for Surface A*

Similar trends with respect to the samples used to test surface B* were identified for specimens 17C, 18B and 18C that were used surface A*. Even though some inconsistencies where seen for C_{dl}, R_{sc} and C_{sc}, one can see that for sample 17C the increase in R_{ct} and increase in C_{dl}, together with an increase in C_{sc} after myoglobin immobilization, provides an indication of the detection of the protein on this specimen.

On the other hand, on 18C after the myoglobin immobilization step we did not see significant changes in R_{ct}, C_{dl} in addition to a very small increase in C_{sc} that confirms that no protein was detected on this sample.

The net charge of the APTES, the antibodies and the later protein binding affect the band bending of the semiconductor, as mentioned in chapter 2. From the model fitting some conclusions were drawn and, in other to give the reader a more clear explanation, we provide an illustration of changes in the SCR of the semiconductor for a particular charge present at the semiconductor-electrolyte interface. Both the APTES and antibodies present a positive net charge [208, 209], whereas myoglobin and hemoglobin tend to be negatively charged in buffers with pH above their isoelectric point (pI). The pI for myoglobin is 7.2 and for hemoglobin is 6.5 [210, 211]. However, the conformation of the protein could change once bound to the surface and also the amino acids that are exposed and that determine its net charge. When the n-type semiconductor, SiC in this case, is in depletion (see chapter 2) and brought in contact with positive charges the upward band bending is reduced by an amount proportional to E_{fb}. In this case, a small amount of majority carriers is induced close to the interface leading to a decrease in depletion width, increase in capacitance and decrease in impedance. On the other hand, for a negative charge molecular layer, the upward bending is increased and also the flat band potential moves towards more negative values. In addition, an increase in impedance and decreased capacitance are expected due a larger depletion width. For more details see the illustration in Figure 41.

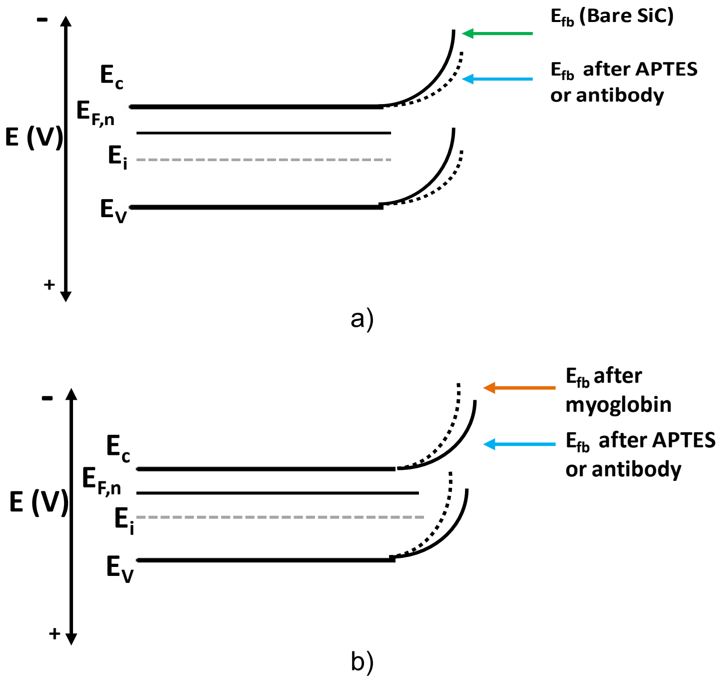

Figure 41 Schematic that illustrates the change in band bending after a) APTES, antibody immobilization and b) protein binding to antibody modified surfaces.

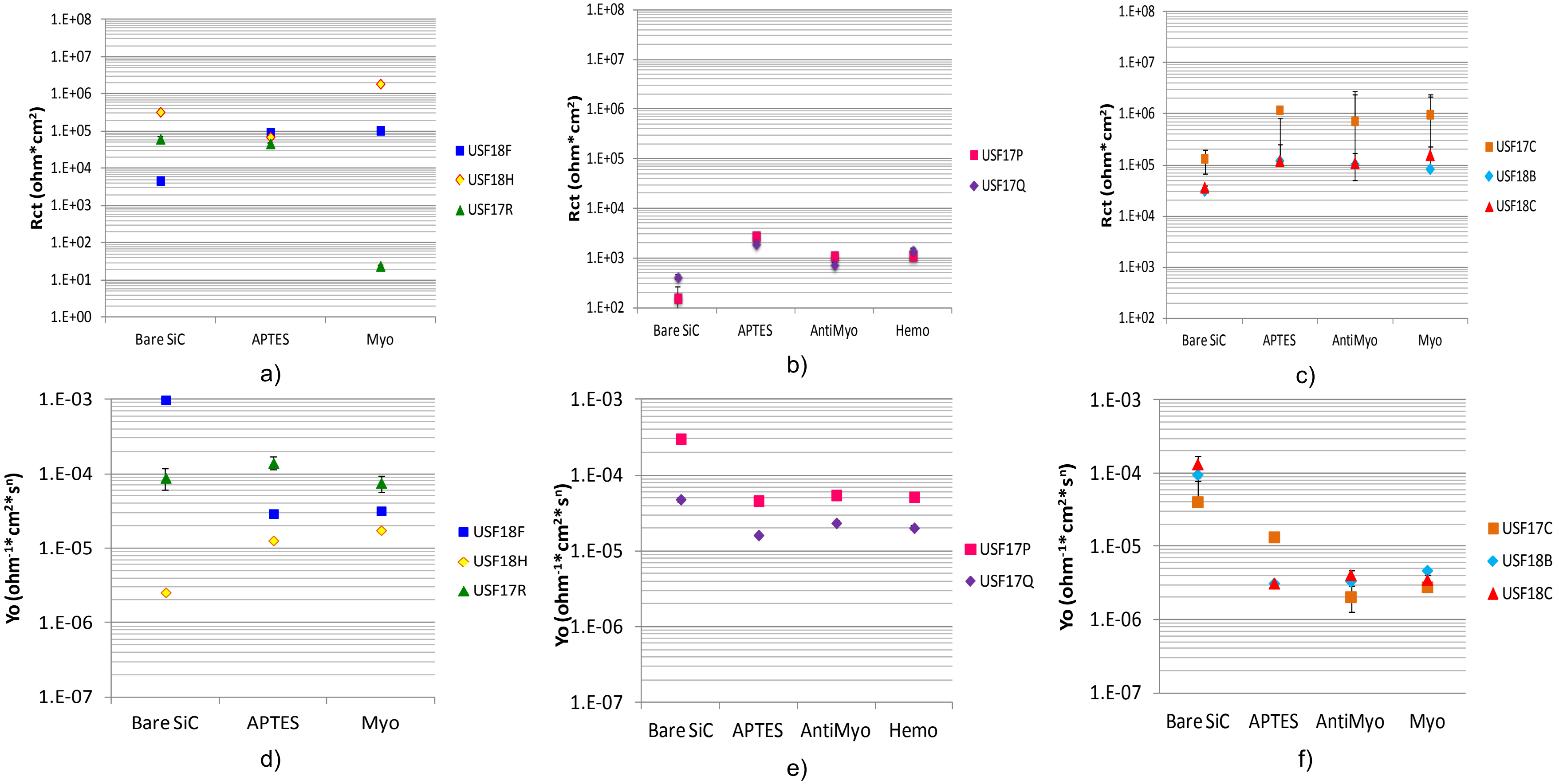

a)

b)

c)

d)

e)

f)

Figure 42 Fitted values of R_{ct} for a) surfaces C*, b) surfaces B*, and c) surfaces A*. Fitted values of C_{dl} for d) surfaces C*, e) surfaces B*, and f) surfaces A*. These values were obtained after fitting the equivalent circuit model described in Figure 40.

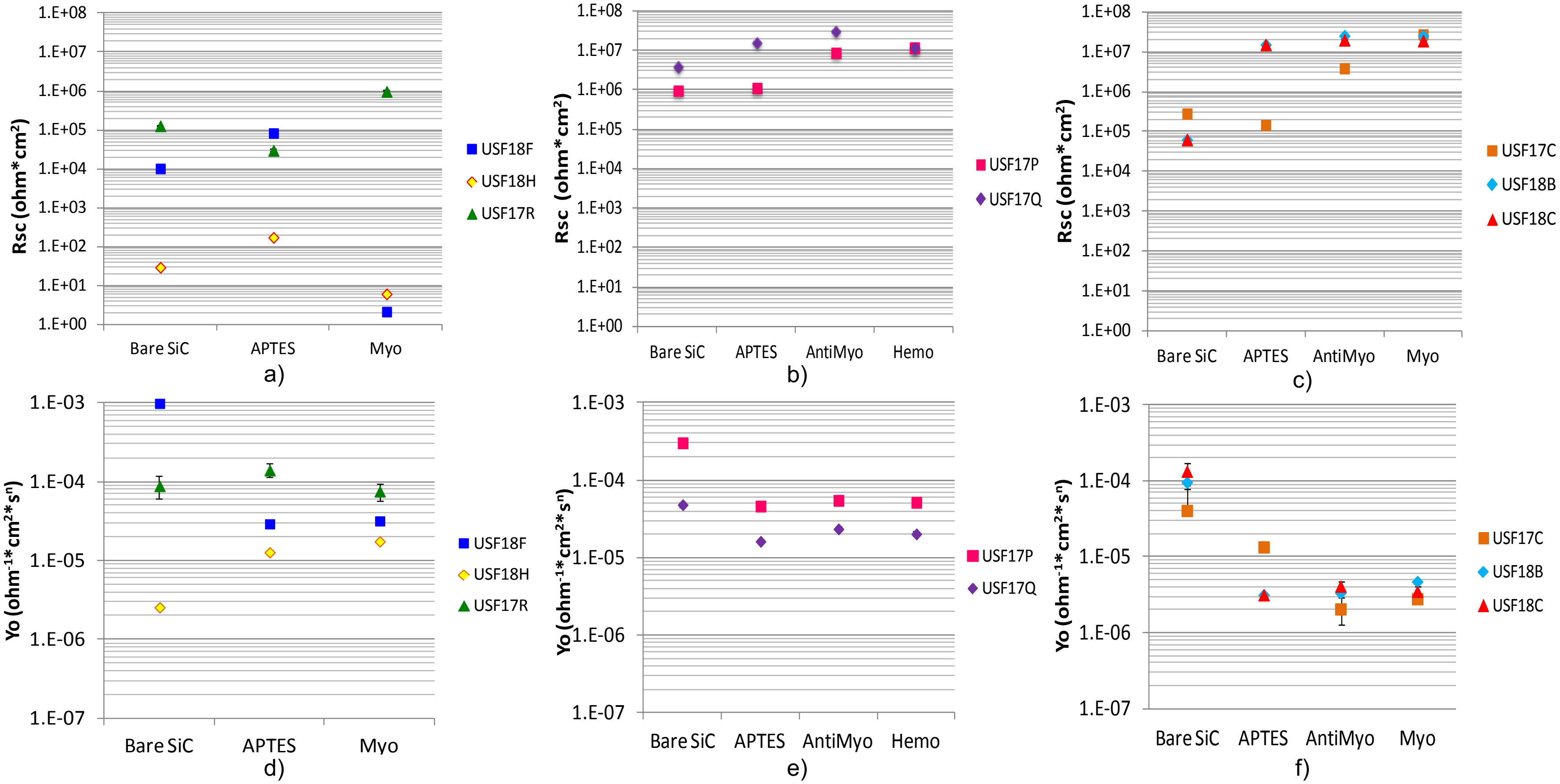

Figure 43 Fitted values of R_{cs} for a) surfaces C*, b) surfaces B*, and c) surfaces A*. Fitted values of C_{sc} d) surfaces C* e) surfaces B* and f) surfaces A*. These values were obtained after fitting the equivalent circuit model in Figure 40.

Table 3 Percentage change in the values of R_{ct}, C_{dl}, R_{cs} and C_{sc} for surface C*.

	Rct		Cdl	
	∆ APTES-Bare	∆ Myo-APTES	∆ APTES-Bare	∆ Myo-APTES
18F	1895.78	12.40	-97.03	8.94
18H	-78.61	2568.54	397.75	37.46
17R	-24.64	-99.95	58.46	-46.06
	Rsc		Csc	
18F	712.24	-100.00	28.25	15.02
18H	488.43	-96.48	0.53	81.70
17R	-76.54	3161.57	590.68	□.76

Table 4 Percentage change in the values of R_{ct}, C_{dl}, R_{cs} and C_{sc} for surface B*.

	Rct			Cdl		
	∆ APTES-Bare	∆ AntiMyo-APTES	∆ Hemo-AntiMyo	∆ APTES-Bare	∆ AntiMyo-APTES	∆ Hemo-AntiMyo
17P	1691	-60.44	-4.22	-84.7	18.54	-5.5
17Q	371.54	-61.16	94.38	-66.32	44.63	-13.75
	Rsc			Csc		
17P	19	671.8	3537	-11.44	19.45	2.5
17Q	290	94.1	-60.66	-9.78	44	-6.28

Table 5 Percentage change in the values of R_{ct}, C_{dl}, R_{cs} and C_{sc} for surface A*.

	Rct			Cdl		
	∆ APTES-Bare	∆ AntiMyo-APTES	∆ Myo-AntiMyo	∆ APTES-Bare	∆ AntiMyo-APTES	∆ Myo-AntiMyo
17C 18C 18B	785 231.9 285.8	-38.9 -9.4 -14.4	34.6 43.4 -20	-66.8 -97.5 -96.7	-84.7 29.9 6.7	36.2 -14.5 40.4
	Rsc			Csc		
17C 18C 18B	-48.4 24250.3 24250.3	2539.8 30.9 67.34	611.3 -4.6 -0.01	-55.76 2.93 -100	14.57 -100 38.4	-14.4 7.9 -0.03

4.5 Cyclic Polarization Tests on 3C-SiC

A potentiodynamic scan taken on a 3C-SiC sample after OH termination is illustrated in Figure 44. At potentials higher than -0.1 V (vs. SCE) the oxidation/reduction rates were small, with typical currents of ~ 2-3 x 10^{-8} A/cm^2. This behavior is typical of a passivated surface with no apparent redox reaction occurring in the system [8]. Small (or no) hysteresis was observed for the samples tested. At more negative (cathodic) potentials a cathodic reaction with limiting current on the order of 10^{-5} A/cm^2 and with tafel slope [8] of ~ 100- 150 mV/decade was identified. Therefore for these measurements the voltage sweep was limited to -0.6 V to 0.6 V (vs. SCE) to avoid any reaction due to H_2 evolution or O_2 reduction that could affect the measurements [8].

However, the cathodic reaction observed in Figure 44 could be in part due to O_2 present in air because the experiments were not performed in an Ar or N_2 environment. No increase was observed after performing the APTES or anti-myoglobin immobilization and the anodic current decreased slightly to 1-2 x10^{-8} A/cm^2. The same was observed when the values of the open circuit potentials were ~ -100 ± 50 mV (vs. SCE) with only a 10% increase (at most) after surface modification.

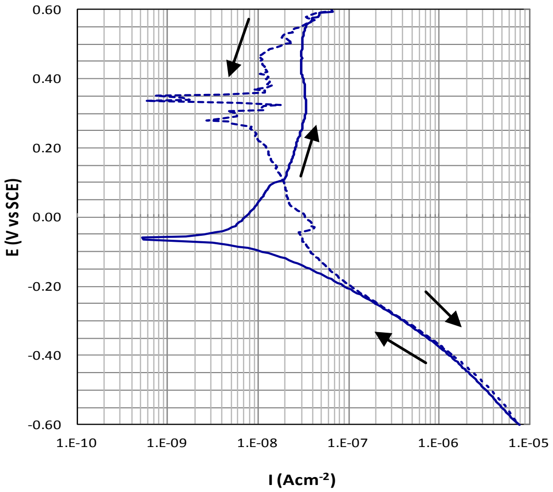

Figure 44 Potentiodynamic scan taken on SiC after OH termination. The arrows indicate the direction of the scans.

4.6 Mott-Schottky Plots of Functionalized 3C-SiC

The Mott-Schottky plots obtained for the same surfaces described in the previous section provided some information that could help us to better understand the impedance results. However, a strong hysteresis was observed on some specimens which can be due to the presence of surface states and defects as described in section4.1.1. For the analysis of the Mott-Schottky plots, we used a model that included the series resistance (R_s) due to the reference electrode, in series with a capacitor due to the semiconductor (C_{sc}) in parallel with a resistor (R_{sc}) to account for imperfections of the material.

4.6.1 Analysis of Mott-Schottky Plots for Surface C*

The results obtained for surface C* are shown in Figure 45. For specimen 18F after OH termination a small peak close to -150 mV (vs. SCE) was identified which can be attributed to the presence of surface states [212]. On both specimens 18F and 17R the value of the capacitance increases after both APTES functionalization and myoglobin immobilization. While there was not a big difference in capacitance on sample 18F after APTES, there was after myoglobin incubation (a 3X increase). This behavior was not expected for sample 18F because for this sample we assumed that myoglobin was not bound to the modified 3C-SiC surface based on the Nyquist and impedance results (see Figure 34 and Figure 35). On the other hand, there was a ~ 2X increase in capacitance from the bare substrate to the myoglobin immobilization for sample 17R. We tried to maintain the same scale for the Mott-Schottky plots but given the more pronounced changes in sample 17R compared to sample 18F.

Using the plots in Figure 45c and Figure 45d and equation (11) we found the flat band potential (E_{fb}) for the three specimens used to test surface C*. As we can see there is a strong frequency dependence that is confirmed in Figure 46. At 10 kHz the values of the capacitance are lower compare to the values obtained at 1 kHz. In addition, the change in capacitance after

APTES and myoglobin incubation is less at 10kHz than at 1kHz, which could be due to the presence of surface states that have less effect at higher frequencies [151].

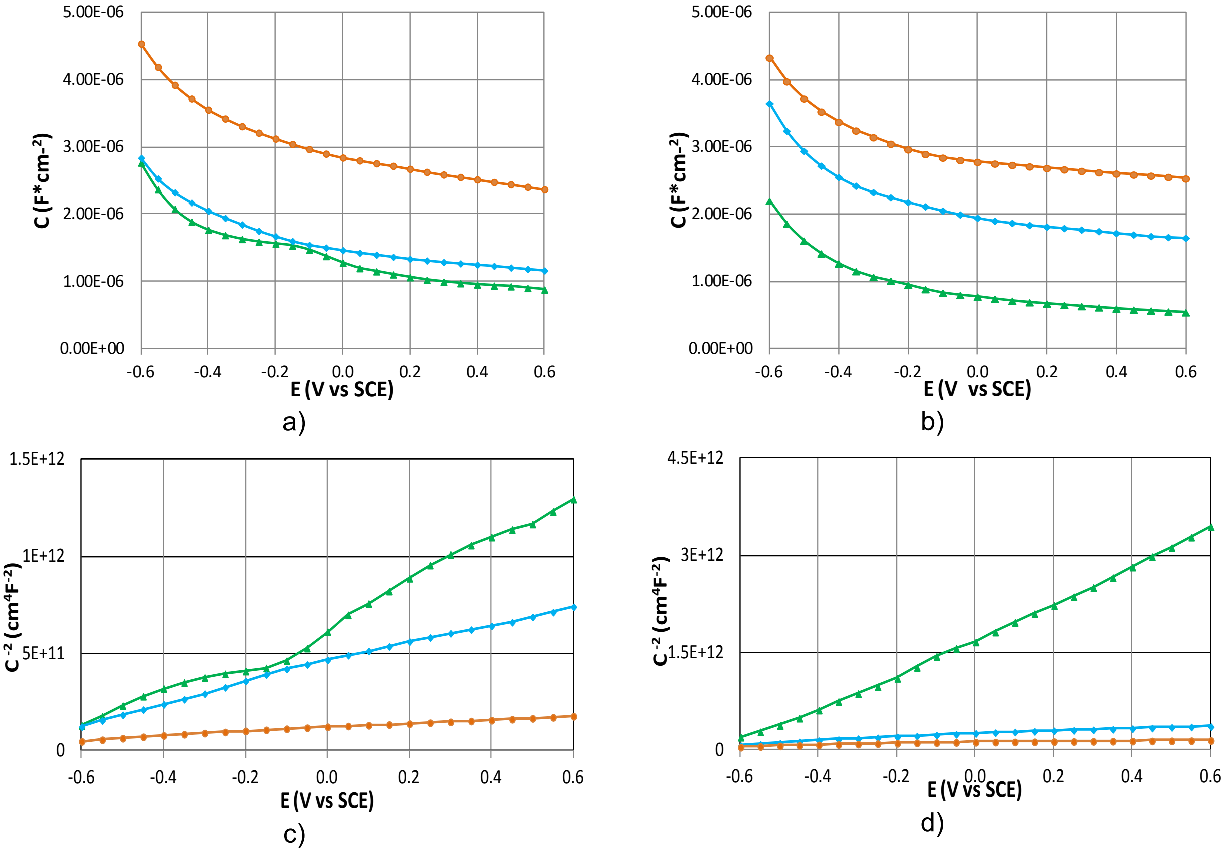

a)

b)

c)

d)

Figure 45 CV and Mott-Schottky plots obtained for each layer needed to form surface C* at 1kHz on specimen a) and c) 18F obtained from wafer USF1-13-18 and b) and d) 17R from wafer USF1-13-17. ▲ Bare SiC ◆ APTES, ● Myoglobin. E denotes potential which is reported with respect to the SCE (saturated calomel electrode).

We can see in Table 6 that, in general, the flat band potentials are more negative at all of the higher frequencies. For specimen 17R the standard deviation presents values that are almost half of the calculated flat band potentials. The high values obtained for the standard deviation of the E_{fb} is a consequence of the hysteresis observed after running successive experiments from -0.6V to 0.6 V (vs. SCE) and in the opposite direction. The hysteresis could rise from the defects described in section 4.1.1 and surface states (trapped charges and recombination), which was also seen in the variation of the value of N_d calculated after each treatment. It was not possible to identify a clear trend in the values for the flat band potential for the three specimens. For samples 18F and 17R we have seen that after APTES functionalization the E_{fb} shift is negative which indicates the presence of negative charges on the surface. This is contrary to the case of sample 18H where E_{fb} shifted to more positive values. The higher value observed at 10kHz could be due to protonation of APTES. A similar trend was observed by Yu *et al* and was considered a consequence of the density of surface states in the semiconductor [213]. There are different parameters that influence a shift in E_{fb} after surface modification such as defects and surface dipoles [214].

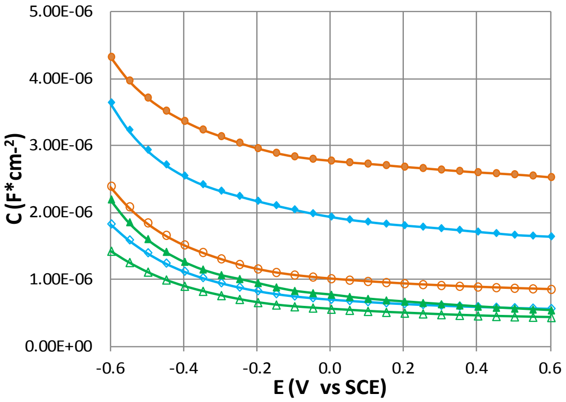

Figure 46 Comparison of CV plots obtained for surface C* at 1kHz (▲ Bare SiC ◆ APTES, ● Myoglobin) and 10kHz (△ Bare ◇ APTES ○Myoglobin) on specimen 17R. E denotes potential, which is reported with respect to the SCE (saturated calomel electrode).

4.6.2 Analysis of Mott-Schottky Plots for Surface B*

The CV and Mott-Schottky plots for the second control, i.e. surface B*, are shown in Figure 47. The capacitance decreases after APTES modification and anti-myoglobin immobilization. However, there is only a small increase in capacitance from the APTES to anti-myoglobin immobilization step and a small decrease after hemoglobin immobilization on the anti-myoglobin surfaces.

Table 6 Flat band potential at 1 kHz and 10 kHz for surface C*.

	Bare SiC		APTES			Myoglobin		
	E_{fb} (mV)	N_d (cm^{-3})	E_{fb} (mV)	N_d (cm^{-3})	Δ E_{fb} (mV)	E_{fb} (mV)	N_d (cm^{-3})	Δ E_{fb} (mV)
18H								
1kHz	-775±17.7	7.28×10^{18}	-755±35	1.45×10^{19}	20±0	-361.25±507	1.82×10^{20}	-530±763
10kHz	-875±3.5	3.64×10^{18}	-720±14	4.85×10^{18}	155±21	-1600±0	4.85×10^{19}	-880±28
18F								
1kHz	-590±84.8	1.46×10^{19}	-955±35	2.43×10^{19}	-365±120	-1200±212	1.46×10^{20}	-245±177
10kHz	-845±7	3.64×10^{18}	-875±35	7.28×10^{18}	-30±28	-1350±155	1.82×10^{19}	-475±35
17R								
1kHz	-593±298	1.46×10^{19}	-1316±702	7.28×10^{19}	-723±261	-2350±1504	3.64×10^{19}	-1175±672
10kHz	-790±456	1.46×10^{19}	-1000±577	7.28×10^{19}	-210±14	-1550±890.6	3.64×10^{18}	-550±70.7

For the two specimens shown in Figure 47 the results were similar at 1kHz and 10kHz, being the capacitance of specimen 17P was almost 3 times higher than that of sample 17Q. The fact that the capacitance is ~ 2 μF/cm^2 between 0.1V and 0.6 V (vs. SCE) can be due to the presence of surface states that at 1kHz and 10kHz affect the interface in a way that we see the effect of the double layer capacitance [215]. In both samples the same peak that was observed in specimen 18F is also seen around -0.15 V (vs. SCE) and it shifts to -0.2 V (vs. SCE) after the surface treatments. This is a consequence of surface states [212] which is confirmed in Figure 48. In this figure we can see that Mott-Schottky plots taken from -0.6 V to 0.6 V (vs. SCE) and in the opposite direction present hysteresis and in Figure 48a the first scan performed present and additional a peak ~ -0.15 V (vs. SCE) consistent with the behavior obtained in Figure 45a and that is attributed to charge trapping and recombination in [149].

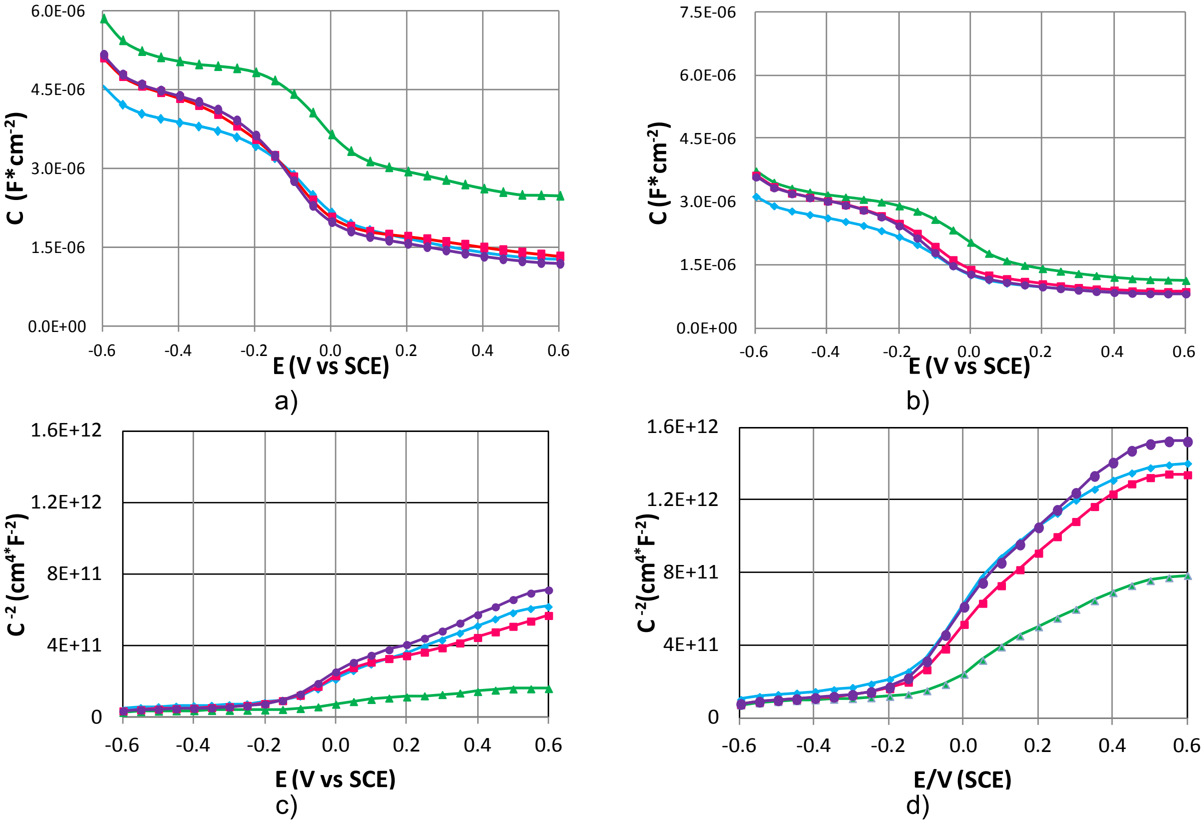

Figure 47 CV and Mott-Schottky plots obtained for each layer needed to form surface B* at 1kHz on specimen a) and c) 17P and b) and d) 17Q both from wafer USF1-13-17. ▲ Bare SiC ◆ APTES, ■ Anti-Myoglobin ● Hemoglobin.

The frequency dependence of the CV and Mott-Schottky plots taken on the specimens used to test surface B* is illustrated in Figure 48. A strong hysteresis effect is observed at 1 kHz that is reduced at 10 kHz but does not disappear at the higher frequencies, say at 100 kHz. The same effect is observed after taking the measurements on the modified surfaces. The reduced hysteresis effect after APTES and anti-myoglobin immobilization may be an indication of the passivation these layers provide by blocking any surface-charge exchange with the electrolyte. However, for these specimens the measurements obtained at 100 kHz showed consistent values of N_d from the starting surface to the last treatment, similar to the ones obtained for these specimens with a Hg probe. In addition, the error in the calculated E_{fb} (see Table 8) is less compared to the 1kHz experiments.

Increasing the test frequency to 100 kHz (see Figure 49) shows almost no change in capacitance after immobilization of hemoglobin, which confirms the specificity of the SiC-anti-myoglobin substrates as indicated in section 3.3.3.2. This behavior is also confirmed in the small change in E_{fb} obtained from the Mott-Schottky plot in Figure 49b. At this frequency we also see that at the more negative potentials the capacitance reaches a plateau that is more stable after APTES formation, which has been related to the organic layer blocking the electrons at the surface of the semiconductor [216].

The calculation of the E_{fb} did not provide consistent results for both specimens after each treatment at the different frequencies. In addition the values of the calculated N_d varied at 1kHz and 10kHz but was ~ 10^{18} cm^{-3} at 100kHz after each treatment was performed. This is an indication of a reduced impact of the surface states at higher frequency. The variability in N_d is also higher in sample 17P than in sample 17Q, which could be due to variations in SiC film thickness because the wafer was not rotated during the growth process (there is a slight variation in film thickness as a result). The higher N_d values measured for sample 17P could also explain why variations in the C_{dl} or how the molecular layer affects the CV shown in Figure 47.

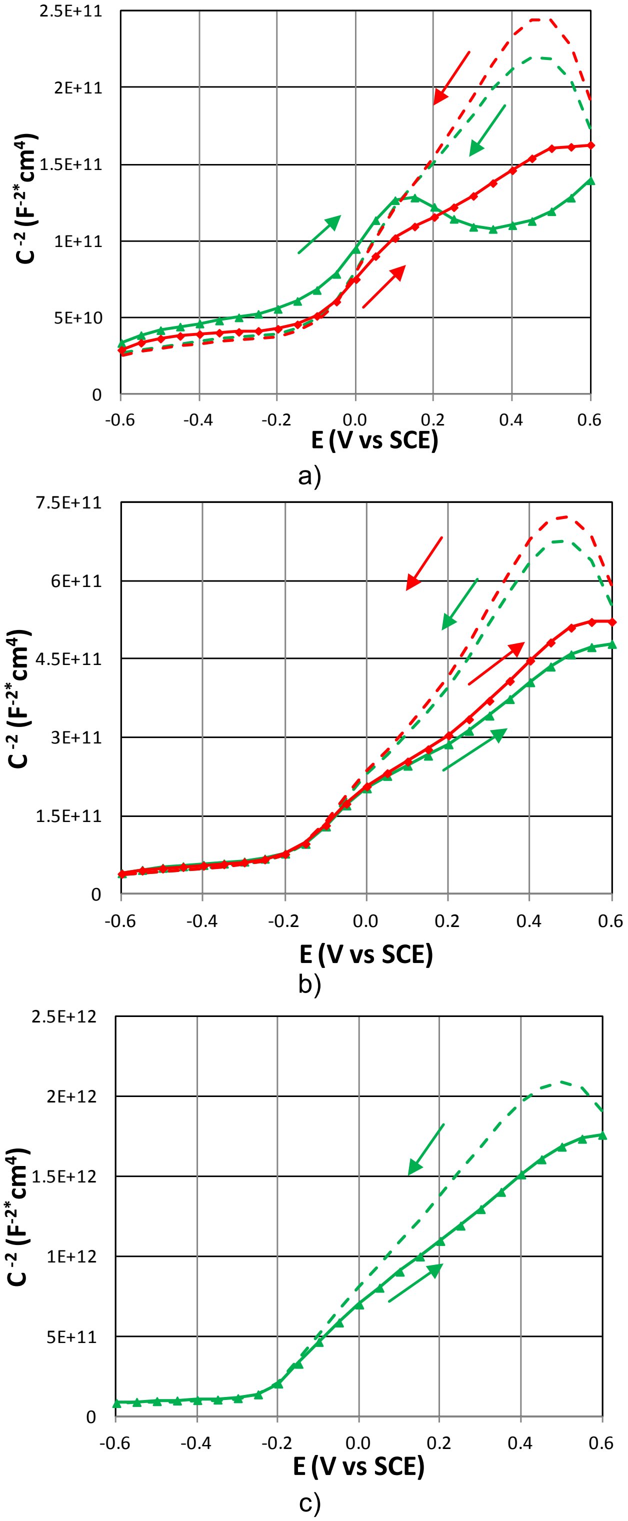

Figure 48 Mott-Schottky plots obtained for specimen 17P after OH termination at a) 1 kHz b) 10 kHz and c) 100kHz on specimen on 17P. —▲— and —◆— represent scans taken from -0.6 to 0.6 V each followed by - - - and - - - taken from 0.6 to -0.6 V.

In Table 7, the ΔE_{fb} after APTES was positive for sample 17P at 1kHz and 10kHz and negative at 100kHz. Sample 17Q showed negative values for ΔE_{fb} after APTES modification. As with the previous specimens, the high negative flat band potential can be a consequence of a high density of surface states. Similarly to the findings of Yu *et al.* for alkyl monolayers on n-type Si [213].

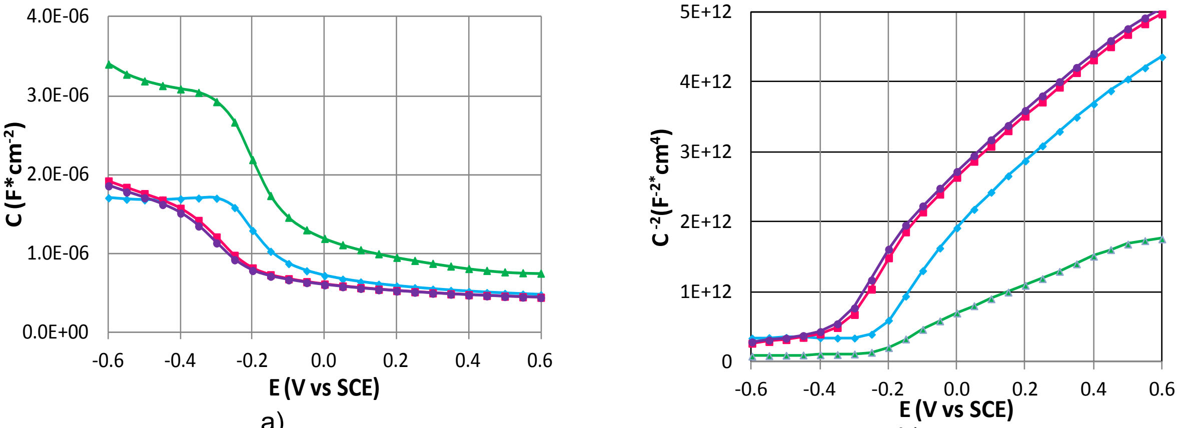

a)

b)

Figure 49 a) CV and b) Mott-Schottky plots obtained surface B* at 100kHz on specimen on 17P. ▲ Bare SiC ◆ APTES, ■ Anti-Myoglobin ■ Hemoglobin.

4.6.3 Analysis of Mott-Schottky Plots for Surface A*

For surface A*, the results also gave an indication of variability with an indication of possible myoglobin detection on one specimen out of the three that were tested. In this case, we also see the peak due to surface states in Figure 50a like specimens 18F and 17R in Figure 45 and 17P and 17Q in Figure 47. This could explain the higher values of capacitance observed in Figure 50a towards the more negative potentials. For both samples used to test surface A*, samples 17C and 18C showed that the capacitance decreased after APTES functionalization, but for anti-myoglobin and myoglobin immobilization the trend is different. On sample 17C, there is a small decrease in capacitance after anti-myoglobin immobilization where as it increases for sample 18C. After incubation of the myoglobin there is no change detected on sample 18C but a small increase in sample 17C that can also be seen in the Mott-Schottky plots shown in Figure 50c and Figure 50d.

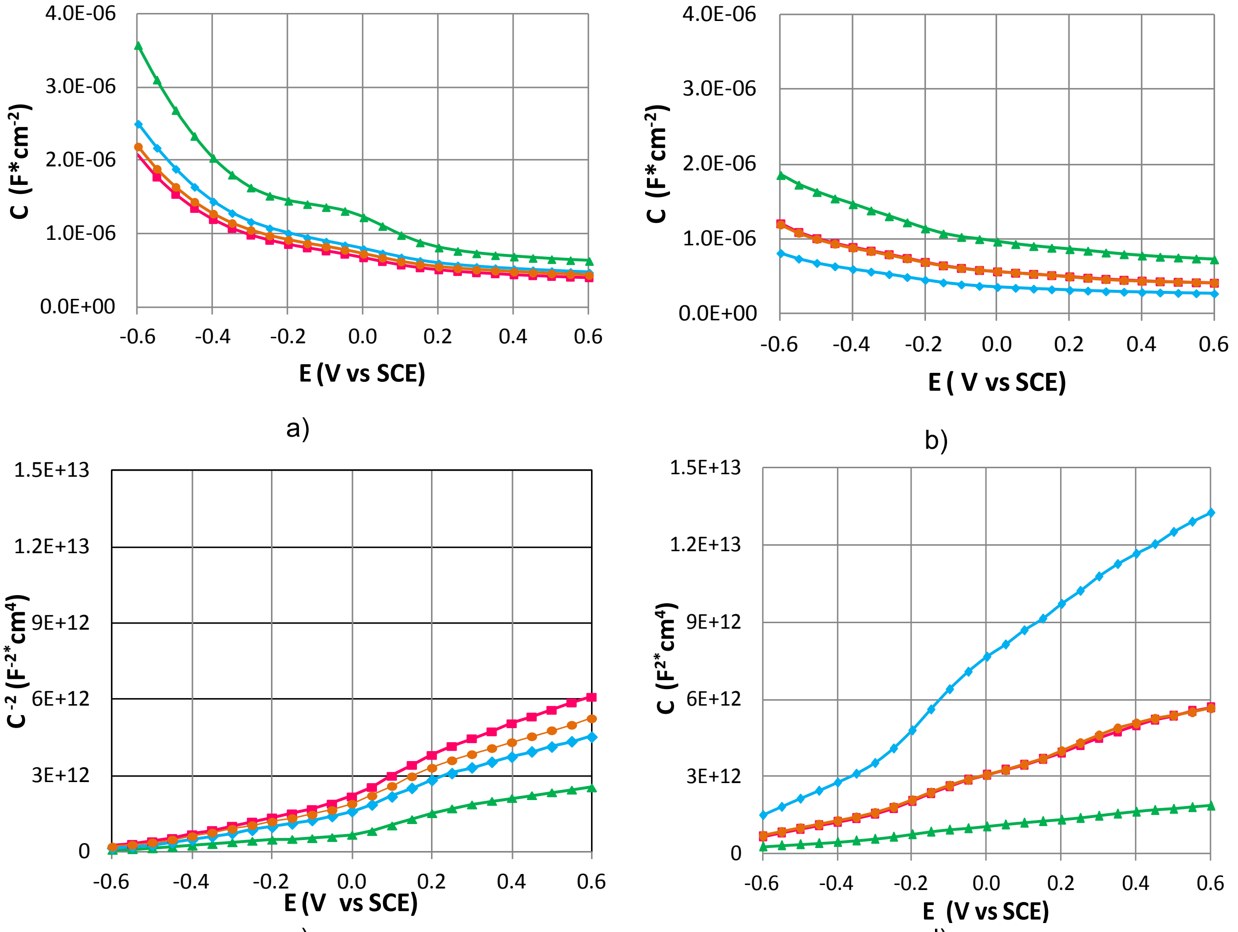

a) b)

c) d)

Figure 50 CV and Mott-Schottky plots obtained for each layer needed to form surface A* at 1kHz on specimen a) and c) 17C and b) and d) 18B. ▲ Bare SiC ◆ APTES, ■ Anti-Myoglobin ● Myoglobin. E denotes potential which is reported with respect to the SCE (saturated calomel electrode).

Table 7 Flat band potential at 1 kHz , 10 kHz and 100 kHz for surface B*.

	Bare SiC		APTES			Anti-Myoglobin			Hemoglobin		
	E_{fb} (mV)	N_d (cm^{-3})	E_{fb} (mV)	N_d (cm^{-3})	ΔE_{fb} (mV)	E_{fb} (mV)	N_d(cm^{-3})	ΔE_{fb}(mV)	E_{fb} (mV)	N_d(cm^{-3})	ΔE_{fb}(mV)
17P											
1kHz	-320±125	$5.26x10^{19}$	-236.7±35.6	$1.66x10^{19}$	83.3±91	-262±90.7	$1.85x10^{19}$	3±35	-265±120	$1.82x10^{19}$	-40±28
10kHz	-285±106	$2.1x10^{19}$	-267±62.6	$4.61x10^{18}$	7.5±33.1	-280±35.6	$6x10^{19}$	-2.5±35	-136.7±35	$1.46x10^{19}$	80±42
100kHz	-312±53	$6.1x10^{18}$	-465±11	$3.1x10^{18}$	-105±53	-615±11	$3.3x10^{18}$	-116±65	-625±17	$3.3x10^{18}$	-25±28
17Q											
1kHz	-175±58	$1.13x10^{19}$	-262±81	$5.5x10^{18}$	-87.5±74	-302±139	$7.9x10^{28}$	-40±175	-270±98	$6.7x10^{18}$	85±106
10kHz	-317±49.2	$5.7x10^{18}$	-483±125.8	$1x10^{20}$	-180±87.2	-375.3±29	$3.27x10^{18}$	100±100	-435±50	$3.27x10^{18}$	-60±14
100kHz	-650±0	$3.27x10^{18}$	-650±53	$2.5x10^{18}$	-37.5±53	-605±21	$2.7x10^{18}$	-7.5±75	-670±29	$2.7x10^{18}$	-65±50

Table 8 Flat band potential at 1 kHz and 10 kHz for surface A*.

	Bare SiC		APTES			Anti-Myoglobin			Myoglobin		
	E_{fb} (mV)	N_d (cm^{-3})	E_{fb} (mV)	N_d (cm^{-3})	ΔE_{fb}(mV)	E_{fb} (mV)	N_d(cm^{-3})	ΔE_{fb} (mV)	E_{fb} (mV)	N_d(cm^{-3})	ΔE_{fb} (mV)
17C											
1kHz	-500±70	$7.28x10^{18}$	-532.5±10	$3.64x10^{18}$.	-32.5±60.1	-535±21	$1.43x10^{18}$	-2.5±31.8	-545±35	$2.9x10^{18}$	-10±11
10kHz	-550±0	$7.28x10^{18}$	-562.5±8	$3.64x10^{18}$	-12.5±17.8	-567±3.3	$2.43x10^{18}$	-5±28	-582±0	$2.9x10^{18}$	-15±0
18C											
1kHz	-450±141	$1.1x10^{19}$	-800±141	$3.64x10^{18}$	-350±282	-740±268.7	$3.28x10^{18}$	60±127	-820±226.3	$3.28x10^{18}$	-80±42
10kHz	-685±91.9	$7.28x10^{18}$	-815±120.2	$2.9x10^{18}$	-130±212	-825±106	$3.28x10^{18}$	-10±14.1	-885±120.2	$2.7x10^{18}$	-65±14
18B											
1kHz	-623±81.4	$6.5x10^{18}$	-855±21.2	$1.61x10^{18}$	-260±113.1	-770±268.7	$3.28x10^{18}$	85±247	-780±254.5	$3.28x10^{18}$	-10±14
10kHz	-850±28.3	$7.28x10^{18}$	-835±50	$1.46x10^{18}$	15±77.8	-845±148.5	$2.9x10^{18}$	-10±98.9	-900±70.7	$2.9x10^{18}$	-55±78

For these specimens it was not possible to obtain one unique conclusion from the extrapolated flat band potentials. At 1 kHZ and 10 kHz, samples 17C and 18C had a ΔE_{fb} from -45 mV (vs. SCE) to -350 mV (vs. SCE) similar to sample 18B after APTES functionalization, although the later only had a $\Delta E_{fb.}$ of 15 (vs. SCE) Small changes in flat band potentials after surface functionalization have been linked to no surface dipole formation on the surface [213]. On the other hand, in the cases where the ΔE_{fb} is more than -100 mV can be a consequence of the presence of surface states [213]. For the surface with the immobilized anti-myoglobin the ΔE_{fb} is less than 100 mV (vs. SCE) for the three specimens being only -10 mV (vs. SCE) for sample 18B and 18C at 10 kHz.

After myoglobin immobilization we can see in Table 8 that a very negative ΔE_{fb} of ~ -1V (vs. SCE) was observed. Myoglobin presents a negative charge at pH higher than 5.3 [210] and for this reason the value that we found for the flat band potential after myoglobin immobilization on the anti-myoglobin surfaces could be an indication of the detection. However, if we consider the impedance results in Figure 38 and Figure 39 this could only be true for specimen 17C.

4.7 Discussion and Conclusions of the Myoglobin Detection on SiC Via Impedance Spectroscopy

Even though the data obtained for the impedance detection of myoglobin on functionalized 3C-SiC did not present a unified trend a few conclusions can be drawn from this work. One step that proved to be very important to successfully perform the binding of the protein to the surface was the preparation of the self-assembled monolayers. In section 3.1 we presented an extensive discussion in the preparation and characterization of self-assembled monolayers on SiC. Even though researchers have been successful in modifying the surface termination of SiC this technique may not be adequate to guarantee the success in the fabrication of a SiC-field effect device in contact with an electrolyte. This step will directly impact the covalent linking of the antibodies, which also has problems on its own as discussed in sections 1.3.1.2 and 3.3.3.

Since our main goal was to use the Mott-Schottky plots as the main characterization approach to determine successful detection of myoglobin on SiC it is worth to spend some time discussing some of the factors that could have impacted the variability in our results. One of the main issues could be the position of the reference electrode, as we mentioned in section 4.3, and the effective area that is exposed to the electrolyte that affects the apparent capacitance measured which could be a consequence of not accurately measuring the pressing force of the o-ring against the SiC sample. This could affect both the impedance and CV measurements and provide variable results.

From the Mott-Schottky plots, it was interesting to see a peak in the CV plots that other authors have seen as a consequence of the presence of surface states [216, 217]. In addition a strong frequency dependence was also seen in all the specimens tested, an example is shown in Figure 48 and Figure 49. This effect has been related to surface states [149, 156], non-uniform spatial doping and the presence of deep donor and acceptor impurities [151, 157].

In most of the Mott-Schottky plots we observed two slopes, even for the SiC before the chemical modification. Some authors have found a similar behavior on alkyl modified p-type and n-type Si, which indicates that due to the thin films the semiconductor does not reach inversion but goes into deep depletion and this has been explained by the presence of deep localized levels [218]. Lauermann *et al.* also found it difficult to obtain straight and reproducible Mott-Schottky plots with 6H-SiC and 3C-SiC, hence making it difficult to calculate accurately the flat band potential [219]. Similarly to what we have found, their extrapolated flat band potential is ~ -350 mV (vs. SCE) at pH 0 with an increase of 52 mV per pH, which gives ~ -450 mV (vs. SCE) at pH 7. The results presented in Table 6 to Table 8 showed similar values and some were higher in some cases. They concluded that the quality of the crystal and the presence of surface states, obtained from photocurrent measurements, affected significantly their results [219].

We also found that in some cases the flat band potential shifted towards more negative values after APTES and anti-myoglobin immobilization. Einati *et al.* found shifts towards positive potentials after APDEMS functionalization of p-type Si and an increase in the magnitude towards positive potentials have been attributed to protonation of the end-groups [214]. On the other hand, a decrease and/or more negative flat band potentials have been identified when negatively charged ions are adsorbed at a semiconductor surface [220]. And also on alkyl monolayers films prepared on n-type Si in addition to a decrease in capacitance after functionalization of the Si surfaces [213, 216]. The variability and flat band potential shift after surface functionalization can be affected by defects in the structure. In particular, APTES has been demonstrated to form in islands and tends to crosslink both the substrate and the organosilane itself preventing the crosslinking of other proteins effectively to the surface [221, 222]. In some cases, the quality of the monolayer is not an issue, but the rearrangement of the dipole charge on the substrate after adding the monolayer or the interaction of the monolayer with the electrolyte [214]. In order to understand if the last two phenomena are affecting our measurements further experimentation needs to be conducted.

Because of the variability on the results, we conclude that using the Mott-Schottky and impedance spectroscopy techniques proved not to be reliable to detect myoglobin immobilization under the specified conditions. Some authors have obtained similar uncertainty in their work with the immobilization of anti-α-fetoprotein on p-type Si for the detection of the respective antigen (α-fetoprotein). Due to inconsistency of their results at different frequencies the authors opted to use the real component of the impedance obtained after Mott-Schottky measurements at higher frequencies (e.g. 100kHz) to identify changes in antibody-antigen binding [11]. Similarly, Bataillard *et al.* investigated the detection of the same antigen using also anti-α-fetoprotein on p-type Si.

Because it was not possible to differentiate the flat band potential changes after the surface modifications these authors opted to extend their scanning potential range to analyze the molecular layer capacitance and not the capacitance in the space charge region of the semiconductor [223]. Both of these approaches could be implemented in our research, considering that by extending the voltage range other chemical processes could take place during the experiment.

More experiments should be performed in order to explain some of the trends observed for the parameters of the equivalent circuit model and the flat band potential shift. This includes using an electrolyte with different pH, performing the EIS measurements at a fixed DC bias with respect to the reference electrode, comparing the fitting of the data to other equivalent circuits, among other changes in the electrochemical cell that will be described in Chapter 5.

CHAPTER 5: CONCLUSIONS AND FUTURE WORK

There are many opportunities to use SiC as a substrate and active material to be incorporated in devices that require certain chemical, mechanical and electrical properties when implanted in the harsh environment of the human body. In this dissertation we presented a study that included the surface modification of SiC for the development of immunosensors. The polytype of interest was 3C-SiC because of the proven hema-compatibility and biocompatibility with several cell lines that indicated that it may be a viable substrate to detect biomarkers in blood. Moreover, there is still a need to look for more explanations to identify how surface charge, morphology, and chemical termination affect cell attachment and proliferation, as well as toxic and pharmacokinetic effects of SiC in-vivo. In order to address hema-compatibility in-vivo, hema-compatibility must be first studied under blood flow conditions and target the expression of specific proteins such as P-selectin and fibrinogen [110, 224, 225].

We were also interested in using SiC to build a device to predict silent myocardial infarction, because the integration of other materials and systems on SiC increases the possibilities to create complex devices that can perform multiple biomolecule detection and analysis on a single platform (i.e. system on a chip). At first glance, some of the proposed devices built on SiC could be considered costly because of the costs associated with material fabrication. At the same time, since SiC is a potential material for long-term device implantation, other costs associated with patient treatment and multiple surgeries for implant replacement can be reduced thus rendering SiC-based biosensors (like the one proposed in this work) more than cost effective, not to mention the obvious improvement in the quality of life for patients who can avoid repetitive surgical procedures.

5.1 Conclusions

In Chapter 2 we discussed some of the main advantages of using SiC in biosensors and summarized the type of polytype and crystal suitable for particular applications. This depends on a particular doping level selected in order for this material to be used in impedance or potentiostatic systems. Likewise, care should be taken in the characterization of the SiC film or polytype to be used. As we demonstrated in chapter4, the inherent presence of defects (e.g. stacking faults, voids, etc.) significantly impacts the response of electrically based biosensors.

Since the surface functionalization of SiC with organic molecules is recognized as a crucial step in biological sensor development, it has been demonstrated on all relevant forms of SiC. In chapter 3 we demonstrated the successful immobilization of anti-myoglobin and later, the detection of myoglobin via fluorescent microscopy. However, by performing impedance spectroscopy experiments in Chapter 4 the binding of myoglobin on SiC modified surfaces was not easy to identify. And we believe that the quality of the APTES films contributed significantly to the results. For this reason, we suggest that more efforts should be dedicated to further developing self-initiated photografting and photopolymerization (SIPGP) films on SiC [165, 226, 227]. These types of films could provide a more reproducible and uniform film for the precise immobilization of antibodies or other targeted proteins.

5.2 Future Work

Because of the high variability of the results observed in the impedance spectroscopy and Mott-Schottky measurements in sections 4.3 and 4.6, we propose to do several modifications to the electrochemical setup. This includes making a fixture that provides a precise method to fix the reference electrode (activated Ti mesh) every time the samples are inserted or removed from the setup. In addition, because initially an SU8 coating was used as a passivation layer for the electrode and it seemed to fail in some of the specimens thus affecting the results, we propose to increase the inside diameter of the inner electrode compared to the o-ring used to fix the sample. This way the metal of the electrode will not be exposed to the electrolyte and there are no chances of having parasitic capacitance effects due to a failed protective coating.

Another issue that was identified after building the cell was the use of screws to press the sample against the o-ring (see Figure 33). This may contribute to differences in apparent capacitance due to different pressure on the sample after surface treatment. It is not clear yet how to improve this but we need to find a way to fix the sample without pressing to hard and break it.

Using Si as a control experiment can also provide better insight into how the defects inherent in the SiC material affects the results. Some similarities have been observed with some of our results and similar work performed on Si. Because Si has been widely characterized and it has less surface defects, having a highly doped n-type Si crystal could help to predict impedance and flat band potential changes after the protein immobilization on these semiconductor surfaces. In addition, we can perform the analysis and fitting the impedance results with other equivalent circuit models that includes more resistive or capacitive elements that resemble failed coatings [207, 215]. On the other hand, we can focus our work into measuring the resistive or capacitive effect cause by the immobilized biomolecules implementing an analysis approach like the ones proposed by Souteyrand *et al.* [228] and Bataillard *et al.* [223] and described in section 4.7.

Lastly, since we also discussed in chapter 2 that SiC can be produced in different forms (e.g. BioSiC made from wood, *a*-SiC, nanoporous SiC, etc.) and polytypes (i.e. cubic, rombohedral and hexagonal) we can also explore the construction of interdigitated microelectrode (IME) arrays on amorphous-SiC (*a*-SiC). The initial idea when this dissertation work was started was to develop IMEs on SiC but, at the moment we did not have access to insulating SiC material. Recently, we have developed in the SiC group with the support of the

NREC staff, 200 nm *a*-SiC films (via PECVD) that do not present apparent defects or pinholes as demonstrated by the SEM images in Figure 51, taken at different magnifications with a Hitachi SU-70 SEM. We have also built some IMEs on *a*-SiC and SiO_2 using Ti/Au as the metal electrode with a 5 µm and 10 µm pitch. The sensors showed a small leakage current, a good indication of the insulating properties of the *a*-SiC films. However, some improvements may need to be done regarding the mask used to make the devices, such as undercutting and non-straight edges that were observed via SEM in Figure 52b.

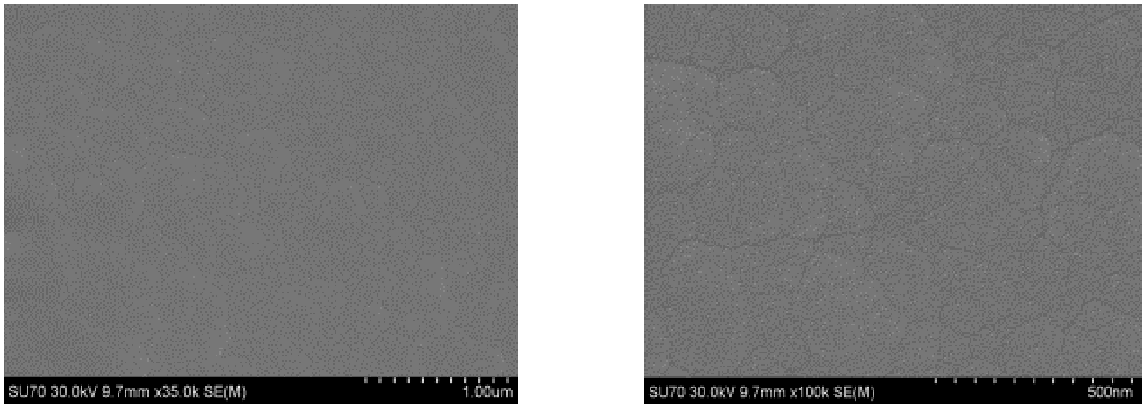

a) b)

Figure 51 SEM images taken on *a*-SiC films. Films deposited by J. Register and R. Everly in the Plasmatherm 700 PECVD took at the USF NREC core facility.

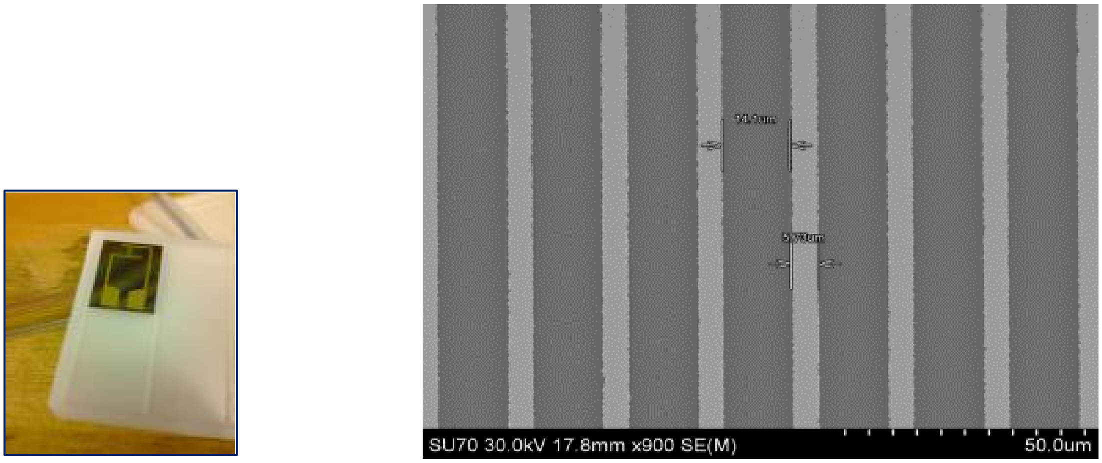

a) b)

Figure 52 Photograph of a) IME built on *a*-SiC and b) SEM image of the Ti/Au digits of the IME built on *a*-SiC.

REFERENCES

[1] A. Guiseppi-Elie, "An implantable biochip to influence patient outcomes following trauma-induced hemorrhage," *Anal Bioanal Chem,* vol. 399, pp. 403-419, 2011.

[2] P. Connolly, "The potential for biosensors in cardiac surgery," *Perfusion,* vol. 19, pp. 247-249, 2004.

[3] D. D. Gutterman, "Silent Myocardial Ischemia," *Circulation,* pp. 785 – 797, 2009.

[4] R. H. Christenson and H. M. E. Azzazy, "Biochemical markers of the acute coronary syndromes," *Clinical Chemistry,* vol. 44, pp. 1855–1864, 1998.

[5] S. E. Saddow, C. L. Frewin, C. Coletti, N. Schettini, E. Weeber, a. Oliveros*, et al.*, "Single-Crystal Silicon Carbide: A Biocompatible and Hemocompatible Semiconductor for Advanced Biomedical Applications," *Materials Science Forum,* vol. 679-680, pp. 824-830, 2011.

[6] A. Rzany, C. Harder, and M. Schaldach, " Silicon Carbide as an Anti-Thrombogenic Stent Coating: An Example of a Science-Based Development Strategy " *Progress in Biomedical Research,* vol. 5, pp. 168-78, 2000.

[7] C. Hehrlein, "aSiC : H-coated Stents Stent Passivation with Silicon Carbide as a Possible Alternative to Drug-eluting Stents – A Comprehensive Review of Pre-clinical and Clinical Results," *Interventional Cardiology,* vol. 4, pp. 60-63, 2009.

[8] A. Tlili, M. A. Jarboui, A. Abdelghani, D. M. Fathallah, and M. A. Maaref, "A novel silicon nitride biosensor for specific antibody–antigen interaction," *Materials Science and Engineering: C,* vol. 25, pp. 490-495, 6// 2005.

[9] A. Lloyd Spetz, S. Nakagomi, and S. Savage, "High temperature SiC-FET chemical gas sensors " in *Advances in Silicon Carbide Processing and Applications*, S. E. Saddow and A. Agrawal, Eds., ed Norwood, MA: Artech House, 2004, pp. 29–67.

[10] G. Gabriel, I. Erill, J. Caro, R. Gomez, D. Riera, R. Villa*, et al.*, "Manufacturing and full characterization of silicon carbide-based multi-sensor micro-probes for biomedical applications," *Microelectronics Journal,* vol. 38, pp. 406-415, Mar 2007.

[11] E. Souteyrand, J. P. Cloarec, J. R. Martin, C. Wilson, I. Lawrence, S. Mikkelsen*, et al.*, "Direct Detection of the Hybridization of Synthetic Homo-Oligomer DNA Sequences by Field Effect," *The Journal of Physical Chemistry B,* vol. 101, pp. 2980-2985, 1997.

[12] A. M. Gutierrez, G. R. Reboredo, S. M. Mosca, and A. Catala, "Fatty acid composition and lipid peroxidation induced by ascorbate-Fe2+ in different organs of goose (Anser anser)," *Comparative Biochemistry and Physiology C-Toxicology & Pharmacology,* vol. 137, pp. 123-132, Feb 2004.

[13] S. J. H. A. S. McLean, and M. Salter "Bench-to-bedside review: the value of cardiac biomarkers in the intensive care patient," *Critical care (London, England),* vol. 12, p. 215, 2008.

[14] N. K. J. Manoj, R. Lal, S. Mukherji, and V. Ramgopal Rao, *Bionanotechnology Global Prospects* vol. CRC Press: Boca Raton, 2009.

[15] M. Zafari, L. C. Afonso, K. Aggarwal, E. Bessman, and D. L. Coven, "Myocardial Infarction," ed, 2011.

[16] A. H. Ahmed, K. Shankar, H. Eftekhari, M. Munir, J. Robertson, A. Brewer*, et al.*, "Silent myocardial ischemia: Current perspectives and future directions," *Exp Clin Cardiol,* vol. 12, pp. 189-96, Winter 2007.

[17] C. Pepine, "Silent myocardial ischemia: Definition, magnitude, and scope of the problem," *Cardiology Clinics,* vol. 4, pp. 577 – 581, 1986.

[18] Y. Rozenman and M. S. Gotsman, "THE EARLIEST DIAGNOSIS OF ACUTE MYOCARDIAL-INFARCTION," *Annual Review of Medicine,* vol. 45, pp. 31-44, 1994.

[19] K. A. Ammar, J. A. Kors, B. P. Yawn, and R. J. Rodeheffer, "Defining unrecognized myocardial infarction: a call for standardized electrocardiographic diagnostic criteria," *Am Heart J,* vol. 148, pp. 277-84, Aug 2004.

[20] K. Komukai, T. Ogawa, H. Yagi, T. Date, K. Suzuki, H. Sakamoto*, et al.*, "Renal insufficiency is related to painless myocardial infarction," *Circ J,* vol. 71, pp. 1366-9, Sep 2007.

[21] A. M. Amanullah and K. Lindvall, "Prevalence and significance of transient — Predominantly asymptomatic — Myocardial ischemia on Holter monitoring in unstable angina pectoris, and correlation with exercise test and thallium-201 myocardial perfusion imaging," *The American Journal of Cardiology,* vol. 72, pp. 144-148, 7/15/ 1993.

[22] H. Mickley, "Ambulatory ST segment monitoring after myocardial infarction," *Brittish Heart Journal,* vol. 71, pp. 113-114, 1994.

[23] M. Plebani and M. Zaninotto, "Cardiac markers: present and future," *International journal of clinical & laboratory research,* vol. 29, pp. 56-63, 1999.

[24] B. Dey, R. Jain, A. Khera, V. Rao, N. Dhar, U. D. Gupta*, et al.*, "Boosting with a DNA vaccine expressing ESAT-6 (DNAE6) obliterates the protection imparted by recombinant BCG (rBCGE6) against aerosol Mycobacterium tuberculosis infection in guinea pigs," *Vaccine,* vol. 28, pp. 63-70, Dec 10 2009.

[25] K. M. Coy, G. A. Imperi, C. R. Lambert, and C. J. Pepine, "Silent myocardial ischemia during daily activities in asymptomatic men with positive exercise test responses," *The American Journal of Cardiology,* vol. 59, pp. 45-49, 1/1/ 1987.

[26] JHeuser, "Afib_ecg," ed: Wikimedia Commons, 2007.

[27] K. Thygesen, J. S. Alpert, and H. D. White, "Universal definition of myocardial infarction," *European heart journal,* vol. 28, pp. 2525-38, 2007.

[28] A. S. Jaffe, L. Babuin, and F. S. Apple, "Biomarkers in acute cardiac disease: the present and the future," *Journal of the American College of Cardiology,* vol. 48, pp. 1-11, 2006.

[29] A. J. Anderson, "The Temperature Dependence of the Formal Potential and the Rate Constant of the Heterogeneous Electron-Transfer Reaction of Myogl," 1999.

[30] W. S. Kilpatrick, R. J. Spooner, P. Grant, and W. Tullett, "Is rapid myoglobin measurement of diagnostic value in the emergency presentation of non-traumatic chest pain?," *Journal of Accident Emergency Medicine,* vol. 11, pp. 267-269, 1994.

[31] M. Plebani and M. Zaninotto, "Diagnostic strategies using myoglobin measurement in myocardial infarction," *Clinica chimica acta; international journal of clinical chemistry,* vol. 272, pp. 69-77, 1998.

[32] S. Takeda, A. Yamashita, K. Maeda, and Y. Maéda, "Structure of the core domain of human cardiac troponin in the Ca(2+)-saturated form," *Nature,* vol. 424, pp. 35-41, 2003.

[33] A. S. Jaffe, J. Ravkilde, R. Roberts, U. Naslund, and F. S. Apple, "It's time for a change to a troponin standard," *Online,* pp. 1216-1220, 2000.

[34] D. Novis, B. Jones, J. C. Dale, and M. K. Walsh, "Biochemical markers of myocardial injury test turnaround time: a College of American Pathologists Q-Probes study of 7020 troponin and 4368 creatine kinase-MB determinations in 159 institutions," *Archives of pathology & laboratory medicine,* vol. 128, pp. 158-64, 2004.

[35] D. M. Dawson, H. M. Eppenberger, and M. E. Eppenberger, "Multiple molecular forms of creatine kinases," *Annals of the New York Academy of Sciences,* vol. 151, pp. 616-26, 1968.

[36] A. González Oliva, H. J. Cruz, and C. C. Rosa, "Immunosensors for Diagnostics," *Sensors Update,* vol. 9, pp. 283-312, 2001.

[37] W. M. Albers, I. Vikholm, T. Viitala, and J. Peltonen, "Chapter 1 - Interfacial and Materials Aspects of the Immobilization of Biomolecules onto Solid Surfaces," in *Handbook of Surfaces and Interfaces of Materials*, N. Hari Singh, M.Sc, and M. S. P. D. Ph.D.A2 - Hari Singh Nalwa, Eds., ed Burlington: Academic Press, 2001, pp. 1-31.

[38] K. Elgert, "Chapter 4: Antibody structure and function," in *Immunology: Understanding the immune system*, ed: John Wiley & Sons, Inc, 1998, pp. 58-78.

[39] V. H. J. D. Andrade, "Protein adsorption and materials biocompatibility: A tutorial review and suggested hypotheses," in *Advances in polymer science. Biopolymers/non-exclusion HPCL*. vol. 79, ed Berlin, GE: Springer-Verlag, 1987, pp. 8-10.

[40] F. Rusmini, Z. Zhong, and J. Feijen, "Protein Immobilization Strategies for Protein Biochips," *Biomacromolecules,* vol. 8, pp. 1775-1789, 2007/06/01 2007.

[41] A. Abdelghani, S. Hleli, and K. Cherif, "Optical and electrochemical characterization of self-assembled octadecyltrichlorosilane monolayer on modified silicon electrode," *Materials Letters,* vol. 56, pp. 1064-1068, 11// 2002.

[42] C. J. Barrelet, D. B. Robinson, J. Cheng, T. P. Hunt, C. F. Quate, and C. E. D. Chidsey, "Surface Characterization and Electrochemical Properties of Alkyl, Fluorinated Alkyl, and Alkoxy Monolayers on Silicon," *Langmuir,* vol. 17, pp. 3460-3465, 2001/05/01 2001.

[43] G. A. Campbell and R. Mutharasan, "Detection and quantification of proteins using self-excited PZT-glass millimeter-sized cantilever," *Biosensors and Bioelectronics,* vol. 21, pp. 597-607, 10/15/ 2005.

[44] M. G. Sankalia, R. C. Mashru, J. M. Sankalia, and V. B. Sutariya, "Physicochemical characterization of papain entrapped in ionotropically cross-linked kappa-carrageenan gel beads for stability improvement using Doehlert shell design," *Journal of Pharmaceutical Sciences,* vol. 95, pp. 1994-2013, 2006.

[45] A. J. Fleischman, S. Roy, C. A. Zorman, and M. Mehregany, "Behavior of polycrystalline SiC and Si surface-micromachined lateral resonant structures at elevated temperatures," *Silicon Carbide, Iii-Nitrides and Related Materials, Pts 1 and 2,* vol. 264-2, pp. 889-892, 1998.

[46] S. Luo and D. R. Walt, "Avidin-biotin coupling as a general method for preparing enzyme-based fiber-optic sensors," *Analytical Chemistry,* vol. 61, pp. 1069-1072, 1989/05/01 1989.

[47] G. Palestino, V. Agarwal, R. Aulombard, E. a. Pérez, and C. Gergely, "Biosensing and Protein Fluorescence Enhancement by Functionalized Porous Silicon Devices," *Langmuir,* vol. 24, pp. 13765-13771, 2008/12/02 2008.

[48] E. Barsoukov and J. R. Macdonald, *Impedance Spectroscopy Theory, Experiment, and Applications*, 2nd ed. ed. Hoboken: John Wiley & Sons, Inc, 2005.

[49] G. Barbero, A. L. Alexe-Ionescu, and I. Lelidis, "Significance of small voltage in impedance spectroscopy measurements on electrolytic cells," *Journal of Applied Physics,* vol. 98, pp. 113703-5, 12/01/ 2005.

[50] D. Kell, "The principles and potential of electrical admittance spectroscopy: an introduction," in *Biosensors: Fundamentals and Applications*, A. Turner, I. Karube, and G. Wilson, Eds., ed Oxford: Oxford University Press, 1987.

[51] J. S. Daniels and N. Pourmand, "Label-Free Impedance Biosensors: Opportunities and Challenges," *Electroanalysis,* vol. 19, pp. 1239-1257, May 16 2007.

[52] A. J. Bard and L. R. Faulkner, *Electrochemical methods : fundamentals and applications*. New York: Wiley, 1980.

[53] I. O. K'Owino and O. A. Sadik, "Impedance Spectroscopy: A Powerful Tool for Rapid Biomolecular Screening and Cell Culture Monitoring," *Electroanalysis,* vol. 17, pp. 2101-2113, 2005.

[54] P. Zoltowski, "On the electrical capacitance of interfaces exhibiting constant phase element behaviour," *Journal of Electroanalytical Chemistry,* vol. 443, pp. 149-154, 2/10/ 1998.

[55] K. B. Oldham, A. M. Bond, and J. C. Myland, *Electrochemical science and technology fundamentals and applications*. Chichester, West Sussex, U.K: John Wiley & Sons, 2012.

[56] B. Y. Chang and S. M. Park, "Electrochemical Impedance Spectroscopy," in *Annual Review of Analytical Chemistry, Vol 3*. vol. 3, E. S. Yeung and R. N. Zare, Eds., ed Palo Alto: Annual Reviews, 2010, pp. 207-229.

[57] L. Yang and A. Guiseppi-Elie, "Impedimetric Biosensors for Nano- and Microfluidics," in *Encyclopedia of Microfluidics and Nanofluidics*, D. Li, Ed., ed: Springer, 2008, pp. 811-823.

[58] P. Castro, A. A. Sagues, E. I. Moreno, L. Maldonado, and J. Genesca, "Characterization of activated titanium solid reference electrodes for corrosion testing of steel in concrete," *Corrosion* vol. 58, pp. 609-617, 1996.

[59] P. B. Luppa, L. J. Sokoll, and D. W. Chan, "Immunosensors—principles and applications to clinical chemistry," *Clinica Chimica Acta,* vol. 314, pp. 1-26, 12// 2001.

[60] C. J. McNeil, D. Athey, and R. Renneberg, "Immunosensors for clinical diagnostics," *EXS,* vol. 81, pp. 17-25, 1997.

[61] J. Rishpon, Gezundhajt, Y., Soussan, L., Rosen-Margalit, I., Hadas, E., "Biosensor Design and Applications," in *ACS Symposium Series*, P. R. Mathewson and J. W. Finley, Eds., ed Washington, DC: American Chemical Society 511, 1992.

[62] A. P. F. Turner, Karube, I., Wilson, G.S., *Biosensors: Fundamentals and Applications*. Oxford: Oxford Science Publications, 1987.

[63] M. Grattarola and G. Massobrio, *Bioelectronics handbook : MOSFETS, biosensors, and neurons / Massimo Grattarola, Giuseppe Massobrio*: New York : McGraw-Hill, c1998., 1998.

[64] U. Brand, B. Reinhardt, F. Rüther, T. Scheper, and K. Schügerl, "Bio-field-effect transistors for process control in biotechnology," *Sensors and Actuators B: Chemical,* vol. 4, pp. 315-318, 6// 1991.

[65] B. A. Lawton, Z. H. Lu, R. Pethig, and Y. Wei, "Physico-Chemical studies of the activity of urease and the development of a conductimetric urea sensor," *Journal of Molecular Liquids,* vol. 42, pp. 83-98, 10// 1989.

[66] A. Guiseppi-Elie, Wallace, G.G., Matsue, T., "Chemical and biological sensors based on electrocally conductive polymers," in *Handbook of Conducting Polymers*. vol. Two, T. Skotheim, Elsenbaumer, R., Reynolds, J. R., Ed., 3rd ed. ed New York: Marcel Dekker, 1998, pp. 963-992.

[67] A. Oliveros, A. Guiseppi-Elie, and S. Saddow, "Silicon carbide: a versatile material for biosensor applications," *Biomedical Microdevices,* vol. 15, pp. 353-368, 2013/04/01 2013.

[68] A. Lloyd Spetz, S. Nakagomi, H. Wingbrant, M. Andersson, A. Salomonsson, S. Roy*, et al.*, " New Materials for Chemical and Biosensors " *Materials and Manufacturing Processes,* vol. 21, pp. 253-6, 2006.

[69] R. Yakimova, R. M. Petoral, G. R. Yazdi, C. Vahlberg, A. Lloyd Spetz, and K. Uvdal, "Surface functionalization and biomedical applications based on SiC," *Journal of Physics D: Applied Physics,* vol. 40, pp. 6435-6442, 2007.

[70] P. Fromhertz, "The Neuron-semiconductor Interface," in *In Bioelectronics: From Theory to Applications*, I. Willner and E. Katz, Eds., ed Weinheim: Wiley-VCH Verlag, 2005, pp. 339-393.

[71] P. Bergveld, "Thirty years of ISFETOLOGY," *Sensors and Actuators B* vol. 88, pp. 1-20, 2003.

[72] P. J. Rousche and R. A. Normann, "Chronic recording capability of the Utah Intracortical Electrode Array in cat sensory cortex," *Journal of neuroscience methods,* vol. 82, pp. 1-15, 1998.

[73] G. Steinhoff, O. Purrucker, M. Tanaka, M. Stutzmann, and M. Eickhoff, "AlxGa1–xN—A New Material System for Biosensors," *Advanced Functional Materials,* vol. 13, pp. 841-6, 2003.

[74] R. P. Otoole, S. G. Burns, G. J. Bastiaans, and M. D. Porter, "Thin Aluminum Nitride Film Resonators - Miniaturized High-Sensitivity Mass Sensors," *Analytical Chemistry,* vol. 64, pp. 1289-1294, Jun 1 1992.

[75] C. Deger, E. Born, H. Angerer, O. Ambacher, M. Stutzmann, J. Hornsteiner*, et al.*, "Sound velocity of AlxGa1-xN thin films obtained by surface acoustic-wave measurements," *Applied Physics Letters,* vol. 72, pp. 2400-2402, May 11 1998.

[76] Y. Kawakami, S. Kamiyama, G. Hatakoshi, T. Mukai, Y. Narukawa, I. Nomura*, et al.*, "Photonic devices," in *In Wide Bandgap Semiconductors: Fundamental Properties and Modern Photonic and Electronic Devices*, K. Takahashi, A. Yoshikawa, and A. Sandhu, Eds., ed Heidelberg, Germany: Springer-Verlag, 2007, pp. 146-7.

[77] C. Coletti, M. J. Jaroszeski, A. Pallaoro, A. M. Hoff, S. Iannotta, and S. E. Saddow, "Biocompatibility and wettability of crystalline SiC and Si surfaces," *Conf Proc IEEE Eng Med Biol Soc,* pp. 5850-3, 22-26 August 2007 2007.

[78] C. L. Frewin, M. Jaroszeski, E. Weeber, K. E. Muffly, A. Kumar, M. Peters*, et al.*, "Atomic force microscopy analysis of central nervous system cell morphology on silicon carbide and diamond substrates," *Journal of Molecular Recognition,* vol. 22, pp. 380-388, Sep-Oct 2009.

[79] G. Kotzar, M. Freas, P. Abel, A. Fleischman, S. Roy, C. Zorman*, et al.*, "Evaluation of MEMS materials of construction for implantable medical devices," *Biomaterials,* vol. 23, pp. 2737-2350, 2002.

[80] T. J. Fawcett, J. T. Wolan, A. L. Spetz, M. Reyes, and S. E. Saddow, "Thermal detection mechanism of SiC based hydrogen resistive gas sensors," *Applied Physics Letters,* vol. 89, Oct 30 2006.

[81] A. J. Rosenbloom, Y. Shishkin, D. M. Sipe, Y. Ke, R. P. Devaty, and W. J. Choyke, "Porous Silicon Carbide as a Membrane for Implantable Biosensors," *Materials Science Forum,* vol. 457-460, pp. 1463-1466, 2004.

[82] J. Deva Reddy, A. A. Volinsky, C. L. Frewin, C. Locke, and S. E. Saddow, "Mechanical properties of single and polycrystalline SiC thin films," in *Materials Research Society Meeting*, 2008, pp. AA03 – AA06.

[83] M. Mehregany, C. A. Zorman, N. Rajan, and C. H. Wu, "Silicon carbide MEMS for harsh environments," *Proceedings of the IEEE,* vol. 86, pp. 1594-1610, Aug 1998.

[84] S. E. Saddow and A. Agrawal, "Chapter 1-Silicon carbide overview," in *Advances in Silicon Carbide Processing and Applications* S. Saddow and A. Agrawal, Eds., First ed Norwood, MA: Norwood: Artech House, 2004, pp. 7-18.

[85] C. W. Locke, A. Severino, F. La Via, M. Reyes, J. Register, and S. E. Saddow, "Chapter 2 - SiC Films and Coatings: Amorphous, Polycrystalline, and Single Crystal Forms," in *Silicon Carbide Biotechnology*, ed Oxford: Elsevier, 2012, pp. 17-61.

[86] J. M. Goddard and J. H. Hotchkiss, "Polymer surface modification for the attachment of bioactive compounds," *Progress in Polymer Science,* vol. 32, pp. 698-725, 2007.

[87] G. Beheim and L. Evans, "Materials for microelectromechanical systems," in *In MEMS: design and fabrication*, M. Gad-el-Hak, Ed., ed Boca Raton, FL: Taylor & Francis Group, 2006, pp. 5-7.

[88] C. Locke, C. Frewin, L. Abbati, and S. E. Saddow, "Demonstration of 3C-SiC MEMS Structures on Polysilicon-on-oxide Substrates," in *Materials Research Society Spring Meeting*, San Francisco, CA, 2010, pp. 1246-B08-05.

[89] N. Wright and A. Horsfall, "SiC sensors: a review," *Journal of Physics D: Applied Physics,* vol. 40, pp. 6345-54, 2007.

[90] G. L. Harris, "Basic physicial properties," in *Properties of silicon carbide*, G. L. Harris, Ed., ed United Kingdom: INSPEC, Institution of Electrical Engineers, 1995, p. 9.

[91] Y. Goldberg, M. Levinshtein, and S. Rumyantsev, "Silicon carbide (SiC)," in *Properties of Advanced Semiconductor Materials: GaN, AlN, InN, BN, SiC, SiGe*, M. Shur, M. Levinshtein, and S. Rumyantsev, Eds., ed New York, NY: John Wiley and Sons, 2001, pp. 93-147.

[92] X. Li, X. Wang, R. Bondokov, J. Morris, Y. H. An, and T. S. Sudarshan, "Micro/nanoscale mechanical and tribological characterization of SiC for orthopedic applications " *Journal of biomedical materials research. Part B, Applied biomaterials,* vol. 72, pp. 353-61, 2004.

[93] A. B. Sproul and M. A. Green, "Improved value for the silicon intrinsic carrier concentration from 275 to 375 K," *Journal of Applied Physics,* vol. 70, p. 846, 1991.

[94] T. Ayalew, "SiC Semiconductor Devices, Technology, Modeling, and Simulation " Doctor of technical sciences, Electrical and Computer Engineering, Vienna University of Technology, Austria, 2004.

[95] P. Godignon, "SiC Materials and Technologies for Sensors Development " *Materials Science Forum,* vol. 483-485, pp. 1009-14, 2005.

[96] C. Locke, R. Anzalone, A. Severino, C. Bongiorno, G. Litrico, F. La Via*, et al.*, "High Quality Single Crystal 3C-SiC(111) Films Grown on Si(111)," *Materials Science Forum,* vol. 615-617, pp. 145-148, 2009.

[97] U. Kalnins, A. Erglis, I. Dinne , I. Kumsars , and S. Jegerebce, "Clinical outcomes of silicon carbide coated stents in patients with coronary artery disease," *Med Sci Monit,* vol. 8, pp. PI16-20, 2002.

[98] M. Amon, A. Bolz, and M. Schaldach, "Improvement of stenting therapy with a silicon carbide coated tantalum stent," *Journal of Material Science: Materials in medicine,* vol. 7, pp. 273-278, 1996.

[99] C. Ozbek, A. Heisel, B. Gross, W. Bay, and H. Schieffer, "Coronary implantation of silicone-carbide-coated Palmaz-Schatz stents in patients with high risk of stent thrombosis without oral anticoagulation," *Catheterization and cardiovascular diagnosis,* vol. 41, pp. 71-78, May 1997.

[100] D. Carrié, K. Khalifé, M. Hamon, B. Citron, J. P. Monassier, R. Sabatier*, et al.*, "Initial and follow-up results of the Tenax coronary stent," *Journal of interventional cardiology* vol. 14, pp. 1-5, 2001.

[101] J. Fournier, J. Calabuig, A. Merchan, J. Augé, R. Melgares, T. Colman*, et al.*, "Initial results and 6 month clinical follow-up after implantation of a silicon carbide coated coronary stent," *Revista Española de Cardiología,* vol. 54, pp. 567-572, 2001.

[102] J. Will, A. Hoppe, F. A. Muller, C. T. Raya, J. M. Fernandez, and P. Greil, "Bioactivation of biomorphous silicon carbide bone implants," *Acta Biomater,* vol. 6, pp. 4488-94, Dec 2010.

[103] S. Santavirta, M. Takagi, L. Nordsletten, A. Anttila, R. Lappalainen, and Y. Konttinen, "Biocompatibility of silicon carbide in colony formation test in vitro," *Archives of Orthopedic Trauma Surgery,* vol. 118, pp. 89-91, 1998.

[104] M. Saki, M. Kazemzadeh Narbat, A. Samadikuchaksaraei, H. B. Ghafouri, and F. Gorjipour, "Biocompatibility Study of a Hydroxyapatite-Alumina and Silicon Carbide Composite Scaffold for Bone Tissue Engineering," *Yakhteh Medical Journal,* vol. 11, pp. 55-60, 2009.

[105] I. Svensson, E. Artursson, P. Leanderson, R. Berglind, and F. Lindgren, "Toxicity in vitro of some silicon carbides and silicon nitrides: whiskers and powders," *American journal of industrial medicine,* vol. 31, pp. 335-43, 1997.

[106] K. Rodelsperger and B. Bruckel, "The carcinogenicity of WHO fibers of silicon carbide: SiC whiskers compared to cleavage fragments of granular SiC," *Inhal Toxicol,* vol. 18, pp. 623-31, Aug 2006.

[107] J. M. Bluet, J. Botsoa, Y. Zakharko, A. Geloen, S. Alekseev, O. Marty*, et al.*, "Chapter 11 - SiC as a Biocompatible Marker for Cell Labeling," in *Silicon Carbide Biotechnology*, ed Oxford: Elsevier, 2012, pp. 377-429.

[108] C. L. Frewin, "The neuron-silicon carbide interface: biocompatibility study and BMI device development," PhD Dissertaion Electrical Engineering, University of South Florida, Tampa, FL, 2009.

[109] C. L. Frewin, C. Locke, S. E. Saddow, and E. J. Weeber, "Single-Crystal Cubic Silicon Carbide : An In Vivo Biocompatible Semiconductor for Brain Machine Interface Devices," in *33rd Annual International Conferen of the IEEE Engineering in Medicine and Biology Society*, Boston, MA, 2011, pp. 2957-60.

[110] N. Schettini, M. J. Jaroszeski, L. West, and S. E. Saddow, "Chapter 5 - Hemocompatibility Assessment of 3C-SiC for Cardiovascular Applications," in *Silicon Carbide Biotechnology*, ed Oxford: Elsevier, 2012, pp. 153-208.

[111] J. M. Anderson, "Chapter 4 Mechanisms of inflammation and infection with implanted devices," *Cardiovascular Pathology,* vol. 2, pp. 33-41, 1993.

[112] F. Nederberg, J. Watanabe, K. Ishihara, J. Hilborn, and T. Bowden, "Biocompatible and biodegradable phosphorylcholine ionomers with reduced protein adsorption and cell adhesion," *Journal of biomaterials science: Polymer edition,* vol. 17, pp. 605-614, 2006.

[113] S. Abraham, S. Brahim, K. Ishihara, and A. Guiseppi-Elie, "Molecularly engineered p(HEMA)-based hydrogels for implant biochip biocompatibility," *Biomaterials,* vol. 26, pp. 4767-78, 2005.

[114] A. N. Wilson and A. Guiseppi-Elie, "Bioresponsive Hydrogels," *Advanced Healthcare Materials,* pp. n/a-n/a, 2012.

[115] P. J. Barnes, "Inhaled Glucocorticoids for Asthma," *New England Journal of Medicine,* vol. 332, pp. 868-875, 1995.

[116] L. S. Goodman, L. L. Brunton, B. Chabner, B. œ. C. Knollmann, and L. S. Goodman, *Goodman & Gilman's The pharmacological basis of therapeutics*, 12th ed. New York: McGraw-Hill, 2011.

[117] W. K. Ward, M. J. Quinn, M. D. Wood, K. L. Tiekotter, S. Pidikiti, and J. A. Gallagher, "Vascularizing the tissue surrounding a model biosensor: how localized is the effect of a subcutaneous infusion of vascular endothelial growth factor (VEGF)?," *Biosensors and Bioelectronics,* vol. 19, pp. 155-163, 2003.

[118] G. Takagi, M. Miyamoto, S. Tara, I. Takagi, H. Takano, M. Yasutake*, et al.*, "Controlled-release basic fibroblast growth factor for peripheral artery disease: comparison with autologous bone marrow-derived stem cell transfer," *Tissue Eng Part A,* vol. 17, pp. 2787-94, 2011.

[119] B. D. Ratner, *Biomaterials science : an introduction to materials in medicine*, 2nd ed ed. San Diego ; London: Elsevier Academic Press, 2004.

[120] C. N. Kotanen, F. G. Moussy, S. Carrara, and A. Guiseppi-Elie, "Implantable enzyme amperometric biosensors," *Biosens Bioelectron,* vol. 35, pp. 14-26, 2012.

[121] P. Godignon, I. Maring, G. Gabriel, R. Gomez, M. Placidi, and R. Villa, "New generation of SiC biodevices implemented on 4 inch wafers," *Materials Science Forum,* vol. 645-648, pp. 1097-1100, 2010.

[122] C. A. Zorman, "Silicon Carbide as a Material for Biomedical Microsystems," in *Symposium on Design, Test, Integration & Packaging of MEMS/MOEMS* Rome, Italy, 2009.

[123] V. Chu, J. P. Conde, J. Jarego, P. Brogueira, J. Rodriguez, N. Barradas*, et al.*, "Transport and Photoluminescence of Hydrogenated Amorphous Silicon-Carbon Alloys," *Journal of Applied Physics,* vol. 78, pp. 3164-3173, Sep 1 1995.

[124] H. Pierson, *Handbook of Chemical Vapor Depostion*, 2nd ed. Norwich, NY: Noyes Publicatio, 1999.

[125] D. Hume and I. Kolthoff, "The Silicon Carbide Electrode " *Journal of american chemical society,* vol. 63, pp. 2805-6, 1941.

[126] F. Meier, D. M. Giolando, and J. R. Kirchhoff, "Silicon carbide: a new electrode material for voltammetric measurements " *Chemical Communications,* p. 2553, 1996.

[127] S. Singh and R. C. Buchanan, "SiC-C fiber electrode for biological sensing," *Materials Science & Engineering C-Biomimetic and Supramolecular Systems,* vol. 27, pp. 551-557, Apr 2007.

[128] W. C. Wu, H. W. Chang, and Y. C. Tsai, "Electrocatalytic detection of dopamine in the presence of ascorbic acid and uric acid at silicon carbide coated electrodes," *Chemical Communications,* vol. 47, pp. 6458-6460, 2011.

[129] A. Salimi, L. Mohamadi, R. Hallaj, and S. Soltanian, "Electrooxidation of insulin at silicon carbide nanoparticles modified glassy carbon electrode," *Electrochemistry Communications,* vol. 11, pp. 1116-1119, Jun 2009.

[130] H. A. Rafiee-Pour, A. Noorbakhsh, A. Salimi, and H. Ghourchian, "Sensitive Superoxide Biosensor Based on Silicon Carbide Nanoparticles," *Electroanalysis,* vol. 22, pp. 1599-1606, Jul 2010.

[131] R. Ghavami, A. Salimi, and A. Navaee, "SiC nanoparticles-modified glassy carbon electrodes for simultaneous determination of purine and pyrimidine DNA bases," *Biosensors and Bioelectronics,* vol. 26, pp. 3864-3869, 2011.

[132] N. Yang, H. Zhuang, R. Hoffmann, W. Smirnov, J. Hees, X. Jiang*, et al.*, "Nanocrystalline 3C-SiC electrode for biosensing applications," *Analytical Chemistry,* vol. 83, pp. 5827-30, Aug 1 2011.

[133] J. Pascual, F. Valvo, P. Godignon, J. Aguilo, J. Millan, J. Camassel*, et al.*, "SiC base micro-probe for myocardial ischemia monitoring," *Silicon Carbide and Related Materials 2003, Prts 1 and 2,* vol. 457-460, pp. 1483-1486, 2004.

[134] R. Gomez, A. Ivorra, R. Villa, P. Godignon, J. Millan, I. Erill*, et al.*, "A SiC microdevice for the minimally invasive monitoring of ischemia in living tissues," *Biomed Microdevices,* vol. 8, pp. 43-49, Mar 2006.

[135] D. M. Brown, J. Kretchmer, J. Fedison, and T. Dean, "The commercialization of the SiC flame sensor," in *Electrochemical Society Proceedings*, 2002.

[136] SenSiCAB. (2012, December 15). *Sensors for cleaner air*.

[137] A. Lloyd Spetz, R. Pearce, L. Hedin, V. Khranovskyy, and F. Söderlind, "New transducer material concepts for biosensors and surface functionalization " in *SPIE, The International Society for Optical Engineering*, 2009, pp. 7362-06.

[138] J. Botsoa, V. Lysenko, A. Géloën, O. Marty, J. M. Bluet, and G. Guillot, "Application of 3C-SiC quantum dots for living cell imaging," *Applied Physics Letters,* vol. 92, p. 173902, 2008.

[139] D. Caputo, G. de Cesare, A. Nascetti, and R. Scipinotti, "Two-Color Sensor for Biomolecule Detection," *Sensor Letters,* vol. 6, pp. 542-547, Aug 2008.

[140] T. Taubner, D. Korobkin, Y. Urzhumov, G. Shvets, and R. Hillenbrand, "Near-field microscopy through a SiC superlens," *Science,* vol. 313, pp. 1595-1595, Sep 15 2006.

[141] G. Pandraud, P. J. French, and P. M. Sarro, "Fabrication and characteristics of a PECVD SiC evanescent wave optical sensor," *Sensors and Actuators a-Physical,* vol. 142, pp. 61-66, Mar 10 2008.

[142] C. A. Zorman and R. J. Parro, "Micro- and nanomechanical structures for silicon carbide MEMS and NEMS," *physica status solidi (b),* vol. 245, pp. 1404-1424, 2008.

[143] C. Iliescu, D. P. Poenar, M. Carp, and F. C. Loe, "A microfluidic device for impedance spectroscopy analysis of biological samples," *Sensors and Actuators B: Chemical,* vol. 123, pp. 168-176, 2007.

[144] C. Iliescu, B. Chen, D. P. Poenar, and Y. Y. Lee, "PECVD amorphous silicon carbide membranes for cell culturing," *Sensors and Actuators B: Chemical,* vol. 129, pp. 404-411, 2008.

[145] R. Memming, "Principles of Semiconductor Physics," in *Semiconductor Electrochemistry*, ed: Wiley-VCH Verlag GmbH, 2007, pp. 1-21.

[146] A. W. Bott, "Electrochemistry of Semiconductors," *Current separations.com and Drug development,* vol. 17, p. 5, 1998.

[147] R. Memming, "Electrochemical Systems," in *Semiconductor Electrochemistry*, ed: Wiley-VCH Verlag GmbH, 2007, pp. 46-60.

[148] I. Tiginyanu, S. Langa, H. Foell, and v. Ursachi, "Porous III-V Semiconductors ", ed, 2009.

[149] S. R. Morrison, *Electrochemistry at semiconductor and oxidized metal electrodes*: Plenum Press, 1980.

[150] R. Memming, "Solid-Liquid Interface," in *Semiconductor Electrochemistry*, ed: Wiley-VCH Verlag GmbH, 2007, pp. 81-111.

[151] K. Rajeshwar, "Fundamentals of Semiconductor Electrochemistry and Photoelectrochemistry," in *Encyclopedia of Electrochemistry*. vol. 6, S. Licht, Ed., ed: Wiley-VCH Verlag GmbH & Co. KGaA, 2007, pp. 1-45.

[152] D. K. Schroder, *Semiconductor Material and Device Characterization*: Wiley, 2006.

[153] N. Sato, *Electrochemistry at metal and semiconductor electrodes*. Amsterdam ; New York: Elsevier, 1998.

[154] R. De Gryse, W. P. Gomes, F. Cardon, and J. Vennik, "On the Interpretation of Mott-Schottky Plots Determined at Semiconductor/Electrolyte Systems," *Journal of The Electrochemical Society,* vol. 122, pp. 711-712, January 1, 1975 1975.

[155] J. A. Turner, "Energetics of the semiconductor-electrolyte interface," *Journal of Chemical Education,* vol. 60, pp. 327-329, 1983.

[156] Y. B. Wang, R. K. Yuan, and M. Willander, "Capacitance of semiconductor-electrolyte junction and its frequency dependence," *Applied Physics A,* vol. 63, pp. 481-486, 1996/11/01 1996.

[157] G. Nogami, "Characterization of Semiconductor Electrodes with a Deep Impurity Level," *Journal of The Electrochemical Society,* vol. 129, pp. 2219-2223, January 1, 1982 1982.

[158] K. Uosaki and H. Kita, "Effects of the Helmholtz Layer Capacitance on the Potential Distribution at Semiconductor/Electrolyte Interface and the Linearity of the Mott-Schottky Plot," *Journal of The Electrochemical Society,* vol. 130, pp. 895-897, January 1, 1983 1983.

[159] A. J. Nozik and R. Memming, "Physical Chemistry of Semiconductor−Liquid Interfaces," *The Journal of Physical Chemistry,* vol. 100, pp. 13061-13078, 1996/01/01 1996.

[160] J. H. Kennedy and K. W. Frese, "Flatband Potentials and Donor Densities of Polycrystalline α - Fe2 O 3 Determined from Mott-Schottky Plots," *Journal of The Electrochemical Society,* vol. 125, pp. 723-726, January 1, 1978 1978.

[161] A. Oliveros, C. L. Frewin, S. J. Schoell, M. Hoeb, M. Stutzmann, I. D. Sharp*, et al.*, "Assessment of cell proliferation on 6H-SiC bio-functionalized with self-assembled monolayers," *Journal of Materials Research,* vol. 28, pp. 78-86, 2013.

[162] A. Oliveros, A. Guiseppi-Elie, M. Jaroszeski, and S. E. Saddow, "Characterization of 3C-SiC (100) as a platform for detecting the onset of acute myocardial infarction (AMI)," *MRS Online Proceedings Library,* vol. 1433, pp. null-null, 2012.

[163] A. Oliveros, A. Guiseppi-Elie, M. Jaroszeski, and S. E. Saddow, "Protein immobilization on 3C-SiC (100) as a substrate for detecting the onset of acute myocardial infarction (AMI)," in *Engineering in Medicine and Biology Society (EMBC), 2012 Annual International Conference of the IEEE*, 2012, pp. 1643-1646.

[164] A. Oliveros, S. J. Schoell, C. Frewin, M. Hoeb, M. Stutzmann, I. D. Sharp*, et al.*, "Biocompatibility Assessment of SiC Surfaces After Functionalization with Self Assembled Organic Monolayers," *MRS Online Proceedings Library,* vol. 1235, pp. null-null, 2009.

[165] S. J. Schoell, A. Oliveros, M. Steenackers, S. E. Saddow, and I. D. Sharp, "Chapter 3 - Multifunctional SiC Surfaces: From Passivation to Biofunctionalization," in *Silicon Carbide Biotechnology*, ed Oxford: Elsevier, 2012, pp. 63-117.

[166] S. Brahim, A. M. Wilson, D. Narinesingh, E. Iwuoha, and A. Guiseppi-Elie, "Chemical and biological sensors based on electrochemical detection using conducting electroactive polymers," *Microchimica Acta,* vol. 143, pp. 123-137, Dec 2003.

[167] M. Stutzmann, J. A. Garrido, M. Eickhoff, and M. S. Brandt, "Direct biofunctionalization of semiconductors: A survey," *Physica Status Solidi a-Applications and Materials Science,* vol. 203, pp. 3424-3437, Nov 2006.

[168] A. Catellani and G. Cicero, "Modifications of cubic SiC surfaces studied by ab initio simulations: from gas adsorption to organic functionalization," *Journal of Physics D: Applied Physics,* vol. 40, p. 6215, 2007.

[169] C. Vahlberg, G. R. Yazdi, R. M. Petoral, M. Syvajarvi, K. Uvdal, a. L. Spetz*, et al.*, "Surface Engineering of Functional Materials for Biosensors," *IEEE Sensors, 2005.,* pp. 504-507, 2005.

[170] M. R. Linford, P. Fenter, P. M. Eisenberger, and C. E. D. Chidsey, "Alkyl Monolayers on Silicon Prepared from 1-Alkenes and Hydrogen-Terminated Silicon," *Journal of the American Chemical Society,* vol. 117, pp. 3145-3155, 1995/03/01 1995.

[171] K. Bierbaum, M. Kinzler, C. Woell, M. Grunze, G. Haehner, S. Heid*, et al.*, "A Near Edge X-ray Absorption Fine Structure Spectroscopy and X-ray Photoelectron Spectroscopy Study of the Film Properties of Self-Assembled Monolayers of Organosilanes on Oxidized Si(100)," *Langmuir,* vol. 11, pp. 512-518, 1995.

[172] N. Faucheux, R. Schweiss, K. Lützow, C. Werner, and T. Groth, "Self-assembled monolayers with different terminating groups as model substrates for cell adhesion studies," *Biomaterials,* vol. 25, pp. 2721-30, 2004.

[173] M. Rosso, A. Arafat, K. Schroen, M. Giesbers, C. S. Roper, R. Maboudian*, et al.*, "Covalent attachment of organic monolayers to silicon carbide surfaces," *Langmuir,* vol. 24, pp. 4007-4012, Apr 15 2008.

[174] M. Rosso, M. Giesbers, A. Arafat, K. Schroen, and H. Zuilhof, "Covalently Attached Organic Monolayers on SiC and SixN4 Surfaces: Formation Using UV Light at Room Temperature," *Langmuir,* vol. 25, pp. 2172-2180, Feb 17 2009.

[175] G. Cicero and A. Catellani, "Towards SiC surface functionalization: An ab initio study," *Journal of Chemical Physics,* vol. 122, Jun 1 2005.

[176] S. J. Schoell, M. Hoeb, I. D. Sharp, W. Steins, M. Eickhoff, M. Stutzmann*, et al.*, "Functionalization of 6H-SiC surfaces with organosilanes," *Applied Physics Letters,* vol. 92, Apr 14 2008.

[177] H. Tsuchida, I. Kamata, and K. Izumi, "Infrared attenuated total reflection spectroscopy of 6H–SiC (0001)" *Journal of Applied Physics,* vol. 85, pp. 3570-3574, 1999.

[178] S. J. Schoell, J. Howgate, M. Hoeb, M. Auernhammer, J. A. Garrido, M. Stutzmann*, et al.*, "Electrical passivation and chemical functionalization of SiC surfaces by chlorine termination," *Applied Physics Letters,* vol. 98, May 2011.

[179] J. Howgate, S. J. Schoell, M. Hoeb, W. Steins, B. Baur, S. Hertrich*, et al.*, "Photocatalytic Cleavage of Self-Assembled Organic Monolayers by UV-Induced Charge Transfer from GaN Substrates," *Advanced Materials,* vol. 22, pp. 2632-+, Jun 25 2010.

[180] N. Aghdassi, D. Dulson, S. Linden, L. Q. Li, L. F. Chi, and H. Zacharias, "Very large-bandgap insulating monolayers of ODS on SiC," *Applied Surface Science,* vol. 258, pp. 7280-7285, Jul 15 2012.

[181] J. Wong, A. Chilkoti, and V. T. Moy, "Direct force measurements of the streptavidin–biotin interaction," *Biomolecular Engineering,* vol. 16, pp. 45-55, 1999.

[182] E. H. Williams, A. V. Davydov, A. Motayed, S. G. Sundaresan, P. Bocchini, L. J. Richter*, et al.*, "Immobilization of streptavidin on 4H-SiC for biosensor development," *Applied Surface Science,* vol. 258, pp. 6056-6063, Jun 1 2012.

[183] R. M. Petoral, G. R. Yazdi, A. L. Spetz, R. Yakimova, and K. Uvdal, "Organosilane-functionalized wide band gap semiconductor surfaces," *Applied Physics Letters,* vol. 90, May 28 2007.

[184] D. K. Bhowmick, S. Linden, A. Devaux, L. De Cola, and H. Zacharias, "Functionalization of Amorphous SiO2 and 6H-SiC(0001) Surfaces with Benzo[ghi]perylene-1,2-dicarboxylic Anhydride via an APTES Linker," *Small,* vol. 8, pp. 592-601, Feb 20 2012.

[185] G. Qin, R. Zhang, B. Makarenko, A. Kumar, W. Rabalais, J. M. Lopez Romero*, et al.*, "Highly stable, protein resistant thin films on SiC-modified silicon substrates," *Chemical Communications,* vol. 46, pp. 3289-3291, 2010.

[186] C. L. Frewin, C. Coletti, C. Riedl, U. Starke, and S. E. Saddow, "A Comprehensive Study of Hydrogen Etching on the Major SiC Polytypes and Crystal Orientations," *Materials Science Forum,* pp. 615-617, 2009.

[187] C. Coletti, C. L. Frewin, S. E. Saddow, M. Hetzel, C. Virojanadara, and U. Starke, "Surface studies of hydrogen etched 3C-SiC(001) on Si(001)," *Applied Physics Letters,* vol. 91, Aug 6 2007.

[188] I. D. Sharp, S. J. Schoell, M. Hoeb, M. S. Brandt, and M. Stutzmann, "Electronic properties of self-assembled alkyl monolayers on Ge surfaces," *Applied Physics Letters,* vol. 92, Jun 2 2008.

[189] S. P. Low, K. Williams, L. T. Canham, and N. H. Voelcker, "Evaluation of mammalian cell adhesion on surface-modified porous silicon," *Biomaterials,* vol. 27, pp. 4538-46, 2006.

[190] M. Reyes, Y. Shishkin, S. Harvey, and S. E. Saddow, "Development of a high growth rate 3C-SiC on Si CVD process," 2006, pp. 79-84.

[191] S. J. Schoell, M. Sachsenhauser, A. Oliveros, J. Howgate, M. Stutzmann, M. S. Brandt*, et al.*, "Organic Functionalization of 3C-SiC Surfaces," *ACS Applied Materials & Interfaces,* vol. 5, pp. 1393-1399, 2013/02/27 2013.

[192] B. Baur, G. Steinhoff, J. Hernando, O. Purrucker, M. Tanaka, B. Nickel*, et al.*, "Chemical functionalization of GaN and AlN surfaces," *Applied Physics Letters,* vol. 87, pp. 263901-263901, 2005.

[193] W. Qian, D. Yao, F. Yu, B. Xu, R. Zhou, X. Bao*, et al.*, "Immobilization of antibodies on ultraflat polystyrene surfaces," *Clin Chem,* vol. 46, pp. 1456-63, Sep 2000.

[194] L. Yang and Y. Li, "AFM and impedance spectroscopy characterization of the immobilization of antibodies on indium-tin oxide electrode through self-assembled monolayer of epoxysilane and their capture of Escherichia coli O157:H7," *Biosens Bioelectron,* vol. 20, pp. 1407-16, Jan 15 2005.

[195] J. C. Ehrhart, B. Bennetau, L. Renaud, J. P. Madrange, L. Thomas, J. Morisot*, et al.*, "A new immunosensor for breast cancer cell detection using antibody-coated long alkylsilane self-assembled monolayers in a parallel plate flow chamber," *Biosens Bioelectron,* vol. 24, pp. 467-74, Nov 15 2008.

[196] N. A. Lapin and Y. J. Chabal, "Infrared Characterization of Biotinylated Silicon Oxide Surfaces, Surface Stability, and Specific Attachment of Streptavidin," *The Journal of Physical Chemistry B,* vol. 113, pp. 8776-8783, 2009/06/25 2009.

[197] B. S. Kang, F. Ren, L. Wang, C. Lofton, W. W. Tan, S. J. Pearton*, et al.*, "Electrical detection of immobilized proteins with ungated <equation>AlGaN/GaN</equation> high-electron-mobility Transistors," *Applied Physics Letters,* vol. 87, pp. 023508-023508-3, 2005.

[198] Z.-H. Wang and G. Jin, "Covalent immobilization of proteins for the biosensor based on imaging ellipsometry," *Journal of Immunological Methods,* vol. 285, pp. 237-243, 2/15/ 2004.

[199] D. Huber, J. Rudolf, P. Ansari, B. Galler, M. Fuhrer, C. Hasenhindl*, et al.*, "Effectiveness of natural and synthetic blocking reagents and their application for detecting food allergens in enzyme-linked immunosorbent assays," *Anal Bioanal Chem,* vol. 394, pp. 539-48, May 2009.

[200] Thermo-Scientific. (July 25th). *Protocol - EDC and Sulfo-NHS*. Available: http://www.piercenet.com/objects/view.cfm?type=page&ID=C0B555CC-0F33-4818-B09D-031E7FCF89FC

[201] G. T. Hermanson, "Chapter 5 - Heterobifunctional Crosslinkers," in *Bioconjugate Techniques (Second Edition)*, ed New York: Academic Press, 2008, pp. 276-335.

[202] D. Maraldo and R. Mutharasan, "Optimization of antibody immobilization for sensing using piezoelectrically excited-millimeter-sized cantilever (PEMC) sensors," *Sensors and Actuators B: Chemical,* vol. 123, pp. 474-479, 4/10/ 2007.

[203] E. H. Williams, A. V. Davydov, A. Motayed, S. G. Sundaresan, P. Bocchini, L. J. Richter*, et al.*, "Immobilization of streptavidin on 4H–SiC for biosensor development," *Applied Surface Science,* vol. 258, pp. 6056-6063, 2012.

[204] C. Seokheun and C. Junseok, "Methods of reducing non-specific adsorption in microfluidic biosensors," *Journal of Micromechanics and Microengineering,* vol. 20, p. 075015, 2010.

[205] Q. A. Bhatti, G. J. Moran, and C. C. Matthai, "Computer Simulation of Surface Diffusion of Silicon and Carbon Adatoms on SiC(001)," *MRS Online Proceedings Library,* vol. 423, pp. null-null, 1996.

[206] A. Sagues, J. T. Wolan, A. De Fex, and T. Fawcett, "Impedance behavior of nanoporous SiC," *Electrochimica Acta,* vol. 51, pp. 1656–1663, 2006.

[207] L. Wu, F. Camacho-Alanis, H. Castaneda, G. Zangari, and N. Swami, "Electrochemical impedance spectroscopy of carboxylic-acid terminal alkanethiol self assembled monolayers on GaAs substrates," *Electrochimica Acta,* vol. 55, pp. 8758-8765, 12/1/ 2010.

[208] L. Olitzki, "Electric Charge of Antibodies," *The Journal of Immunology,* vol. 24, pp. 505-512, June 1, 1933 1933.

[209] Y. Cheng, P. Xiong, C. S. Yun, G. F. Strouse, J. P. Zheng, R. S. Yang*, et al.*, "Mechanism and optimization of pH sensing using SnO2 nanobelt field effect transistors," *Nano Lett,* vol. 8, pp. 4179-84, Dec 2008.

[210] Y. Thiansilakul, S. Benjakul, and M. P. Richards, "Isolation, characterisation and stability of myoglobin from Eastern little tuna (Euthynnus affinis) dark muscle," *Food Chemistry,* vol. 124, pp. 254-261, 1/1/ 2011.

[211] G. Gros, H. S. Rollema, W. Jelkmann, H. Gros, C. Bauer, and W. Moll, "Net charge and oxygen affinity of human hemoglobin are independent of hemoglobin concentration," *J Gen Physiol,* vol. 72, pp. 765-773, 12/01 1978.

[212] A. Belaïdi, J. N. Chazalviel, F. Ozanam, O. Gorochov, A. Chari, B. Fotouhi*, et al.*, "Silicon surface states and subsurface hydrogen," *Journal of Electroanalytical Chemistry,* vol. 444, pp. 55-60, 3/5/ 1998.

[213] H.-Z. Yu, S. Morin, D. D. M. Wayner, P. Allongue, and C. Henry de Villeneuve, "Molecularly Tunable “Organic Capacitors” at Silicon/Aqueous Electrolyte Interfaces1," *The Journal of Physical Chemistry B,* vol. 104, pp. 11157-11161, 2000/11/01 2000.

[214] H. Einati, A. Mottel, A. Inberg, and Y. Shacham-Diamand, "Electrochemical studies of self-assembled monolayers using impedance spectroscopy," *Electrochimica Acta,* vol. 54, pp. 6063-6069, 10/30/ 2009.

[215] W. Yang, J. E. Butler, J. J. N. Russell, and R. J. Hamers, "Direct electrical detection of antigen-antibody binding on diamond and silicon substrates using electrical impedance spectroscopy," *Analyst,* vol. 132, pp. 296-306, 2007.

[216] P. Allongue, C. Henry de Villeneuve, and J. Pinson, "Structural characterization of organic monolayers on Si 〈111〉 from capacitance measurements," *Electrochimica Acta,* vol. 45, pp. 3241-3248, 6/23/ 2000.

[217] P. Allongue, C. H. D. Villeneuve, and P. Vi, "Molecularly Tunable “Organic Capacitors” at Silicon/Aqueous Electrolyte Interfaces 1," *Society,* pp. 11157-11161, 2000.

[218] E. J. Faber, "TOWARDS THE HYBRID ORGANIC SEMICONDUCTOR FET (HOSFET) – Electrical and Electrochemical Characterization of Functionalized and Unfunctionalized, Covalently Bound Organic Monolayers on Silicon Surfaces," MESA Research Institute at the University of Twente, University of Twente, Enschede, Netherlands, 2006.

[219] I. Lauermann, R. Memming, and D. Meissner, "Electrochemical Properties of Silicon Carbide," *Journal of the Electrochemical Society,* vol. 144, pp. 73-80, 1997.

[220] J. A. Turner and B. A. Parkinson, "The application of chronocoulometry to the study of adsorption at the semiconductor/electrolyte interface," *Journal of Electroanalytical Chemistry and Interfacial Electrochemistry,* vol. 150, pp. 611-617, 7/25/ 1983.

[221] E. Metwalli, D. Haines, O. Becker, S. Conzone, and C. G. Pantano, "Surface characterizations of mono-, di-, and tri-aminosilane treated glass substrates," *Journal of colloid and interface science,* vol. 298, pp. 825-31, 2006.

[222] R. G. Acres, A. V. Ellis, J. Alvino, C. E. Lenahan, D. A. Khodakov, G. F. Metha*, et al.*, "Molecular Structure of 3-Aminopropyltriethoxysilane Layers Formed on Silanol-Terminated Silicon Surfaces," *The Journal of Physical Chemistry C,* vol. 116, pp. 6289-6297, 2012/03/15 2012.

[223] P. Bataillard, F. Gardies, N. Jaffrezic-Renault, C. Martelet, B. Colin, and B. Mandrand, "Direct detection of immunospecies by capacitance measurements," *Anal Chem,* vol. 60, pp. 2374-9, Nov 1 1988.

[224] L. Corash, "Measurement of platelet activation by fluorescence-activated flow cytometry," *Blood Cells,* vol. 16, pp. 97-106; discussion 107-8, 1990.

[225] A. H. Lazarus, J. F. Wright, V. Blanchette, and J. Freedman, "Analysis of platelets by flow cytometry," *Transfusion Science,* vol. 16, pp. 353-361, 12// 1995.

[226] M. Steenackers, I. D. Sharp, K. Larsson, N. a. Hutter, M. Stutzmann, and R. Jordan, "Structured Polymer Brushes on Silicon Carbide," *Chemistry of Materials,* vol. 22, pp. 272-278, 2010.

[227] C. N. Kotanen, C. Tlili, and A. Guiseppi-Elie, "Amperometric glucose biosensor based on electroconductive hydrogels," *Talanta,* vol. 103, pp. 228-235, 1/15/ 2013.

[228] E. Souteyrand, J. R. Martin, and C. Martelet, "Direct detection of biomolecules by electrochemical impedance measurements," *Sensors and Actuators B: Chemical,* vol. 20, pp. 63-69, 1994.

[229] A. Carré, W. Birch, and V. Lacarrière, "Glass Substrates Modified With Organosilanes For DNA Immobilization," in *Silanes and other coupling agents* vol. 4, ed: Brill, 2007, pp. 113-126.

APPENDICES

Appendix A Calculation of the Expected Capacitance of the SiC Space Charge Region

In this appendix we include some calculations and fitting of the results obtained experimentally from the electrochemical impedance and Mott-Schottky plots from Chapter 4.

A.1 Capacitance of SiC After OH Termination

Assuming a depletion width of 0.094 μm and N_d 3.64x 10^{18} cm^{-3} from the Hg probe measurements we obtain the capacitance of the SiC space charge region using equation (13).

$$C_{SiC} = \frac{\varepsilon\varepsilon_o}{d} = \frac{9.7x8.85x10^{-14}}{0.094x10^{-4}} = 93.4\,\frac{nF}{cm^2} \tag{13}$$

A.2 Capacitance of SiC After APTES Surface Modification

In order to calculate the capacitance of the SiC|APTES surfaces, we assume that the net charge of the APTES layer induces a depletion width in the semiconductor. Carre *et al.* [229] proposed that APTES films have a density of ~ 1.2 amine groups/nm^2.

If we assume Q = q/nm^2 (q = 1.6x10^{-19} C), we have:

$$Q = q * d * N_d. \tag{14}$$

$$\frac{10^{14}q}{cm^2} = q * d * N_d \tag{15}$$

$$d = 0.00002\,cm = 200\,nm \tag{16}$$

Using equation (12) we calculate $C_{SiC} = 43\,nF/cm^2$ after APTES functionalization.

A.3 Fit of the Experimental Data

Using expressions for the total capacitance in depletion and accumulation we fit the CV data obtained for bare SiC and APTES modified SiC presented in section 4.6.3.

A.4 Fitting of the CV Results for the SiC After OH Termination

Using the values obtained from extrapolating the Mott-Schottky plots presented in Figure 50 and Table 9, i.e. E_{fb} = -550 mV and N_d = 7.28x10^{18} cm^{-3}. We consider that in accumulation there is a voltage drop both in the SCR and the Helmholtz capacitance, C_H and that the charge in the SCR (Q_{SiC}) is the same as in the Helmholtz layer, see (17). we used the calculated capacitance in accumulation and depletion expressed in equations (18) to (20) to fit the experimental data as shown in Figure 53. In this case we assumed a C_H= 5 μF/cm^2 in series with the SiC's SCR capacitance.

In accumulation:

$$E - E_{fb} = V_{SiC} + V_{C_H} = \frac{Q_{SiC}}{C_{SiC}} - \frac{Q_{SiC}}{C_H} \tag{17}$$

$$Q_{SiC} = \sqrt{2\varepsilon\varepsilon_o kTN_d} e^{-\frac{qV_{SiC}}{2kT}} \tag{18}$$

$$C_{SiC} = \sqrt{\frac{q^2\varepsilon\varepsilon_o N_d}{2kT}} e^{-\frac{qV_{SiC}}{2kT}} \tag{19}$$

$$\frac{1}{C_T} = \frac{1}{C_{SiC}} + \frac{1}{C_H} \tag{20}$$

In depletion:

$$C_{SiC} = \sqrt{\frac{q\varepsilon\varepsilon_o N_d}{2(E-E_{fb}-\frac{kT}{q})}} \tag{21}$$

$$\frac{1}{C_T} = \frac{1}{C_{SiC}} \tag{22}$$

As seen in Figure A. 1 the best fitting is achieved including the Helmholtz capacitance (C_H) in accumulation and a difference of the calculated and experimental data is observed between -200 and 200 mV probably due to the presence of surface states or defects that were not considered in the simulated CV data.

Appendix A (Continued)

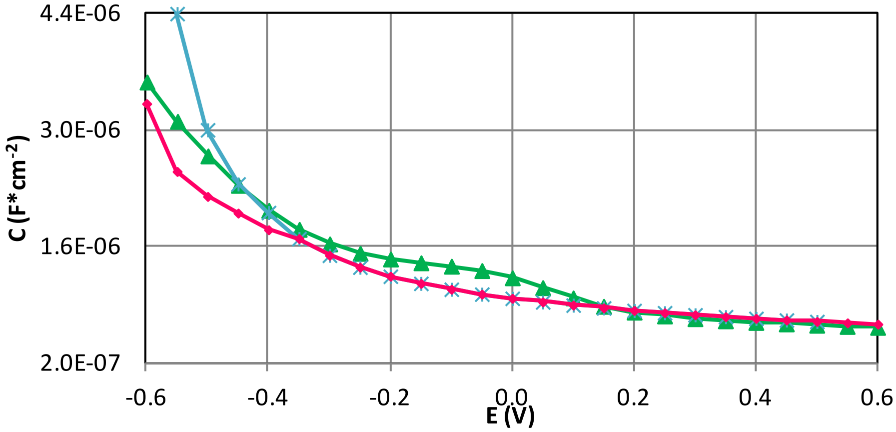

Figure A.1 Experimental and fitted CV data for SiC. Experimental bare SiC ▲ without C_H in accumulation ✳ Including the C_H= 5 μF/cm^2 in accumulation ◆ .

A.5 Fitting of the CV Results for the SiC After APTES Surface Functionalization

Similarly to the calculations performed for the simulated CV data for the bare SiC, we consider equations (17) to (19) for the total capacitance in accumulation and depletion. However, equation (20) is modified as shown in (23) since we include the effect of the APTES capacitance in series to the C_H in accumulation. We assume a value of C_{APTES}= 4.4 uF/cm^2 that gives an approximate thickness of the APTES film of 5 Å lower than the 10 Å calculated via XPS by Schoell *et al.* [191].

In accumulation:

$$\frac{1}{C_T} = \frac{1}{C_{SiC}} + \frac{C_H + C_{APTES}}{C_H * C_{APTES}} \tag{23}$$

We see in Figure A. 2 that the fitted data closely fits the experimental data but assuming C_H higher than for the bare SiC simulated data. The experimental data shows no "bumps" or indications of surface states probably due to the insulating effect of the APTES films.

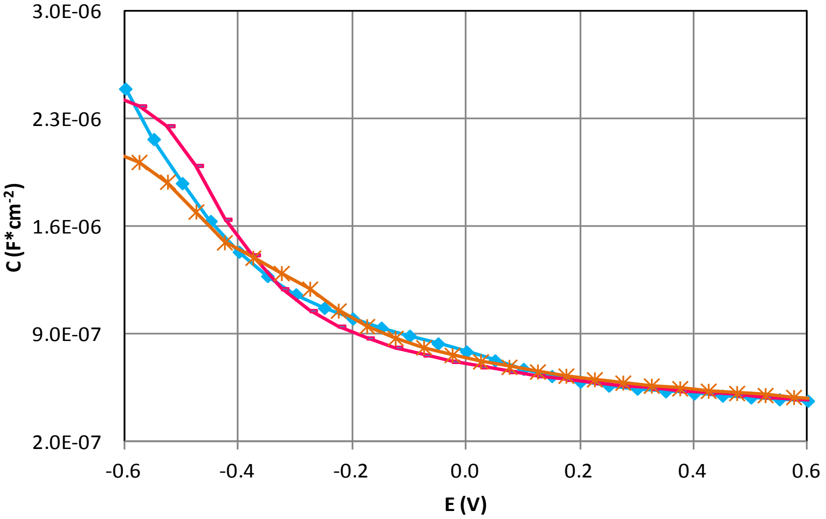

Figure A.2 Experimental and fitted CV data for APTES coated SiC. —◆— Experimental APTES|SiC — Including C_{APTES} = 4.4 μF/cm^2 and C_H= 7 μF/cm^2 in accumulation —✳— Including C_{APTES} = 4.4 μF/cm^2 and C_H= 5 μF/cm^2 in accumulation.

Appendix B Permission for Reproduction of Materials

In the figure below is the permission from IEEE to use the material from [163] including in Chapter 3, section 3.4 to 3.4.3.1, Figure 21, Figure 22, Figure 22 and Figure 24.

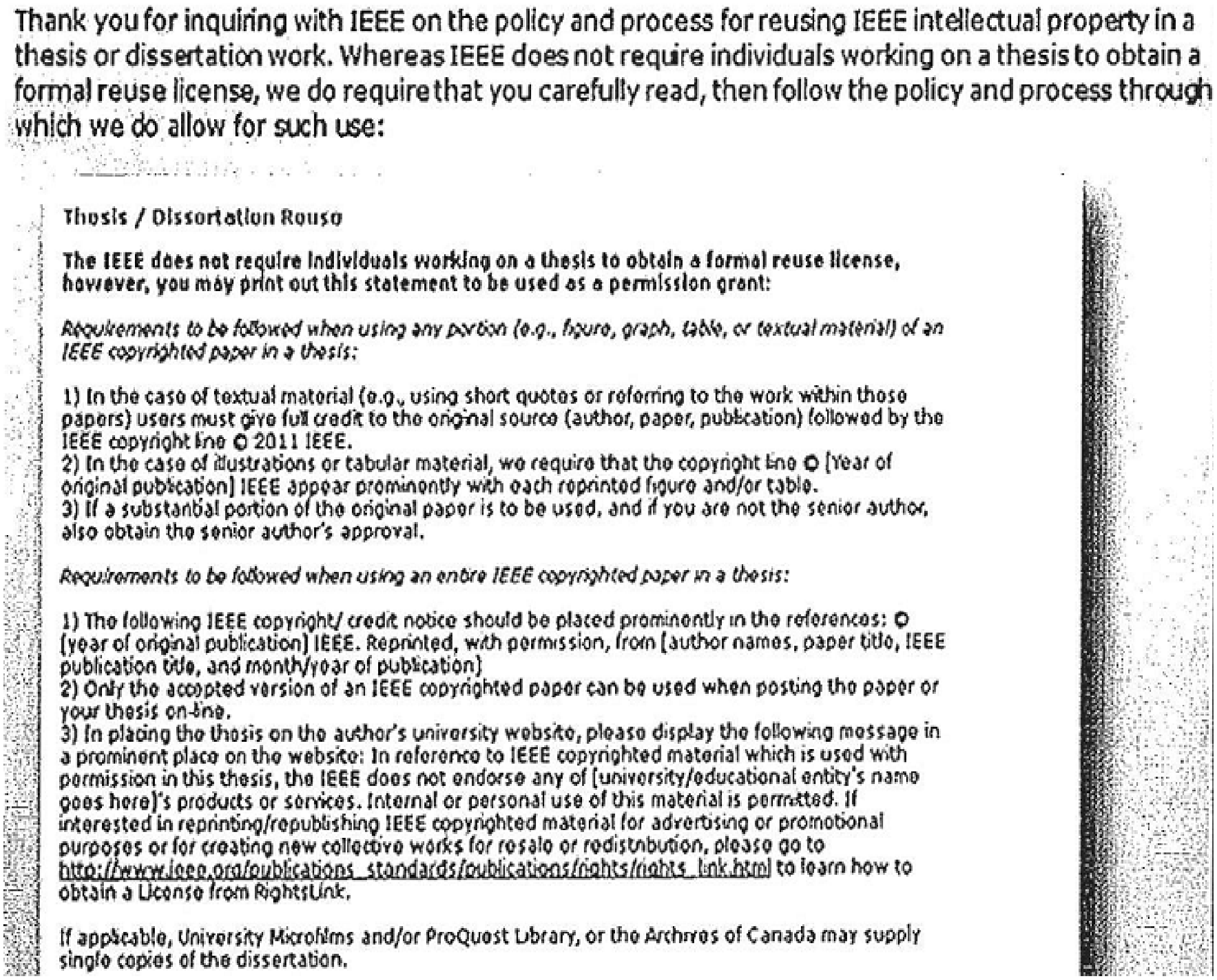

Thank you for inquiring with IEEE on the policy and process for reusing IEEE intellectual property in a thesis or dissertation work. Whereas IEEE does not require individuals working on a thesis to obtain a formal reuse license, we do require that you carefully read, then follow the policy and process through which we do allow for such use:

Thesis / Dissertation Reuse

The IEEE does not require individuals working on a thesis to obtain a formal reuse license, however, you may print out this statement to be used as a permission grant:

Requirements to be followed when using any portion (e.g., figure, graph, table, or textual material) of an IEEE copyrighted paper in a thesis:

1) In the case of textual material (e.g., using short quotes or referring to the work within those papers) users must give full credit to the original source (author, paper, publication) followed by the IEEE copyright line © 2011 IEEE.
2) In the case of illustrations or tabular material, we require that the copyright line © [Year of original publication] IEEE appear prominently with each reprinted figure and/or table.
3) If a substantial portion of the original paper is to be used, and if you are not the senior author, also obtain the senior author's approval.

Requirements to be followed when using an entire IEEE copyrighted paper in a thesis:

1) The following IEEE copyright/ credit notice should be placed prominently in the references: © [year of original publication] IEEE. Reprinted, with permission, from [author names, paper title, IEEE publication title, and month/year of publication]
2) Only the accepted version of an IEEE copyrighted paper can be used when posting the paper or your thesis on-line.
3) In placing the thesis on the author's university website, please display the following message in a prominent place on the website: In reference to IEEE copyrighted material which is used with permission in this thesis, the IEEE does not endorse any of [university/educational entity's name goes here]'s products or services. Internal or personal use of this material is permitted. If interested in reprinting/republishing IEEE copyrighted material for advertising or promotional purposes or for creating new collective works for resale or redistribution, please go to http://www.ieee.org/publications_standards/publications/rights/rights_link.html to learn how to obtain a License from RightsLink.

If applicable, University Microfilms and/or ProQuest Library, or the Archives of Canada may supply single copies of the dissertation.

Figure B.1 IEEE policy for using IEEE intellectual property in a thesis or dissertation work.

Appendix B (Continued)

Below is the permission from Cambridge University Press to reproduce material from [161] in Chapter 3, including sections 3.2 to 3.3.2.4, Figure 17 and Figure 18 and Table 2, in addition to excerpts from [164] and [165] in sections 3.2 to 3.3.2.4 and excerpts of [162] in section 3.4 and 3.4.3.1 and modifications of Figure 21 and Figure 22.

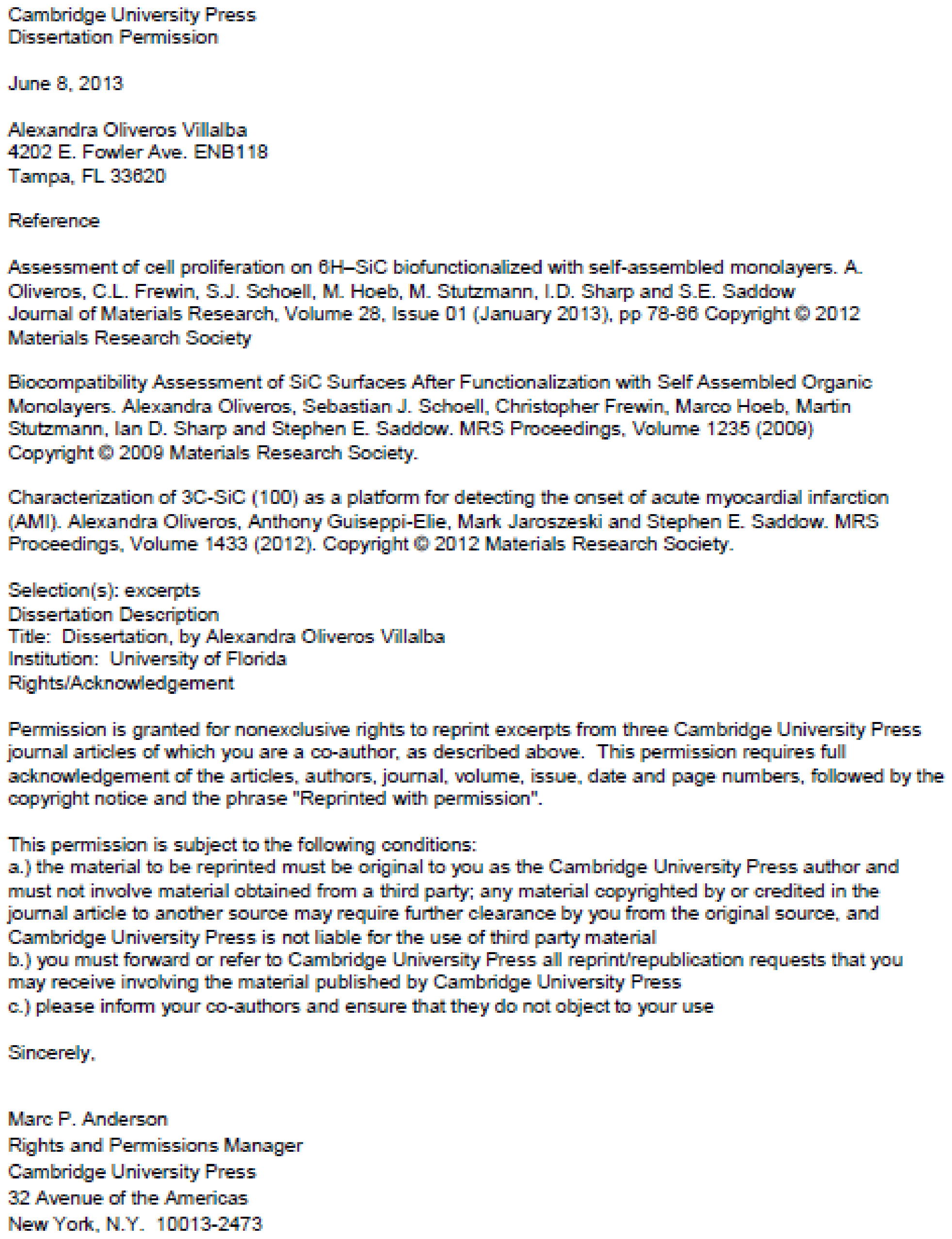

Cambridge University Press
Dissertation Permission

June 8, 2013

Alexandra Oliveros Villalba
4202 E. Fowler Ave. ENB118
Tampa, FL 33620

Reference

Assessment of cell proliferation on 6H–SiC biofunctionalized with self-assembled monolayers. A. Oliveros, C.L. Frewin, S.J. Schoell, M. Hoeb, M. Stutzmann, I.D. Sharp and S.E. Saddow Journal of Materials Research, Volume 28, Issue 01 (January 2013), pp 78-86 Copyright © 2012 Materials Research Society

Biocompatibility Assessment of SiC Surfaces After Functionalization with Self Assembled Organic Monolayers. Alexandra Oliveros, Sebastian J. Schoell, Christopher Frewin, Marco Hoeb, Martin Stutzmann, Ian D. Sharp and Stephen E. Saddow. MRS Proceedings, Volume 1235 (2009) Copyright © 2009 Materials Research Society.

Characterization of 3C-SiC (100) as a platform for detecting the onset of acute myocardial infarction (AMI). Alexandra Oliveros, Anthony Guiseppi-Elie, Mark Jaroszeski and Stephen E. Saddow. MRS Proceedings, Volume 1433 (2012). Copyright © 2012 Materials Research Society.

Selection(s): excerpts
Dissertation Description
Title: Dissertation, by Alexandra Oliveros Villalba
Institution: University of Florida
Rights/Acknowledgement

Permission is granted for nonexclusive rights to reprint excerpts from three Cambridge University Press journal articles of which you are a co-author, as described above. This permission requires full acknowledgement of the articles, authors, journal, volume, issue, date and page numbers, followed by the copyright notice and the phrase "Reprinted with permission".

This permission is subject to the following conditions:
a.) the material to be reprinted must be original to you as the Cambridge University Press author and must not involve material obtained from a third party; any material copyrighted by or credited in the journal article to another source may require further clearance by you from the original source, and Cambridge University Press is not liable for the use of third party material
b.) you must forward or refer to Cambridge University Press all reprint/republication requests that you may receive involving the material published by Cambridge University Press
c.) please inform your co-authors and ensure that they do not object to your use

Sincerely,

Marc P. Anderson
Rights and Permissions Manager
Cambridge University Press
32 Avenue of the Americas
New York, N.Y. 10013-2473

Figure B.2 Reprint permission from Cambridge University Press.

Appendix B (Continued)

Below is the permission to reproduce material from [67] in Chapter 2, including section 2.2 to section 2.2.3.3, Figure 10, Figure 11, Figure 12 and Table 1.

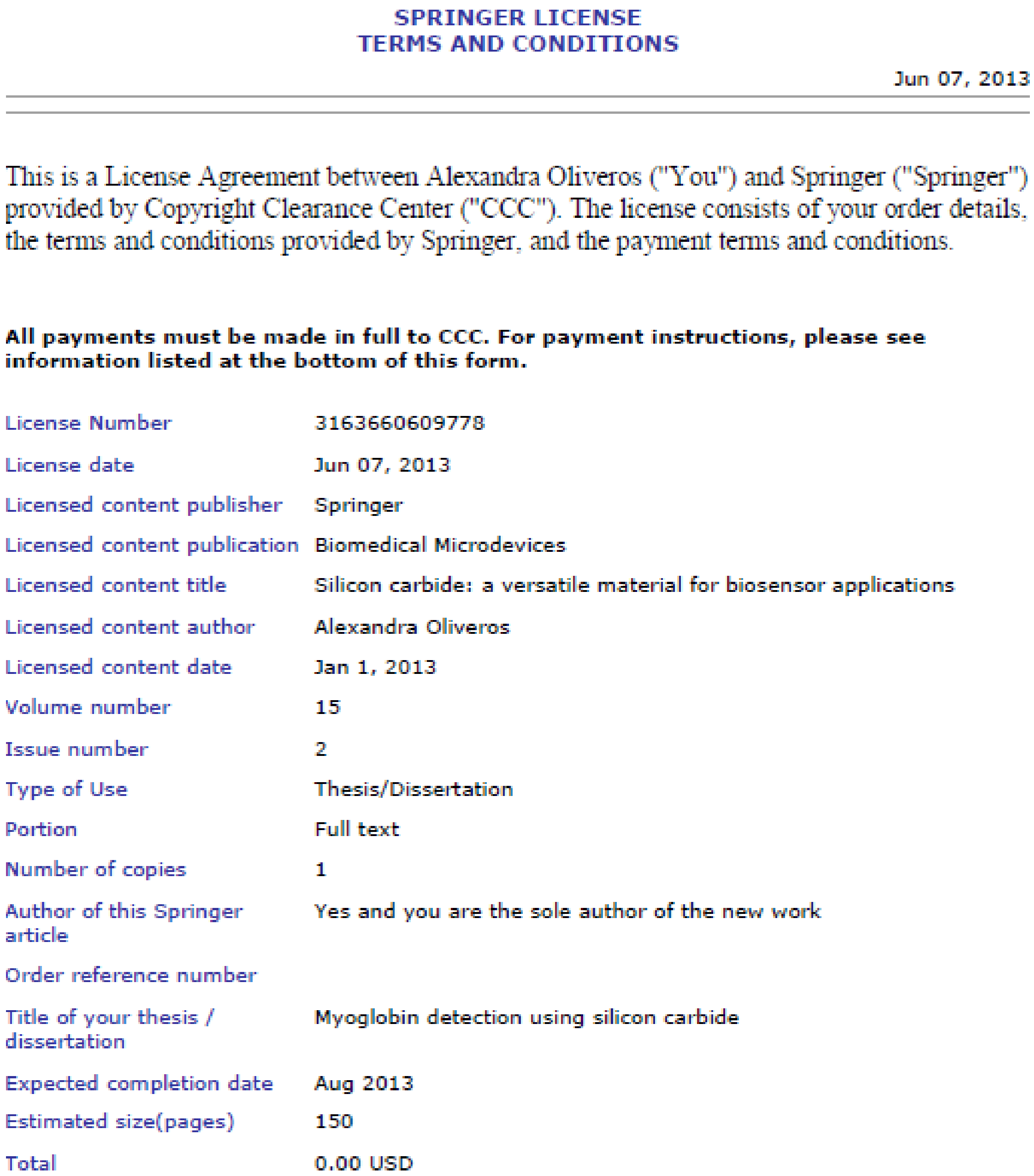

SPRINGER LICENSE
TERMS AND CONDITIONS

Jun 07, 2013

This is a License Agreement between Alexandra Oliveros ("You") and Springer ("Springer") provided by Copyright Clearance Center ("CCC"). The license consists of your order details, the terms and conditions provided by Springer, and the payment terms and conditions.

All payments must be made in full to CCC. For payment instructions, please see information listed at the bottom of this form.

License Number	3163660609778
License date	Jun 07, 2013
Licensed content publisher	Springer
Licensed content publication	Biomedical Microdevices
Licensed content title	Silicon carbide: a versatile material for biosensor applications
Licensed content author	Alexandra Oliveros
Licensed content date	Jan 1, 2013
Volume number	15
Issue number	2
Type of Use	Thesis/Dissertation
Portion	Full text
Number of copies	1
Author of this Springer article	Yes and you are the sole author of the new work
Order reference number	
Title of your thesis / dissertation	Myoglobin detection using silicon carbide
Expected completion date	Aug 2013
Estimated size(pages)	150
Total	0.00 USD

Figure B.3 Permission of reproduction of articles from Biomedical Microdevices (Springer).

Appendix B (Continued)

Below is permission to reproduce excerpts from [165] in Chapter 3, section 3.2 to section 3.3.2.4.

ELSEVIER LICENSE
TERMS AND CONDITIONS

Jun 10, 2013

This is a License Agreement between Alexandra Oliveros ("You") and Elsevier ("Elsevier") provided by Copyright Clearance Center ("CCC"). The license consists of your order details, the terms and conditions provided by Elsevier, and the payment terms and conditions.

All payments must be made in full to CCC. For payment instructions, please see information listed at the bottom of this form.

Supplier	Elsevier Limited The Boulevard,Langford Lane Kidlington,Oxford,OX5 1GB,UK
Registered Company Number	1982084
Customer name	Alexandra Oliveros
Customer address	4202 E. Fowler Ave TAMPA, FL 33620
License number	3165420370681
License date	Jun 10, 2013
Licensed content publisher	Elsevier
Licensed content publication	Elsevier Books
Licensed content title	Silicon Carbide BiotechnologyA Biocompatible Semiconductor for Advanced Biomedical Devices and Applications
Licensed content author	S.J. Schoell,A. Oliveros,M. Steenackers,S.E. Saddow,I.D. Sharp
Licensed content date	2012
Number of pages	55
Start Page	63
End Page	117
Type of Use	reuse in a thesis/dissertation
Intended publisher of new work	other
I am an academic or government institution with a full-text subscription to this journal and the audience of the material consists of students and/or employees of this institute?	No
Portion	excerpt
Number of excerpts	4
Format	both print and electronic

Figure B.4 Permission to use excerpts of a co-authored book chapter (Publisher: Elsevier).